MOLECULAR ENGINEERING OF ELECTRICAL CONDUCTIVITY OF ORGANIC NANOFIBER MATERIALS

by

Na Wu

A dissertation submitted to the faculty of
The University of Utah
in partial fulfillment of the requirements for the degree of

Doctor of Philosophy

Department of Materials Science and Engineering

The University of Utah

May 2017

The University of Utah Graduate School

STATEMENT OF DISSERTATION APPROVAL

The dissertation of **Na Wu**

has been approved by the following supervisory committee members:

Ling Zang	, Chair	**12/01/2016** Date Approved
Feng Liu	, Member	**12/01/2016** Date Approved
Shelley D. Minteer	, Member	**12/01/2016** Date Approved
Jennifer S. Shumaker-Parry	, Member	**12/01/2016** Date Approved
Rajesh Menon	, Member	**12/06/2016** Date Approved

and by **Feng Liu** , Chair of

the Department of **Materials Science and Engineering**

and by David B. Kieda, Dean of The Graduate School.

ABSTRACT

Perylene tetracarboxylic diimide (PTCDI) derivatives, typical n-type organic semiconductors with high thermal- and photostability, have been extensively investigated for one-dimensional (1D) self-assembly and their applications in electronic and opto-electronic devices. Unfortunately, the intrinsically low electrical conductivity of PTCDI-based materials hinders further development of functions and applications. To solve this problem, covalently linked electron donor-acceptor (D-A) PTCDI molecules were designed, synthesized, and assembled into nanofibers in this work. Their electrical properties and the thermal- and photo-effects have been systematically studied. In addition to providing an improved understanding of the basic properties of the materials, these studies also open new and potential applications of the D-A PTCDI nanofibers.

We designed a PTCDI molecule with 1-methylpiperidine (MP) substituted as electron donor to construct self-doped semiconductors, through one-dimensional (1D) self-assembly of the molecules into a nanofiber structure. The resultant nanofibers exhibit much higher conductivity than the other reported PTCDI molecules. The mechanism studies demonstrate that the MP moieties reduce the adjacent PTCDI core into an anionic radical, which acts as the n-type dopant in the PTCDI lattice. Such highly conductive nanofiber materials can be used as chemiresistive sensor for vapor detection of hydrogen peroxide.

Our further study on the MP-PTCDI nanofibers reveals a persistent photoconductivity

(PPC) effect, which is sustained conductivity after light illumination is terminated. Systematic study demonstrates the PPC effect is predominantly caused by the D-A structure of PTCDI. This study helps understand the PPC mechanism, and guide the design of new material structures for sustained charge separation to further enhance the photovoltaic and photocatalytic efficiency of organic semiconductor materials.

Thermoactivated conductivity was studied in the nanofiber materials assembled from other two D-A PTCDI molecules both in the dark and under visible light illumination. A symmetric n-dodecyl side chain substituted PTCDI nanofiber was used as a control for the comparative study. The charge transport properties are strongly dependent on the PTCDI molecular structure and packing states within the nanofibers. The comprehensive understanding of the thermoactivated conductivity in PTCDI nanofibers can assist in designing new D-A molecules that can be fabricated into nanofibers to be used as temperature sensor with increased sensitivity.

To my beloved family

TABLE OF CONTENTS

LIST OF TABLES

LIST OF ABBREVIATIONS

1D	One-dimensional
A	Acceptor
AFM	Atomic force microscopy
BHJs	Bulk heterojunctions
C60	Fullerene
CBP	4'-bis(9-carbazolyl)-2,2'-biphenyl
CH-PTCDI	N,N-(dicyclohexyl)perylene-3,4,9,10-tetracarboxylic diimide
CTC	Charge transfer complex
D	Donor
DADP	Diacetone diperoxide
DC	Direct current
DD-PTCDI	N,N'-di(dodecyl)-perylene-3,4,9,10-tetracarboxylic diimide
DIP	Di-indenoperylene
DMSO	Dimethyl sulfoxide
EA	Electron affinity
F4-TCNQ	2,3,5,6-Tetrafluoro-7,7,8,8-tetracyanoquinodimethane
GDM	Gaussian disorder model
GIXD	Grazing incidence X-ray diffractometry
H_2O_2	Hydrogen peroxide
HMTD	hexamethylene triperoxide diamine
HOMO	Highest occupied molecular orbital
IDE	Interdigitated electrode
IE	Ionization energy
IPA	Ion-pair

KPFM	Kelvin probe force microscopy
L_D	Diffusion length
LLR	Large lattice relaxation
LUMO	Lowest unoccupied molecular orbital
MA-PTCDI	N,N-dimethylaniline-substituted perylene tetracarboxylic diimide
MB	Microscopic barrier
MO-PTCDI	4-Methoxybenzyl-substituted perylene tetracarboxylic diimide
MP	1-methylpiperidine
MP-PTCDI	1-methylpiperidine-substituted perylene tetracarboxylic diimide
MT-PTCDI	N,N-dimethylbutylamine-substituted perylene tetracarboxylic diimide
NDI	Naphthalene diimide
NIR	Near-infrared
NPD	N, N'-diphenyl-N, N'-bis(1-naphthyl)-1,1'-biphenyl-4,4" diamine
o-DCB	Ortho-dichlorobenzene
OFETs	Organic field-transistors
OLEDs	Organic light-emitting diodes
OSCs	Organic semiconductors
P3HT	Poly(3-hexylthiophene)
PCB-c-P3HT	Fullerene-capped poly(3-hexylthiophene)
PCBM	[6,6]-phenyl-C61-butyric acid methyl ester
PCT	Photoinduced charge transfer
PET	Photoinduced electron transfer
PPC	Persistent photoconductivity
PPV	Phenylenevinylene
PTCDA	3,4,9,10-perylenetetracarboxylic dianhydride
PTCDI	Perylene tetracarboxylic diimide or Perylene diimide
PtOEP	Polycrystalline 2, 3, 4, 7, 8, 12, 13, 17, 18-octaethyl-21H23H-porphine platinum (II)
RLPF	Random localized potential fluctuations
SEM	Scanning electron microscope

SubPC	Boron subphthalyocyanine
TATP	Triacetone triperoxide
TBP	Tribenzopentaphene
TCNQ	7,7,8,8-Tetracyanoquinodimethane
TTF	Tetrathiafulvalene
UPS	Ultraviolet photoelectron spectroscopy
UV	Ultraviolet
XRD	X-ray diffraction
ZnPc	Zinc phthalocyanine

ACKNOWLEDGEMENTS

I would like to express my sincere gratitude to my advisor, Prof. Ling Zang, for his help, guidance, support, encouragement, and impact in my Ph.D. life. I appreciate him offering me a chance to study in the field of materials science and engineering. Prof. Zang is a knowledgeable, rigorous, and gracious mentor for both academics and life. I have learned a lot from him, including how to do research, how to analyze scientific problems, and how to present the points. I also appreciate his consistent motivations and helpful corrections in my presentations and writing. He has also shared with me his viewpoints on life and career. I am very grateful and happy that I was able to work with Prof. Zang for the past four and a half years. I also appreciate the time and help from my other committee members, Prof. Feng Liu, Prof. Shelley D. Minteer, Prof. Jennifer S. Shumaker-Parry and Prof. Rajesh Menon. Thank you all for your advice, support, and encouragement

I greatly appreciate all my previous and current group members, Dr. Xiaomei Yang, Dr. Yanke Che, Dr. Jimin Han, Dr. Ligui Li, Dr. Helin Huang, Dr. Miao Xu, Dr. Benjamin R. Bunes, Dr. Chen Wang, Paul M. Slattum, Daniel L. Jacobs, Yaqiong Zhang, and Dr. Li Yu. Thanks for your guidance, training, support, and help.

I would like to thank Dr. Brian van Devener, Dr. Paulo Perez, Dr. Randy Polson, Brian Baker, Charles Fisher at the Utah Nanofab, Garrett Meeks in the MSE characterization lab, Dr. Atta M. Arif in the Department of Chemistry, and Dr. Marc. D.

Porter's group for their assistance in sample characterization and analysis.

I would also like to thank all the faculty and staff in the Department of Materials Science and Engineering for their knowledge, guide and help.

I also like to thank all my friends. I appreciate their help.

I would take this chance to thank my mother, father, younger brother, grandmother, and grandfather, for their persistent love, support, and encouragement all through my life.

At the end, I would like to express my special appreciation to my husband, Zhonghua Zhan, for his love, selfless support, and encouragement.

This dissertation is based upon work supported by the Department of Homeland Security, Science and Technology Directorate under Grant (2009-ST-108-LR0005), NSF (CHE 0931466 and CBET 1502433), the SEED grant of the VP office of University of Utah (award # 10029849), and USTAR program, I appreciate their support.

Chapter 2 is reprinted with permission from the ACS Applied Materials & Interfaces 2016, 8, 12360-12368.

Chapter 3 is reprinted with permission from the ACS Energy Letters 2016, 1, 906-912.

Chapter 4 is reprinted with permission from the Journal of Physical Chemistry Letters 2017, 8, 292-298.

CHAPTER 1

INTRODUCTION

1.1 Introduction of Organic Semiconductors

1.1.1 Organic Semiconductors

An organic semiconductor (OSC) refers to organic materials that exhibit semiconductor properties, mainly consisting of alternating single and double bonds, leading to high degree of conjugation owing to the presence of π-electrons in their structures.[1-3] In 1977 the first high conducting polymer, chemically doped polyacetylene, was discovered, which demonstrated that polymers could be used as electrically conductive materials.[4,5] Since then, organic semiconductors have emerged as a promising field of research and development. Numerous organic semiconductor materials have been designed and synthesized. They have been used in electronic devices as alternatives to inorganic semiconductors,[6] including organic field-transistors (OFETs),[1,7] organic light-emitting diodes (OLEDs),[8,9] photovoltaics,[10,11] photodetectors,[12,13] lasers,[14] and sensors.[15-19] Organic semiconductors are much cheaper than inorganic semiconductors, and in particular, they are mechanically flexible and solution processable at low temperatures, making them good candidates for flexible electronic devices.

Organic semiconductors can be classified into two categories according to molecular weight: small molecules (or oligomers) and polymers. Depending on the preferential

transportation of holes or electrons, the organic semiconductors are categorized into p-type (hole as the majority carrier) and n-type (electron as the majority carrier) materials.[1] For p-type OSCs, their highest occupied molecular orbital (HOMO) is relatively higher (between 4.0 to 5.5 eV), which favors donating an electron, therefore generating holes as the charge carriers. P-type OSCs have been extensively explored, and some examples are presented in Figure 1.1. The most studied materials have been acene and thiophene derivatives.[20] For example, pentacene (one of the acene family) is a representative p-type semiconductor material, which has a remarkable high hole mobility up to 1.1 $cm^2 V^{-1} s^{-1}$ on the substrate of alumina, 3.3 $cm^2 V^{-1} s^{-1}$ on a soft polymer substrate, and 35 $cm^2 V^{-1} s^{-1}$ for a single crystal at room temperature.[21] However, the major drawbacks of pentacene are the insolubility in common solvents and low photostability (due to photoinduced oxidation), therefore prompting researchers to modify the pentacene molecule with functional side groups to improve the solubility and stability, while maintaining the semiconducting features to the maximal.

In contrast to p-type OSCs, the exploration of n-type semiconductors is more challenging because of their poor ambient stability and low electrical performance. N-type OSCs are normally electron-deficient small molecular and π–conjugated polymers with relatively lower energy level of lowest unoccupied molecular orbital (LUMO) (i.e., below -3.0 eV ideally).[22,23] Figure 1.2 lists some widely studied n-type OSCs. Some challenges can be found in the development of n-type OSCs. First, the electrical performance of n-type OSCs is relatively low. Few of the n-type OSCs that have been reported to date can have an electron mobility comparable to that of amorphous silicon (~ 1.0 $cm^2 V^{-1} s^{-1}$).[24] The low performance of n-type OSCs limits the development of

organic electronic devices because both p-type and n-type OSCs are needed for constructing ambipolar transistors, p-n junctions, and organic circuits, whereas the mobility of p-type OSCs is much higher.[25] Second, due to the low LUMO energy level, the n-type OSCs are not stable in ambient environment, because the electrons are easily trapped by O_2 and H_2O at ambient conditions, or by the hydroxyl groups at the surface of gate insulators, such as SiO_2.[23,26] The other challenge of n-type OSCs is that the electron injections are restrained due to the energy level mismatch between the LUMO of n-type semiconductors and the Fermi level of electrodes, e.g., Au. In practice, Au electrodes are still commonly used due to their greater stability than low work-function electrodes (Ca, Mg, Al, etc.), but with surface modification to reduce the injection barrier.[27] To improve the stability and mobility of n-type OSCs, some strategies for designing high-performance and ambient-stable n-type OSCs were summarized by the Hu group:[28] (1) functionalization of electron-deficient π-conjugated systems by using fluorine or fluorocarbon-based functional groups; (2) functionalization of electron-deficient π-conjugated systems by using electron-withdrawing groups, such as CN, CF_3; and (3) construction of donor-acceptor (D-A) structures.

1.1.2 Charge Transport Mechanisms in Organic Semiconductors

Charge transport properties in organic semiconductors are distinct from the characteristics in inorganic semiconductors. In inorganic semiconductors, strong ionic or covalent bonds lead to the formation of three-dimensional crystalline structures with substantial orbital overlap. Therefore, efficient charge transport can occur through highly delocalized bands, presenting high charge carrier mobility. However, in OSCs, molecules

are organized via supramolecular van der Waals, dipole-dipole, π–π, and hydrogen-bond interactions.[29] The weak intermolecular interactions, closed-shell electronic structures of the individual organic molecule, and relative disorder of OSCs materials make the charge transport properties in OSCs different from inorganic semiconductors.

The charge transport mechanism in OSCs is tightly related to temperature.[2,30] At low temperatures (i.e., 100-300 K), band-like charge transport was observed in crystalline OSCs.[31] For instance, the intrinsic transport of field-induced charges on the surface of a single crystal of rubrene has been studied, and it has been noted that its mobility increased with decreasing temperature.[32] At room temperature or higher, it is generally believed that the charge mobility of semiconducting organic materials is determined by a hopping transport mechanism,[2,33] where charges jump from site to site, because the charge carriers turn to be more conductive to localize at higher temperature due to the reduced effective bandwidth. Electrical conduction by hopping is still not clear. One of the most clearly understood mechanisms is the polaronic transport, a phonon-assisted hopping process.[34] Upon adding or removing an electron from a molecule, associated with the resultant molecular skeleton changes because of the readjustment of the individual bond lengths, a polaron forms. The polaron is a quasiparticle by electron-phonon coupling, the binding energy of which comes from local geometric relaxations and increased polarization of the surrounding medium. The polaron hopping is thus a charge associated with a molecular distortion.[35]

In addition to the effect of temperature, the molecular arrangement patterns also influence the charge transport mechanism. The Weng group observed the photogenerated free carriers, rather than exciton at room temperature, in highly crystalline Zinc

phthalocyanine (ZnPc films) prepared by weak epitaxy growth method. The band-like electronic feature of ZnPc thin film is from the effective intermolecular interactions between the cofacially-stacked π-conjugated ZnPc molecules.[36]

1.1.3 Doping of Organic Semiconductors

Organic semiconductors have an intrinsic smaller charge carrier mobility and lower performance compared to inorganic semiconductors due to the closed-shell electronic structures of the individual organic molecules, weak intermolecular interactions, and comparatively disordered structure.[29,37] Electrical doping of OSCs has emerged as an effective strategy to improve the performance of organic electronic devices and to extend the range of functionality. In particular, controllable doping of OSCs can make great technological breakthroughs like what happened in the inorganic semiconductor industry, which constitutes the basis for electronic devices.[38,39]

The basic doping fundamentals in OSCs are similar to those in inorganic semiconductors, that is to say, extra mobile charge carriers in OSCs matrix are produced by electron donors or acceptors (Figure 1.3).[40] Theoretically, in OSCs doping, dopants are added into the organic semiconductor matrix, which will transfer electrons to the LUMO states of OSCs (n-type doping) or remove electrons from the HOMO states of OSCs to generate holes (p-type doping). The dopants can be small molecules or atoms, such as iodine, bromine, Lewis acids, lithium, cesium, and strontium atoms. However, these small dopants show a strong tendency to diffuse, leading to a falling performance of electronic devices.[6] To resolve these problems, molecular doping, of which larger organic molecular electron acceptors or donors are dopants, has been developed in the past

decades as a replacement for traditional doping.[6,38,39] For example, strong electron acceptor F4-TCNQ has been widely used as a p-type dopant. For example, F4-TCNQ was doped in ZnPc to enhance the conductivity and reduce the Seebeck coefficient.[41] With this methodology, stable and high performance electronic devices have been designed and developed.

In molecular doping, ion-pair (IPA) and ground-state charge-transfer formation are widely considered as the two fundamental interaction mechanisms between dopant and OSCs matrix (Figure 1.4).[38] For the IPA mechanism, electron transfer happens between dopants and OSCs, giving rising to the formation of anion and cation (the ion pair). Taking p-type doping as an example, when the electron affinity (EA) of the acceptor is equal or higher than the ionization energy (IE) of the OSCs, one electron is transferred from the HOMO of the OSCs to the LUMO of the acceptor, followed by formation of an acceptor anion and an OSC cation. The IPA mechanism of n-type doping is similar, but the electron is transferred from the HOMO of the n-type dopant to the LUMO of the OSC.

Another mechanism that generates mobile charge carrier density in molecularly doped OSCs is dependent on the establishment of ground state charge transfer complex (CTC).[38,42] Interacting with dopants, new occupied bonding and empty antibonding orbitals are formed from the rearranging of the frontier molecular orbitals of an OSC molecule and a dopant. The new energy levels of CTC ($E_{CTC,\,H/L}$) are determined by the contribution of parent OSC and dopant as descripted by the Hückel-type model (Equation 1.1, for p-type doping), where H_{OSC} is the HOMO level of OSC, L_{dop} is the LUMO level of the dopant, and β is the resonance integral. In the case of p-type doping, if IE of the

CTC is higher and its EA lower than the IE of the OSC, the electrons will be reorganized, creating a filled level below the transport manifold of the OSC and an empty one above. Subsequently, the CTC is ionized to form a separated mobile hole in the OSC. In other words, the CTC acts as a dopant. The energy levels and the corresponding density of states (DOS) of IPA and CTC molecular doping processes are sketched in Figure 1.4.[38,43]

$$E_{CTC,\frac{H}{L}} = \frac{H_{OSC} + L_{dop}}{2} \pm \sqrt{\left(H_{OSC} - L_{dop}\right)^2 + 4\beta^2} \qquad 1.1$$

Two important factors are generally considered in doping OSCs, one is the position of the Fermi level after doping.[6,40] Doping will shift the Fermi level toward the transport level of the OSCs. The position of the Fermi level after doping can be examined from the Seebeck effect as seen in Equation 1.2.[41,44]

$$S(T) = \frac{k_B}{e}\left[\left(\frac{E_F(T) - E_u}{k_B T}\right) + A\right] \qquad 1.2$$

where S is the Seebeck coefficient. E_u is the energy level of transport states and E_F is the Fermi-level. A is a numerical factor, k_B is the Boltzman constant, T is the temperature, and e is the elementary charge. Ultraviolet photoelectron spectroscopy (UPS) can be used to determine the distribution of transport states (E_u). Therefore, the position of the Fermi level after doping can be measured, allowing for a deeper understanding of the doping and realizing controllable doping. The other is the doping efficiency. Doping efficiency is strongly related to the EA and IE of dopant (or CTC) and host OSCs.

1.1.4 Application of Organic Semiconductors

Organic semiconductors are alternative to conventional inorganic semiconductors in some areas and have been used commercially, such as in xerography, sensor, lighting, and display. OSCs are cheaper, flexible, and easy to process. Numerous investigations and developments of OSCs application have been reported. Herein, some typical applications based on OSCs will be briefly reviewed, particularly the applications in electronic devices including field-effect transistors, light emitting diodes, photovoltaic systems, and electrical sensors.

1.1.4.1 Organic Field-Effect Transistors

Organic field-effect transistors (OFETs) have been fabricated with various device geometries.[1,7] The most commonly used device geometry is bottom gate with top drain and source electrodes. The active organic FET layer can be deposited onto the substrate by thermal evaporation, solution-process coating, printing, or electrostatic lamination. Field-effect mobility is one of the key parameters considering OFETs' performance, which is largely relevant to the electronic properties of OSCs materials. The field-effect mobility (μ) was lower than 10^{-3} cm^2 V^{-1} s^{-1} about 25 years ago, but it has increased to about 1-10 cm^2 V^{-1} s^{-1} for some OSCs due to advancements in molecular design, material processing techniques, and device architecture. OFETs have been used in displays, simple circuits, and chemical and biological sensors.

1.1.4.2 Organic Light-Emitting Diodes

An organic light-emitting diode (OLED) is a device that transforms electrical power into light. In a typical OLED device, the active OSCs are located between two suitable electrodes. Single-layer of heterojunctions of OSCs can be employed in OLED devices.[9,45,46] Heterojunction OLEDs are more widely investigated and developed because of the higher efficiency than single-layer ones. A typical bilayer OLED involves cathode, emissive layer, conductive layer and anode. The basic working principle of an OLED is that when a bias voltage is applied to the electrodes, electrons are injected from the cathode to anode through giving electrons to emissive layer and removing electrons from the conductive layer. The holes in the conductive layer move to the emissive layer, where the recombination of the electron and hole results in the formation of a photon, of which the frequency is determined by the energy gap of the HOMO and LUMO levels of emitting molecules. The efficiency of an OLED can approximately be deduced by Equation 1.3,[6] where $\eta_{external}$ is the final efficiency of the device, b_1 is the carrier balance, which can be adjusted by choosing suitable blocking layers in multilayer OLED devices, U is the operating voltage, and η_{recomb} is the quantum efficiency of carrier recombination, determined by the ratio of radiative recombination of excitons to the total number of excitons, and $\eta_{optical}$ is the efficiency of the optical outcoupling from the device. Researchers have focused on the materials design and devices structure improvement to enhance the efficiency of the OLED. Usually, doped OSCs in the OLEDs can improve the charge carriers injection, leading to lower driving voltage, thus to an enhanced power efficiency.[47]

$$\eta_{external} = b_I \frac{hv}{eU} \eta_{recomb} \eta_{optical} \quad 1.3$$

1.1.4.3 Organic Photovoltaics

Similar to the application in OLEDs, OSCs have also been extensively used in photovoltaic devices (solar cells), which are devices to convert light into direct current (DC) electricity. Being excited by light with energy larger than the band gap of the OSCs, excitons are formed, and then excitons are separated into free electrons and holes, which move in different directions to cathode and anode, converting solar energy into DC electricity.[10] Unlike inorganic solar cells, the exciton is generated in OSCs as a tightly bound electron-hole pair because of the strong Coulomb attraction between the electron and hole due to the low dielectric constant of organic materials.[48-51] Consequently, improving the charge separation efficiency is a key issue of organic solar cells. To meet this challenge, bulk heterojunctions (BHJs) of OSCs have been developed, [11,52,53] which have an absorber layer consisting of a blend of donor and acceptor materials in nanoscale. The advantage of the donor-acceptor (D-A) heterojunction is to accelerate the electron and hole separation rate. The electron-hole binding energy is evaluated to be 0.35-1.0 eV,[11] which is larger than the thermal energy at room temperature (k_BT ~ 0.026 eV) by an order of magnitude. Therefore, D-A structure is constructed to facilitate the generation of free charge carriers at the D-A interface through the driving force created by the energy level offset between donor and acceptor.

1.1.4.4 Organic Electrical Sensors

The other important application of OSCs is in electrical sensors,[15,54] which have been extensively used in industrial, environmental, and medical areas as well as public safety. Sensitivity, selectivity, and the response and recovery time are among the important criteria for sensors. Traditional inorganic electrical sensors have already been widely studied and commercially used. Unfortunately, inorganic electrical sensors have limitations in selectivity and require high operation temperature.[15] Especially for the sensors that are made of metal oxide semiconductors, the dramatic response to humidity (moisture) inhibits the application in open environments. OSCs provide alternative materials for sensor development that possess much more flexibility for structural and property modification in order to improve the sensor selectivity. In principle, the selectivity is achieved through molecular recognition based on analyte-OSC interactions, which include hydrogen bonding, dipole-dipole interactions, van der Waals interactions, and charge transfer.[55] When exposed to analytes, the electrical properties of OSC materials can be affected through charge transfer interaction, charge trapping or doping, adjusting the charge injection or extraction behavior at the electrode/OSCs interfaces, or changing the molecular arrangement of OSCs. The Zang group has developed a series of organic nanofibril chemiresister sensors, which were able to detect trace vapor of explosives,[18] amines,[19] hydrogen peroxide,[17] alkane,[16] and so on. These nanofibers, fabricated from self-assembly of OSC molecules, can provide exciton or electron transport channel as sensing materials, and have the potential to amplify the output signal due to the long-range exciton or electron migration along the one-dimensional well-organized nanofibers.[56,57] Organic field-effect transistors (OFETs) are also excellent

transducers for sensing because amplified signals can be attained.[58] According to the working principle of OFET when analytes interact with channel materials, the signal can be modified by the gate voltage. If the gate dielectrics are used as the sensitive layer, a small change of the effective gate voltage induced by analyte may lead to a pronounced variation of channel current.[15] OFET sensors can be applied for detecting chemicals in gas (vapor) phase, or analytes in solution or biological system with high sensitivity.

1.2 Organic Semiconductors With Donor-Acceptor Structure

1.2.1 The Significance of Donor-Acceptor for Organic Electronics

Modification of organic semiconductors with electron donor-acceptor (D-A) structure or interface is an interesting research topic, because it is an efficient strategy to achieve high conductivity of OSC materials,[17,18,59] or to construct higher performance electronic devices.[60] The efficiency and rate of electron transfer between donor and acceptor are determined by the electron donating and accepting abilities in the D-A system, and the distance, spatial orientation, and flexibility between the donor and acceptor moieties.[61] In this section, we will discuss the significance of OSCs with D-A system.

First, lower band gap OSCs can be synthesized by incorporation of D-A system.[62,63] In general, the HOMO level of OSCs shifts to higher energy level by the introduction of strong electron donating groups, whereas the presence of strong electron accepting groups lowers their LUMO levels. The OSCs with low band gaps have broadened absorption from the ultraviolet (UV) to the near-infrared (NIR) region, enabling fully utilizing the solar energy for solar cells[64] and realizing broadband photo-detection.[65]

Second, the significance of D-A system in OSCs is to enhance the charge generation

and separation. Charge generation is achieved through the formation of charge-transfer complex (CTC) or photoinduced charge transfer (PCT). It has been demonstrated that a charge transfer complex can be formed when an electron donor (D) molecule or moiety has low ionization potential and an electron acceptor (A) molecular or moiety has relatively high electron affinity (Equation 1.4),[66] where δ^{+}, δ represent the partial charge distributed between the D and A part. Upon association, some new properties arise in the CTC, for example, new charge-transfer (CT) bands are formed. Optical spectroscopy is a powerful technique to characterize CT bands, such as UV-vis absorption spectroscopy, luminescence spectroscopy, electron paramagnetic resonance spectroscopy, resonance Raman spectroscopy, positron annihilation spectroscopy (PAL) [67] and so on.

$$D + A \leftrightarrow [D^{\delta+} \cdot A^{\delta-}] \qquad 1.4$$

A charge transfer complex may assist the generation of charge carriers when an electric field is applied on the D-A compound, resulting in dramatic enhancement in conductivity.[68] The enhanced conductivity is attributed to the charge generation and subsequent disassociation with D-A structure or D-A interface.[69] Tetrathiafulvalene (TTF) - 7,7,8,8-Tetracyanoquinodimethane (TCNQ) is a prototype charge-transfer compound.[70] The complex is formed in solution and can be precipitated and grown into a crystalline solid (Figure 1.5 a).[71] In a TTF-TCNQ crystal, TTF and TCNQ are arranged in separated linear chains, then aligned interspaced (Figure 1.5b).[72] TCNQ is an acceptor molecule with electron affinity of 2.88 eV which can be easily reduced to the anion radical TCNQ when it interacts with electron donors, such as TTF.

Photoinduced charge transfer (PCT) is mainly about photoinduced electron transfer (PET),[18,69,73] which is an excited electron transfer process by which an excited electron is transferred from donor (D) to acceptor (A). When an organic molecule is excited by photon absorption, an electron in a ground state orbital can be excited to a higher energy orbital. On one hand, this excited state leaves a vacancy in a ground state orbital that can be filled by an electron donor. On the other hand, it generates an electron in a high energy orbital, which can be donated to an electron acceptor. In addition to the PET process, researchers have also discovered a photoinduced hole transfer process, of which a hole is generated through photoexcitation of an acceptor, followed by transfer to the ground state donor.[74] This PCT process has attracted great interest because of their fundamental role in applications such as solar cells and artificial photosynthetic systems.

Regarding the research on the D-A OSCs, two categories of D-A structures can be developed. One is the covalent D-A molecules, where D and A parts are constructed in one molecule via organic synthesis techniques; the other is the noncovalent D-A structure, where two or more donor and acceptor molecules associate to form D-A interface by molecular engineering, such as co-crystallization, blending, and surface coating, etc.[69]

1.2.2 Structure-Property Relationship of Organic Semiconductors

It has been demonstrated that the electronic properties of OSCs are tightly related to their molecular and supramolecular structure. In addition, the performance of the electronic devices based on OSCs depends on the morphology of these active materials.

In the previous section, we discussed the significance of D-A system. Organic

semiconductors with a D-A system can have a narrower band gap and enhanced charge carrier generation and separation efficiency. However, there are some drawbacks for some simple D-A systems, particularly in polymers. One is the absence of control over the orientation of molecular components because conventional synthesis (or polymerization) restricts the regioselectivity when asymmetric monomers are utilized.[75] As a result, the limit in the regioselectivity would influence the intermolecular π-stacking interactions, leading to inefficient charge transport.[76,77] Another drawback is the limited solubility of organic materials.[78] To overcome the drawbacks and increase the D-A interactions, organic semiconductors with multiple alternating donor or acceptor groups were designed to control both the structural and electronic properties. In Watkin group's work, A-D1-A-D1 and A-D1-A-D2 structures were compared. By using two different donor fragments (D1 and D2) in the polymer semiconductor, it demonstrated improved intermolecular π-stacking interactions and therefore enhanced charge-carrier mobility. The solar cells based on A-D1-A-D2 polymer exhibited short-circuit current densities twice as high as the ones fabricated with simple A-D1-A-D1 polymer, but still having the similar open-circuit voltage.[75] Patil et al. have also designed A1-D-A2-D polymer to fabricate OFETs and had a remarkable improvement in electron mobility due to the optimized chain packing and resultant large crystalline domains formation in solid state.[79] In addition, molecular ambipolar D-A1-A2 organic semiconductors were synthesized to suppress the back electron transfer through the cascade energy levels.[61]

Charge mobility is one of the most fundamental properties of semiconductors. The charge mobility is strongly associated with the degree of long range order. In organic semiconductors, the charge (free charge carriers, molecular excited state, or exciton)

diffusion length (L_D) is important regarding the mobility. Taking the exciton as an example, it has been established that exciton transport is a function of the extent of crystalline order.[80-82] Lunt et al. have measured the exciton diffusion lengths of several organic semiconductor thin films which are widely used in organic electronic devices by spectrally resolved photoluminescence quenching. The measured diffusion length values can be found in Table 1.1. The exciton diffusion length was revealed to be strongly related to the molecular stacking habit and the existence of dimer states in polycrystalline thin film.[81]

Controlling the morphology of the active layer is an important strategy for increasing the efficiency of electrical devices based on OSCs. For example, a lot of research works were focused on optimization of organic materials morphology to enhance BHJ photovoltaic efficiency.[11] The ideal structure of a BHJ solar cell is schematically descripted in Figure 1.6.[10] Interspaced donors and acceptors are arranged within an average length of exciton diffusion (about 10-20 nm), making sure the exciton can reach the D-A interface to initiate the charge separation. In addition, the two D-A phases are interlaced in percolated patterns to ensure efficient charge carrier transport with reduced recombination. There are many methods to modify the BHJ morphology, including adjusting the concentration and ratio of the donor and acceptor in solution, processing solvent, casting methods, drying rate, and post film treatment like thermal annealing and solvent annealing.[83] Generally, these methods can improve the organic materials' crystallinity, and control phase separation in the blend morphology to ensure continuous charge transport pathway to the electrodes. For example, the efficiency of a P3HT/C61-PCBM solar cell can be increased from 0.83% to nearly 5% when heating the film at 150

°C for 30 min.[84]

Besides the above methods, controlled self-assembly of organic semiconductors is the most desirable way to approach the ideal BHJ solar cell structure. A molecule PCB-c-P3HT, covalent linking a P3HT chain with fullerene, was designed and self-assembled into nanowires in an ortho-dichlorobenzene (o-DCB) solution. In contrast to noncovalently mixed P3HT polymer:fullerene blends, the covalent copolymer PCB-c-P3HT can self-assemble to produce more defined interfaces of donor and acceptor in thin films. Additionally, the crystallization of the P3HT core and alignment of the PCB into wires allows for high delocalization of charges and effective transport for carriers, giving rise to high dark current and photocurrent.[85]

1.2.3 Perylene Diimide Derivatives With Donor-Acceptor Structure

Perylene tetracarboxylic diimide (PTCDI) derivatives have been extensively studied and used as industrial dyes and pigments since 1912 because they are chemically inert and possess high thermal- and photostability.[86] Figure 1.7 is the chemical structure of PTCDI. The imide sides (R group) or bay positions (the 1, 6, 7, 12 positions) can be modified with various substituents to obtain different PTCDI molecules with different chemical and physical properties.

Later, PTCDIs' chemical and physical properties were further investigated. It was found that PTCDIs present a relatively low reduction potential (ca. -1.0 V for the first half-wave reduction potential and -1.2 V for the second half-wave reduction potential vs the ferrocene/ferrocenium [$FeCp^{2+/0}$] redox couple) and low electron affinity (about -3.9 eV for unmodified PTCDIs, comparable to fullerene [C_{60}] and its derivatives),[87-89]

combining with their superior thermal- and photostability, which enables their use as electron acceptors or n-channel materials in electronic and optoelectronic devices. Moreover, PTCDI molecules have also been widely studied in fundamental research on OSCs' charge transport mechanism, photo-induced energy and electron transfer processes.[90]

In this dissertation, we focus our research on the electrical properties and potential applications of imide substituted PTCDIs and their corresponding self-assembled nanofibers. More detailed properties of PTCDIs will be discussed in the following sections.

1.2.3.1 Molecular Structural Properties of PTCDIs

The perylene diimides present flat π-systems as established by X-ray diffraction of their single crystals. The frontier orbitals of perylene diimide are presented in Figure 1.8. It has been proven that the imide substituent has a negligible influence on the electronic properties of perylene bisimides because the nodes in the HOMO and LUMO at the imide positions of perylene diimides minimize the electronic coupling between perylene aromatic core and substituents,[57,86] for example, there is a less than 0.1 eV change on a PTCDI's LUMO upon switching from phenyl to perfluorophenyl on the imide positions.[91] It is beneficial to modify the PTCDI molecules to adjust their solubility, control the molecular packing patterns as well as comparatively study PTCDI molecules with different substituents without significantly changing the perylene diimide core's electronic properties.

1.2.3.2 Self-Assembly of PTCDI Molecules into One-Dimensional Nanostructures

PTCDI molecules can be self-assembled into well-defined one-dimensional (1D) nanostructures by controlling the solution processing conditions. The Zang group has conducted enormous pioneering works on the 1D self-assembly of PTCDI molecules and found that the 1D self-assembly is a thermodynamic process of maximizing the longitudinal π-π stacking over the lateral association to form bulky aggregates due to the hydrophobic interaction among the side chains.[56,92-94] Depending on the molecular structure and geometry, the effective self-assembly of PTCDI molecules into 1D nanostructures can be completed via rapid solution dispersion, phase transfer, vapor diffusion, seeded growth, and sol-gel processing.[56]

Crystal structures of PTCDIs have been extensively studied to help understand 1D PTCDI nanostructures. Most crystal structures of PTCDIs with symmetrical n-alkyl imide substitutes exhibit primitive triclinic unit cells. Taking the PTCDI-C_8H_{17} (PTCDI-C8) molecule as an example, the packing alignment of the PTCDI-C8 molecule in the unit cell is schematically shown in Figure 1.9. The PTCDI-C8 molecules exhibit slipped π-π stacking in the [100] direction with the shortest vertical distance at around 3.34 Å to 3.55 Å between the atomic planes of neighboring PTCDI-C8 molecule.[95] As the modification of substituted groups at imide sides with larger groups, the rotational offsets have been observed leading to different distorted π-π stacking patterns. N,N-(dicyclohexyl)perylene-3,4,9,10-tetracarboxylic diimide (CH-PTCDI) is a symmetric molecule with both sides substituted with cyclohexane groups, which shows a flip-flap stacking to minimize the steric hindrance between the cyclohexyl side-chains.[96]

1.2.3.3 PTCDI Nanofibers With Donor-Acceptor Structure

PTCDI nanofibers with D-A structure have attracted much research effort. A series of nanofiber structures modified with different D-A interfaces have been developed via covalent links or noncovalent interaction.

In covalently linked D-A molecules, it is difficult to obtain continuous one-dimensional stacking because the donors and acceptors prefer to stack with each other due to the charge transfer interaction between them.[97] Furthermore, charge recombination occurs easily between D^+ and A^- in the bulk-mixed phase of D and A. To solve this issue, amphiphilic D-A type PTCDI molecules (e.g., those with long alkyl chain in one imide side and the donor group in the other imide side) were designed and synthesized.[17,69,96] This type of PTCDI molecules can be fabricated into well-defined 1D nanostructures driven by the π-π stacking and side chains interactions.

Noncovalent D-A structure can be constructed through blending the PTCDI molecules (usually as the acceptor) with donor molecules, or controlled surface coating of PTCDI nanofibers with donor molecules, which offers more structure diversity and tailorability in comparison to the approach using covalent PTCDI D-A molecules. In particular, the morphology of D and A parts, as well as the interface, can be improved through postcoating treatments, such as solvent annealing or high temperature annealing. For the surface coating, appropriate donor molecules design can enhance the D-A interaction. The Zang group has demonstrated that the modification of the tribenzopentaphene (TBP) donor molecules with large side groups can prevent intermolecular π-π stacking of the donor molecules, leading to uniform molecular distribution of donors onto the PTCDI nanofibers, giving rise to a higher photocurrent

than PTCDI nanofibers coated with TBP modified with small side groups.[98]

1.2.3.4 Charge Transfer in PTCDI Nanofibers With D-A Structure

PTCDI molecules with D-A structures are used as the building blocks to construct 1D nanomaterials featuring higher conductivity (Figure 1.10). First, the ordered 1D π-π stacking in the PTCDI nanofibers favors the electron transfer through co-facial intermolecular π-delocalization.[56,57] As a result, relatively higher conductivity can be attained in the PTCDI 1D nanostructures due to efficient electronic coupling.

Second, PTCDI derivatives are acceptors in the D-A system, and can take part in a variety of excited-state electron transfer processes, as illustrated in Figure 1.11. In addition to the photoinduced charge separation, strong electron donors can also initiate charge separation in the dark though steady-state charge-transfer between donors on one molecule and PTCDI cores on the adjacent molecule, as demonstrated as the intermolecular charge transfer. In this process, the donor moieties with strong electron donating capability (evaluated by the oxidation potentials) and nucleophilicity can reduce PTCDI central cores into the anionic radicals.

1.3 Research Goal and Organization of the Dissertation

1.3.1 Research Goal

Perylene tetracarboxylic diimide (PTCDI) derivatives, a typical n-type organic semiconductor with high thermal- and photostability, have been extensively investigated for one-dimensional (1D) self-assembly and their applications in electronic devices. However, it's still challenging to have high performance electronic and optoelectronic

devices (or systems) with PTCDI-based material due to intrinsically limited properties of organic semiconductors, such as low conductivity. The goal of this dissertation is to design new PTCDI molecules with covalent donor-acceptor (D-A) structure, study their optical and electrical properties, and explore their applications in organic electronics and photocatalysis.

The intrinsically low electrical conductivity of organic semiconductors, due to properties such as the closed-shell electronic structures of the individual organic molecules, and weak intermolecular interactions, hinders further development and more widespread applications. In the first part of this dissertation, we developed a chemical self-doping method that can increase the electrical conductivity through a one-dimensional stacking arrangement of donor-acceptor (D-A) PTCDI molecules. The D-A structure is based on 1-methylpiperidine-substituted perylene tetracarboxylic diimide (MP-PTCDI), of which the MP moiety is a strong electron donor, and can form a charge transfer complex with the PTCDI moiety on the other molecule (acting as the acceptor) of an adjacent stacked molecule, generating anionic radicals of PTCDI (electron). Upon self-assembling into 1D nanostructure (specifically nanoribbons), the electron generated is delocalized along the long axis of PTCDIs through columnar π-π stacking, leading to enhancement in conductivity. The resultant PTCDI radicals function as n-type dopants located in the lattice of PTCDI crystals, in contrast to interstitial doping.

In the second part of this dissertation, the specific chemical and physical properties of PTCDI derivatives with D-A structure were studied in detail, particularly the persistent photoconductivity (PPC) and thermoactivated electrical conductivity in PTCDI nanofiber materials. The PPC is the sustained electrical conductivity after light illumination is

terminated. A comprehensive understanding of the PPC effect in PTCDI nanofibril materials will enable us to explore and enhance their optoelectronic applications, such as photovoltaics and photocatalysis. The study of temperature-dependent conductivity in PTCDI nanofibers provides us deeper insight into the charge transport mechanism, which will be conducive to developing more sensitive organic temperature sensors.

1.3.2 Organization of the Dissertation

The remainder of the dissertation contains the following four chapters.

Chapter 2 demonstrates research on chemical self-doping of MP-PTCDI nanoribbons for high conductivity and their application as a chemiresistive sensor for vapor detection of electron deficient chemicals. It includes the new PTCDI molecule design, the detailed chemical self-doping mechanism to achieve high conductivity, and chemiresistive sensing for hydrogen peroxide vapor detection.

Chapter 3 focuses research on persistent photoconductivity (PPC) effect in PTCDI-based nanofiber materials. This chapter demonstrates the PPC effect with respect to different temperature, illumination power densities, molar amount, and morphology of the PTCDI film. The comparative study of PPC effect in various PTCDI molecules modified with different electron-donating moieties was conducted with the aim to investigate the influence of electron donor-acceptor interaction on the PPC.

Chapter 4 presents the research of the thermoactivated conductivity in PTCDI nanofibers. We studied the temperature activated charge transport within the PTCDI nanofibers with D-A interfaces. For comparison, the study was also performed on a control sample, which was a nanofiber fabricated from a symmetric PTCDI molecule

with both sides modified with n-dodecyl chain. D-A structure helps create disorder regarding both the charge-transfer and dipole-dipole interactions between stacked molecules, and the increased disorder enlarges the activation barrier, enabling larger sensitivity to temperature.

Chapter 5 summarizes the major results and conclusions from all the research works described above, and provides some perspective for future research on PTCDI nanofibers, particularly those with D-A structure.

1.4 References

(1) Facchetti, A. Semiconductors for Organic Transistors. *Mater. Today* **2007**, *10*, 28-37.

(2) Coropceanu, V.; Cornil, J.; da Silva Filho, D. A.; Olivier, Y.; Silbey, R.; Brédas, J.-L. Charge Transport in Organic Semiconductors. *Chem. Rev.* **2007**, *107*, 926-952.

(3) Marrocchi, A.; Facchetti, A.; Lanari, D.; Petrucci, C.; Vaccaro, L. Current Methodologies for a Sustainable Approach to π-Conjugated Organic Semiconductors. *Energy Environ. Sci.* **2016**, *9*, 763-786.

(4) Shirakawa, H.; Louis, E. J.; MacDiarmid, A. G.; Chiang, C. K.; Heeger, A. J. Synthesis of Electrically Conducting Organic Polymers: Halogen Derivatives of Polyacetylene, $(CH)_x$ *J. Chem. Soc., Chem. Commun.* **1977**, 578-580.

(5) Chiang, C. K.; Fincher, C. R.; Park, Y. W.; Heeger, A. J.; Shirakawa, H.; Louis, E. J.; Gau, S. C.; MacDiarmid, A. G. Electrical Conductivity in Doped Polyacetylene. *Phys. Rev. Lett.* **1977**, *39*, 1098-1101.

(6) Walzer, K.; Maennig, B.; Pfeiffer, M.; Leo, K. Highly Efficient Organic Devices Based on Electrically Doped Transport Layers. *Chem. Rev.* **2007**, *107*, 1233-1271.

(7) Sirringhaus, H. 25th Anniversary Article: Organic Field-Effect Transistors: The Path Beyond Amorphous Silicon. *Adv. Mater.* **2014**, *26*, 1319-1335.

(8) Kamtekar, K. T.; Monkman, A. P.; Bryce, M. R. Recent Advances in White Organic Light-Emitting Materials and Devices (WOLEDs). *Adv. Mater.* **2010**, *22*, 572-582.

(9) D'Andrade, B. W.; Forrest, S. R. White Organic Light-Emitting Devices for Solid-State Lighting. *Adv. Mater.* **2004**, *16*, 1585-1595.

(10) Günes, S.; Neugebauer, H.; Sariciftci, N. S. Conjugated Polymer-Based Organic

Solar Cells. *Chem. Rev.* **2007**, *107*, 1324-1338.

(11) Scharber, M. C.; Sariciftci, N. S. Efficiency of Bulk-Heterojunction Organic Solar Cells. *Prog. Polym. Sci.* **2013**, *38*, 1929-1940.

(12) Zhang, H.; Jenatsch, S.; De Jonghe, J.; Nüesch, F.; Steim, R.; Véron, A. C.; Hany, R. Transparent Organic Photodetector Using a Near-Infrared Absorbing Cyanine Dye. *Sci. Rep.* **2015**, *5*, 9439.

(13) Lee, K.-H.; Leem, D.-S.; Castrucci, J. S.; Park, K.-B.; Bulliard, X.; Kim, K.-S.; Jin, Y. W.; Lee, S.; Bender, T. P.; Park, S. Y. Green-Sensitive Organic Photodetectors with High Sensitivity and Spectral Selectivity Using Subphthalocyanine Derivatives. *ACS Appl. Mater. Interfaces* **2013**, *5*, 13089-13095.

(14) Samuel, I. D. W.; Turnbull, G. A. Organic Semiconductor Lasers. *Chem. Rev.* **2007**, *107*, 1272-1295.

(15) Zhang, C.; Chen, P.; Hu, W. Organic Field-Effect Transistor-Based Gas Sensors. *Chem. Soc. Rev.* **2015**, *44*, 2087-2107.

(16) Wang, C.; Bunes, B. R.; Xu, M.; Wu, N.; Yang, X.; Gross, D. E.; Zang, L. Interfacial Donor–Acceptor Nanofibril Composites for Selective Alkane Vapor Detection. *ACS Sens.* **2016**, *1*, 552-559.

(17) Wu, N.; Wang, C.; Bunes, B. R.; Zhang, Y.; Slattum, P. M.; Yang, X.; Zang, L. Chemical Self-Doping of Organic Nanoribbons for High Conductivity and Potential Application as Chemiresistive Sensor. *ACS Appl. Mater. Interfaces* **2016**, *8*, 12360-12368.

(18) Che, Y.; Yang, X.; Liu, G.; Yu, C.; Ji, H.; Zuo, J.; Zhao, J.; Zang, L. Ultrathin n-Type Organic Nanoribbons With High Photoconductivity and Application in Optoelectronic Vapor Sensing of Explosives. *J. Am. Chem. Soc.* **2010**, *132*, 5743-5750.

(19) Huang, H.; Gross, D. E.; Yang, X.; Moore, J. S.; Zang, L. One-Step Surface Doping of Organic Nanofibers to Achieve High Dark Conductivity and Chemiresistor Sensing of Amines. *ACS Appl. Mater. Interfaces* **2013**, *5*, 7704-7708.

(20) Mas-Torrent, M.; Rovira, C. Novel Small Molecules for Organic Field-Effect Transistors: Towards Processability and High Performance. *Chem. Soc. Rev.* **2008**, *37*, 827-838.

(21) Wasikiewicz, J. M.; Abu-Sen, L.; Horn, A. B.; Koelewijn, J. M.; Parry, A. V. S.; Morrison, J. J.; Yeates, S. G. Towards Solution Processable Air Stable p-Type Organic Semiconductors: Synthesis and Evaluation of Mono and Di-Fluorinated Pentacene Derivatives. *J. Mater. Chem. C* **2016**, *4*, 7309-7315.

(22) Newman, C. R.; Frisbie, C. D.; da Silva Filho, D. A.; Brédas, J.-L.; Ewbank, P. C.; Mann, K. R. Introduction to Organic Thin Film Transistors and Design of n-Channel

Organic Semiconductors. *Chem. Mater.* **2004**, *16*, 4436-4451.

(23) Chua, L.-L.; Zaumseil, J.; Chang, J.-F.; Ou, E. C. W.; Ho, P. K. H.; Sirringhaus, H.; Friend, R. H. General Observation of n-Type Field-Effect Behaviour in Organic Semiconductors. *Nature* **2005**, *434*, 194-199.

(24) Wang, C.; Dong, H.; Hu, W.; Liu, Y.; Zhu, D. Semiconducting π-Conjugated Systems in Field-Effect Transistors: A Material Odyssey of Organic Electronics. *Chem. Rev.* **2012**, *112*, 2208-2267.

(25) Gelinck, G.; Heremans, P.; Nomoto, K.; Anthopoulos, T. D. Organic Transistors in Optical Displays and Microelectronic Applications. *Advanced Materials* **2010**, *22*, 3778-3798.

(26) Anthony, J. E.; Facchetti, A.; Heeney, M.; Marder, S. R.; Zhan, X. N-Type Organic Semiconductors in Organic Electronics. *Adv. Mater.* **2010**, *22*, 3876-3892.

(27) Di, C.-a.; Liu, Y.; Yu, G.; Zhu, D. Interface Engineering: An Effective Approach Toward High-Performance Organic Field-Effect Transistors. *Acc. Chem. Res.* **2009**, *42*, 1573-1583.

(28) Gao, X.; Hu, Y. Development of n-Type Organic Semiconductors for Thin Film Transistors: A Viewpoint of Molecular Design. *J. Mater. Chem C* **2014**, *2*, 3099-3117.

(29) Chan, C. K.; Kim, E. G.; Brédas, J. L.; Kahn, A. Molecular n-Type Doping of 1,4,5,8-Naphthalene Tetracarboxylic Dianhydride by Pyronin B Studied Using Direct and Inverse Photoelectron Spectroscopies. *Adv. Funct. Mater.* **2006**, *16*, 831-837.

(30) Karl, N. Charge Carrier Transport in Organic Semiconductors. *Synth. Met.* **2003**, *133–134*, 649-657.

(31) Troisi, A.; Orlandi, G. Charge-Transport Regime of Crystalline Organic Semiconductors: Diffusion Limited by Thermal Off-Diagonal Electronic Disorder. *Phys. Rev. Lett.* **2006**, *96*, 086601.

(32) Podzorov, V.; Menard, E.; Borissov, A.; Kiryukhin, V.; Rogers, J. A.; Gershenson, M. E. Intrinsic Charge Transport on the Surface of Organic Semiconductors. *Phys. Rev. Lett.* **2004**, *93*, 086602.

(33) Fishchuk, I. I.; Kadashchuk, A.; Hoffmann, S. T.; Athanasopoulos, S.; Genoe, J.; Bässler, H.; Köhler, A. Unified Description for Hopping Transport in Organic Semiconductors Including Both Energetic Disorder and Polaronic Contributions. *Phys. Rev. B: Condens. Matter Mater. Phys.* **2013**, *88*, 125202.

(34) Stoneham, A. M.; Gavartin, J.; Shluger, A. L.; Kimmel, A. V.; Ramo, D. M.; Rønnow, H. M.; Aeppli, G.; Renner, C. Trapping, Self-Trapping and the Polaron Family. *J. Phys.: Condens. Matter* **2007**, *19*, 255208.

(35) Fishchuk, I. I.; Kadashchuk, A. K.; Genoe, J.; Ullah, M.; Sitter, H.; Singh, T. B.; Sariciftci, N. S.; Bässler, H. Temperature Dependence of the Charge Carrier Mobility in Disordered Organic Semiconductors at Large Carrier Concentrations. *Phys. Rev. B: Condens. Matter Mater. Phys.* **2010**, *81*, 045202.

(36) He, X.; Zhu, G.; Yang, J.; Chang, H.; Meng, Q.; Zhao, H.; Zhou, X.; Yue, S.; Wang, Z.; Shi, J.; Gu, L.; Yan, D.; Weng, Y. Photogenerated Intrinsic Free Carriers in Small-Molecule Organic Semiconductors Visualized by Ultrafast Spectroscopy. *Sci. Rep.* **2015**, *5*, 17076.

(37) Sirringhaus, H. Organic Semiconductors: An Equal-Opportunity Conductor. *Nat. Mater.* **2003**, *2*, 641-642.

(38) Salzmann, I.; Heimel, G.; Oehzelt, M.; Winkler, S.; Koch, N. Molecular Electrical Doping of Organic Semiconductors: Fundamental Mechanisms and Emerging Dopant Design Rules. *Acc. Chem. Res.* **2016**, *49*, 370-378.

(39) Salzmann, I.; Heimel, G. Toward a Comprehensive Understanding of Molecular Doping Organic Semiconductors (Review). *J. Electron Spectrosc. Relat. Phenom.* **2015**, *204, Part A*, 208-222.

(40) Lüssem, B.; Riede, M.; Leo, K. Doping of Organic Semiconductors. *Phys. Status Solidi A* **2013**, *210*, 9-43.

(41) Maennig, B.; Pfeiffer, M.; Nollau, A.; Zhou, X.; Leo, K.; Simon, P. Controlled p-Type Doping of Polycrystalline and Amorphous Organic Layers: Self-Consistent Description of Conductivity and Field-Effect Mobility by a Microscopic Percolation Model. *Phys. Rev. B: Condens. Matter Mater. Phys.* **2001**, *64*, 195208.

(42) Méndez, H.; Heimel, G.; Winkler, S.; Frisch, J.; Opitz, A.; Sauer, K.; Wegner, B.; Oehzelt, M.; Röthel, C.; Duhm, S.; et al. Charge-Transfer Crystallites as Molecular Electrical Dopants. *Nat. Commun.* **2015**, *6*, 8560.

(43) Winkler, S.; Amsalem, P.; Frisch, J.; Oehzelt, M.; Heimel, G.; Koch, N. Probing the Energy Levels in Hole-Doped Molecular Semiconductors. *Mater. Horiz.* **2015**, *2*, 427-433.

(44) Pfeiffer, M.; Beyer, A.; Fritz, T.; Leo, K. Controlled Doping of Phthalocyanine Layers by Cosublimation With Acceptor Molecules: A Systematic Seebeck and Conductivity Study. *Appl. Phys. Lett.* **1998**, *73*, 3202-3204.

(45) Reineke, S.; Lindner, F.; Schwartz, G.; Seidler, N.; Walzer, K.; Lussem, B.; Leo, K. White Organic Light-Emitting Diodes With Fluorescent Tube Efficiency. *Nature* **2009**, *459*, 234-238.

(46) Dodabalapur, A. Organic Light Emitting Diodes. *Solid State Commun.* **1997**, *102*, 259-267.

(47) Blochwitz, J.; Pfeiffer, M.; Fritz, T.; Leo, K. Low Voltage Organic Light Emitting Diodes Featuring Doped Phthalocyanine as Hole Transport Material. *Appl. Phys. Lett.* **1998**, *73*, 729-731.

(48) Clarke, T. M.; Durrant, J. R. Charge Photogeneration in Organic Solar Cells. *Chem. Rev.* **2010**, *110*, 6736-6767.

(49) Camaioni, N.; Po, R. Pushing the Envelope of the Intrinsic Limitation of Organic Solar Cells. *J. Phys. Chem. Lett.* **2013**, *4*, 1821-1828.

(50) Savoie, B. M.; Jackson, N. E.; Chen, L. X.; Marks, T. J.; Ratner, M. A. Mesoscopic Features of Charge Generation in Organic Semiconductors. *Acc. Chem. Res.* **2014**, *47*, 3385-3394.

(51) Van Voorhis, T. Organic Semiconductors: The Birth of an Exciton. *Nat. Phys.* **2015**, *11*, 300-301.

(52) Park, S. H.; Roy, A.; Beaupre, S.; Cho, S.; Coates, N.; Moon, J. S.; Moses, D.; Leclerc, M.; Lee, K.; Heeger, A. J. Bulk Heterojunction Solar Cells with Internal Quantum Efficiency Approaching 100%. *Nat. Photonics* **2009**, *3*, 297-302.

(53) Scharber, M. C.; Mühlbacher, D.; Koppe, M.; Denk, P.; Waldauf, C.; Heeger, A. J.; Brabec, C. J. Design Rules for Donors in Bulk-Heterojunction Solar Cells—Towards 10% Energy-Conversion Efficiency. *Adv. Mater.* **2006**, *18*, 789-794.

(54) Crone, B.; Dodabalapur, A.; Gelperin, A.; Torsi, L.; Katz, H. E.; Lovinger, A. J.; Bao, Z. Electronic Sensing of Vapors With Organic Transistors. *Appl. Phys. Lett.* **2001**, *78*, 2229-2231.

(55) Duarte, D.; Dodabalapur, A. Investigation of the Physics of Sensing in Organic Field Effect Transistor Based Sensors. *J. Appl. Phys.* **2012**, *111*, 044509.

(56) Zang, L.; Che, Y.; Moore, J. S. One-Dimensional Self-Assembly of Planar π-Conjugated Molecules: Adaptable Building Blocks for Organic Nanodevices. *Acc. Chem. Res.* **2008**, *41*, 1596-1608.

(57) Chen, S.; Slattum, P.; Wang, C.; Zang, L. Self-Assembly of Perylene Imide Molecules into 1D Nanostructures: Methods, Morphologies, and Applications. *Chem. Rev.* **2015**, *115*, 11967-11998.

(58) Klug, A.; Denk, M.; Bauer, T.; Sandholzer, M.; Scherf, U.; Slugovc, C.; List, E. J. W. Organic Field-Effect Transistor Based Sensors With Sensitive Gate Dielectrics Used for Low-Concentration Ammonia Detection. *Org. Electron.* **2013**, *14*, 500-504.

(59) Li, Y.; Liu, T.; Liu, H.; Tian, M.-Z.; Li, Y. Self-Assembly of Intramolecular Charge-Transfer Compounds Into Functional Molecular Systems. *Acc. Chem. Res.* **2014**, *47*, 1186-1198.

(60) Espíldora, E.; Delgado, J. L.; Martín, N. Donor-Acceptor Hybrids for Organic Electronics. *Isr. J. Chem.* **2014**, *54*, 429-439.

(61) Wang, T.; Weerasinghe, K. C.; Sun, H.; Hu, X.; Lu, T.; Liu, D.; Hu, W.; Li, W.; Zhou, X.; Wang, L. Effect of Triplet State on the Lifetime of Charge Separation in Ambipolar D-A1-A2 Organic Semiconductors. *J. Phys. Chem C* **2016**, *120*, 11338-11349.

(62) Rao, K. P.; Kusamoto, T.; Toshimitsu, F.; Inayoshi, K.; Kume, S.; Sakamoto, R.; Nishihara, H. Double Protonation of 1,5-Bis(triarylaminoethynyl)anthraquinone to Form a Paramagnetic Pentacyclic Dipyrylium Salt. *J. Am. Chem. Soc.* **2010**, *132*, 12472-12479.

(63) Liu, C.; Wang, K.; Gong, X.; Heeger, A. J. Low Bandgap Semiconducting Polymers for Polymeric Photovoltaics. *Chem. Soc. Rev* **2016**, *45*, 4825-4846.

(64) Peet, J.; Kim, J. Y.; Coates, N. E.; Ma, W. L.; Moses, D.; Heeger, A. J.; Bazan, G. C. Efficiency Enhancement in Low-Bandgap Polymer Solar Cells by Processing With Alkane Dithiols. *Nat. Mater.* **2007**, *6*, 497-500.

(65) Gong, X.; Tong, M.; Xia, Y.; Cai, W.; Moon, J. S.; Cao, Y.; Yu, G.; Shieh, C.-L.; Nilsson, B.; Heeger, A. J. High-Detectivity Polymer Photodetectors With Spectral Response from 300 nm to 1450 nm. *Science* **2009**, *325*, 1665-1667.

(66) Abdou, M. S. A.; Orfino, F. P.; Son, Y.; Holdcroft, S. Interaction of Oxygen With Conjugated Polymers: Charge Transfer Complex Formation With Poly(3-Alkylthiophenes). *J. Am. Chem. Soc.* **1997**, *119*, 4518-4524.

(67) Adam, A. M. A.; Refat, M. S.; Sharshar, T.; Heiba, Z. K. Synthesis and Characterization of Highly Conductive Charge-Transfer Complexes Using Positron Annihilation Spectroscopy. *Spectrochim. Acta Part A* **2012**, *95*, 458-477.

(68) Pethig, R.; Soni, V. High Field Electrical Conduction in Some Organic Charge-Transfer Complexes. *J. Chem. Soc., Faraday Trans. 1* **1975**, *71*, 1534-1544.

(69) Zang, L. Interfacial Donor–Acceptor Engineering of Nanofiber Materials to Achieve Photoconductivity and Applications. *Acc. Chem. Res.* **2015**, *48*, 2705-2714.

(70) Jérome, D. Organic Conductors: From Charge Density Wave TTF−TCNQ to Superconducting (TMTSF)2PF6. *Chem. Rev.* **2004**, *104*, 5565-5592.

(71) Odom, S. A.; Caruso, M. M.; Finke, A. D.; Prokup, A. M.; Ritchey, J. A.; Leonard, J. H.; White, S. R.; Sottos, N. R.; Moore, J. S. Restoration of Conductivity With TTF-TCNQ Charge-Transfer Salts. *Adv. Funct. Mater.* **2010**, *20*, 1721-1727.

(72) Alves, H.; Molinari, A. S.; Xie, H.; Morpurgo, A. F. Metallic Conduction at Organic Charge-Transfer Interfaces. *Nat. Mater.* **2008**, *7*, 574-580.

(73) Zang, L.; Liu, R.; Holman, M. W.; Nguyen, K. T.; Adams, D. M. A Single-

Molecule Probe Based on Intramolecular Electron Transfer. *J. Am. Chem. Soc.* **2002**, *124*, 10640-10641.

(74) Stoltzfus, D. M.; Donaghey, J. E.; Armin, A.; Shaw, P. E.; Burn, P. L.; Meredith, P. Charge Generation Pathways in Organic Solar Cells: Assessing the Contribution From the Electron Acceptor. *Chem. Rev.* **2016**.

(75) Qin, T.; Zajaczkowski, W.; Pisula, W.; Baumgarten, M.; Chen, M.; Gao, M.; Wilson, G.; Easton, C. D.; Müllen, K.; Watkins, S. E. Tailored Donor–Acceptor Polymers With an A–D1–A–D2 Structure: Controlling Intermolecular Interactions to Enable Enhanced Polymer Photovoltaic Devices. *J. Am. Chem. Soc.* **2014**, *136*, 6049-6055.

(76) Kim, Y.; Cook, S.; Tuladhar, S. M.; Choulis, S. A.; Nelson, J.; Durrant, J. R.; Bradley, D. D. C.; Giles, M.; McCulloch, I.; Ha, C.-S.; et al. Strong Regioregularity Effect in Self-Organizing Conjugated Polymer Films and High-Efficiency Polythiophene:Fullerene Solar Cells. *Nat. Mater.* **2006**, *5*, 197-203.

(77) Li, G.; Shrotriya, V.; Huang, J.; Yao, Y.; Moriarty, T.; Emery, K.; Yang, Y. High-Efficiency Solution Processable Polymer Photovoltaic Cells by Self-Organization of Polymer Blends. *Nat Mater* **2005**, *4*, 864-868.

(78) Piliego, C.; Holcombe, T. W.; Douglas, J. D.; Woo, C. H.; Beaujuge, P. M.; Fréchet, J. M. J. Synthetic Control of Structural Order in N-alkylthieno[3,4-C]pyrrole-4,6-Dione-Based Polymers for Efficient Solar Cells. *J. Am. Chem. Soc.* **2010**, *132*, 7595-7597.

(79) Kanimozhi, C.; Yaacobi-Gross, N.; Chou, K. W.; Amassian, A.; Anthopoulos, T. D.; Patil, S. Diketopyrrolopyrrole–Diketopyrrolopyrrole-Based Conjugated Copolymer for High-Mobility Organic Field-Effect Transistors. *J. Am. Chem. Soc.* **2012**, *134*, 16532-16535.

(80) Lunt, R. R.; Benziger, J. B.; Forrest, S. R. Relationship Between Crystalline Order and Exciton Diffusion Length in Molecular Organic Semiconductors. *Adv. Mater.* **2010**, *22*, 1233-1236.

(81) Lunt, R. R.; Giebink, N. C.; Belak, A. A.; Benziger, J. B.; Forrest, S. R. Exciton Diffusion Lengths of Organic Semiconductor Thin Films Measured by Spectrally Resolved Photoluminescence Quenching. *J. Appl. Phys.* **2009**, *105*, 053711.

(82) Shtein, M.; Mapel, J.; Benziger, J. B.; Forrest, S. R. Effects of Film Morphology and Gate Dielectric Surface Preparation on the Electrical Characteristics of Organic-Vapor-Phase-Deposited Pentacene Thin-Film Transistors. *Appl. Phys. Lett.* **2002**, *81*, 268-270.

(83) Peet, J.; Senatore, M. L.; Heeger, A. J.; Bazan, G. C. The Role of Processing in the Fabrication and Optimization of Plastic Solar Cells. *Adv. Mater.* **2009**, *21*, 1521-1527.

(84) Ma, W.; Yang, C.; Gong, X.; Lee, K.; Heeger, A. J. Thermally Stable, Efficient Polymer Solar Cells with Nanoscale Control of the Interpenetrating Network Morphology. *Adv. Funct. Mater.* **2005**, *15*, 1617-1622.

(85) Kamkar, D. A.; Wang, M.; Wudl, F.; Nguyen, T.-Q. Single Nanowire OPV Properties of a Fullerene-Capped P3HT Dyad Investigated Using Conductive and Photoconductive AFM. *ACS Nano* **2012**, *6*, 1149-1157.

(86) Würthner, F. Perylene Bisimide Dyes as Versatile Building Blocks for Functional Supramolecular Architectures. *Chem. Commun.* **2004**, 1564-1579.

(87) Ahrens, M. J.; Fuller, M. J.; Wasielewski, M. R. Cyanated Perylene-3,4-Dicarboximides and Perylene-3,4:9,10-Bis(dicarboximide): Facile Chromophoric Oxidants for Organic Photonics and Electronics. *Chem. Mater.* **2003**, *15*, 2684-2686.

(88) Lukas, A. S.; Zhao, Y.; Miller, S. E.; Wasielewski, M. R. Biomimetic Electron Transfer Using Low Energy Excited States: A Green Perylene-Based Analogue of Chlorophyll A. *J. Phys. Chem. B* **2002**, *106*, 1299-1306.

(89) Zhao, Y.; Wasielewski, M. R. 3,4:9,10-Perylenebis(dicarboximide) Chromophores That Function as Both Electron Donors and Acceptors. *Tetrahedron Lett.* **1999**, *40*, 7047-7050.

(90) Chesterfield, R. J.; McKeen, J. C.; Newman, C. R.; Ewbank, P. C.; da Silva Filho, D. A.; Brédas, J.-L.; Miller, L. L.; Mann, K. R.; Frisbie, C. D. Organic Thin Film Transistors Based on N-Alkyl Perylene Diimides: Charge Transport Kinetics as a Function of Gate Voltage and Temperature. *J. Phys. Chem. B* **2004**, *108*, 19281-19292.

(91) Chen, H. Z.; Ling, M. M.; Mo, X.; Shi, M. M.; Wang, M.; Bao, Z. Air Stable n-Channel Organic Semiconductors for Thin Film Transistors Based on Fluorinated Derivatives of Perylene Diimides. *Chem. Mater.* **2007**, *19*, 816-824.

(92) Balakrishnan, K.; Datar, A.; Oitker, R.; Chen, H.; Zuo, J.; Zang, L. Nanobelt Self-Assembly from an Organic n-Type Semiconductor: Propoxyethyl-PTCDI. *J. Am. Chem. Soc.* **2005**, *127*, 10496-10497.

(93) Balakrishnan, K.; Datar, A.; Naddo, T.; Huang, J.; Oitker, R.; Yen, M.; Zhao, J.; Zang, L. Effect of Side-Chain Substituents on Self-Assembly of Perylene Diimide Molecules: Morphology Control. *J. Am. Chem. Soc.* **2006**, *128*, 7390-7398.

(94) Datar, A.; Oitker, R.; Zang, L. Surface-Assisted One-Dimensional Self-Assembly of a Perylene Based Semiconductor Molecule. *Chem. Commun.* **2006**, 1649-1651.

(95) Briseno, A. L.; Mannsfeld, S. C. B.; Reese, C.; Hancock, J. M.; Xiong, Y.; Jenekhe, S. A.; Bao, Z.; Xia, Y. Perylenediimide Nanowires and Their Use in Fabricating Field-Effect Transistors and Complementary Inverters. *Nano Lett.* **2007**, *7*, 2847-2853.

(96) Che, Y.; Yang, X.; Balakrishnan, K.; Zuo, J.; Zang, L. Highly Polarized and Self-

Waveguided Emission from Single-Crystalline Organic Nanobelts. *Chem. Mater.* **2009**, *21*, 2930-2934.

(97) Pisula, W.; Kastler, M.; Wasserfallen, D.; Robertson, J. W. F.; Nolde, F.; Kohl, C.; Müllen, K. Pronounced Supramolecular Order in Discotic Donor–Acceptor Mixtures. *Angew. Chem., Int. Ed.* **2006**, *45*, 819-823.

(98) Huang, H.; Chou, C.-E.; Che, Y.; Li, L.; Wang, C.; Yang, X.; Peng, Z.; Zang, L. Morphology Control of Nanofibril Donor–Acceptor Heterojunction to Achieve High Photoconductivity: Exploration of New Molecular Design Rule. *J. Am. Chem. Soc.* **2013**, *135*, 16490-16496.

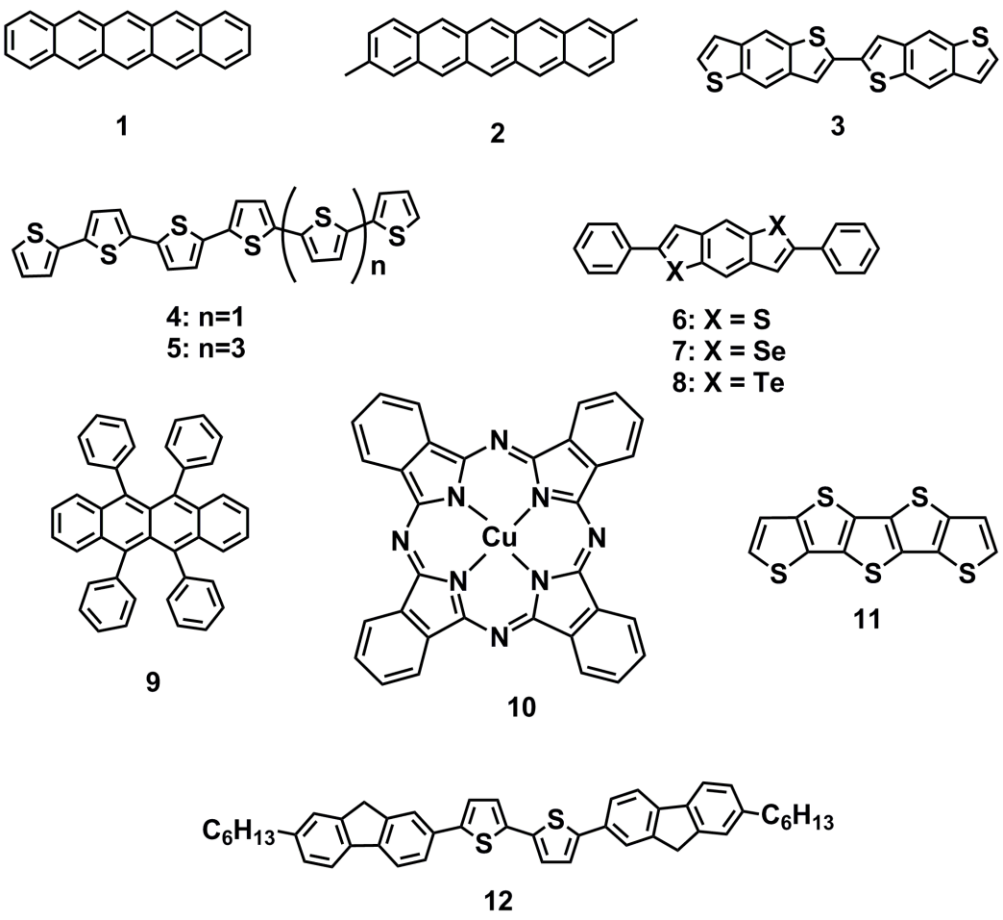

Figure 1.1 Chemical structures of some typical p-type organic semiconductors.

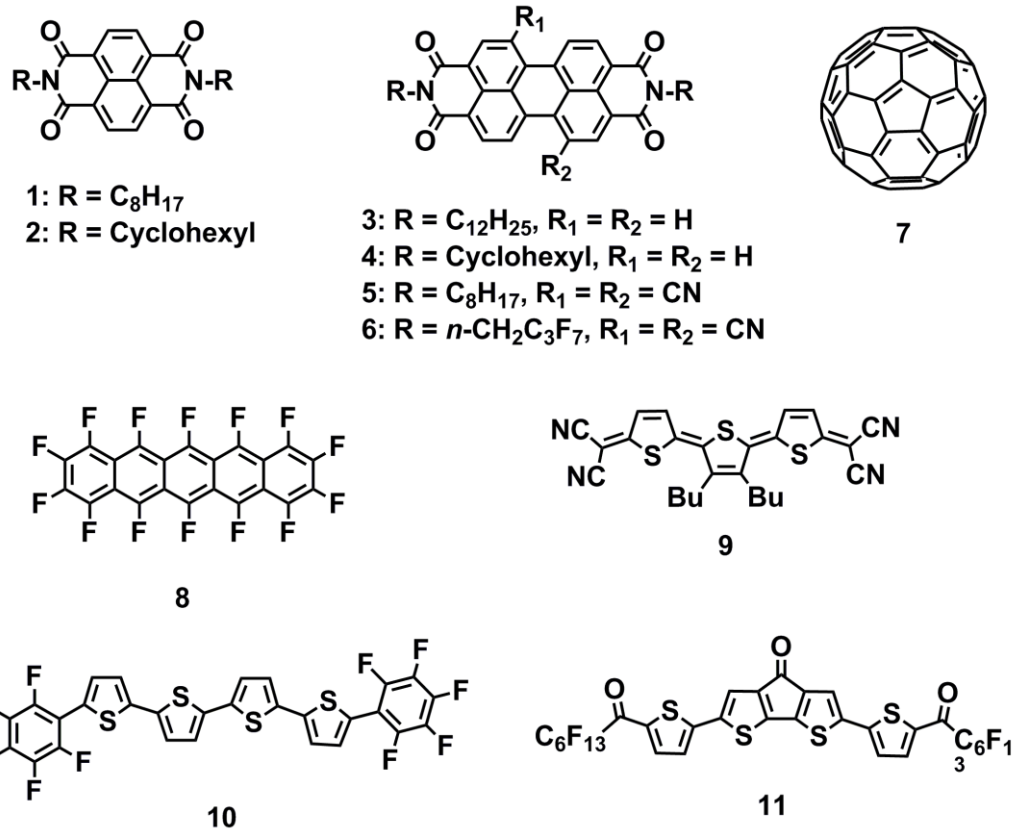

Figure 1.2 Chemical structures of some n-type organic semiconductors.

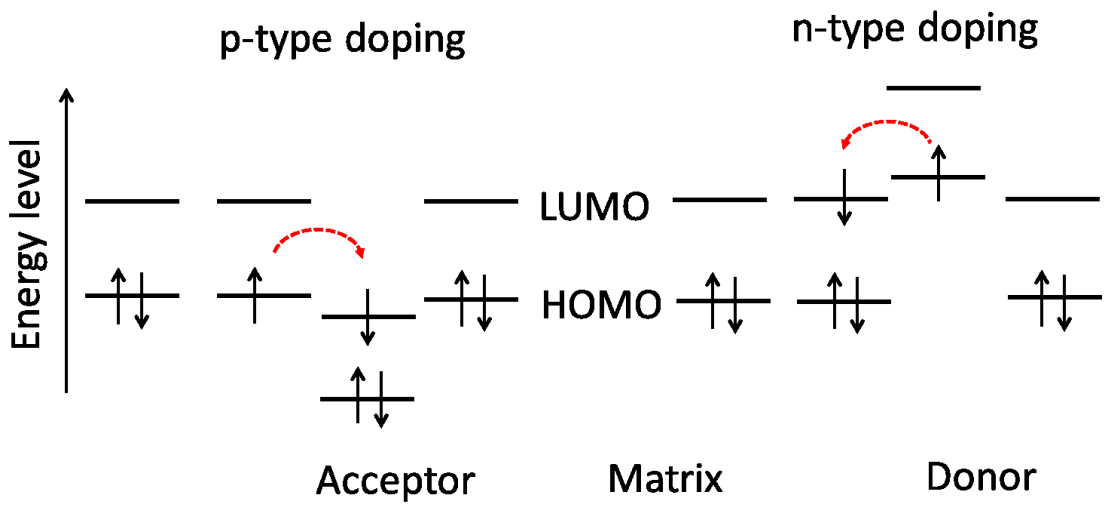

Figure 1.3 Schematic of doping mechanism in organic semiconductors.

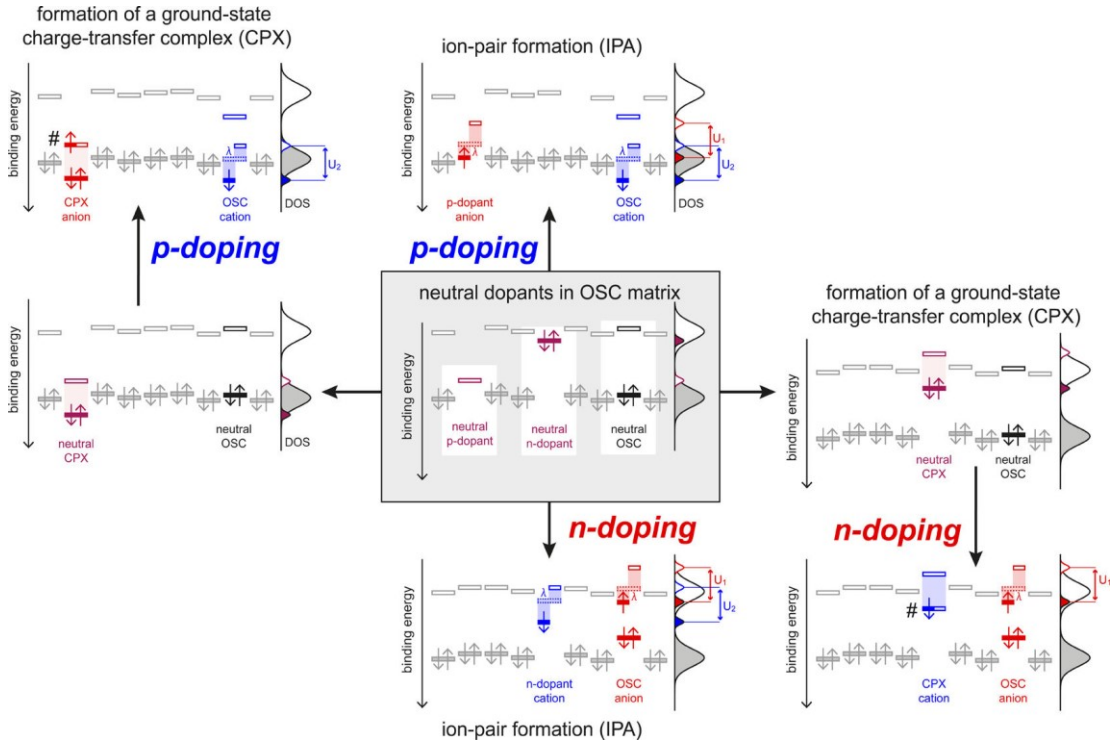

Figure 1.4 Schematic demonstrations of energy levels and the corresponding density of states of p- and n-doping in the case of IPA and the formation of CTCs with their subsequent ionization. Adapted from ref 38, published 2016 by the ACS Publications.

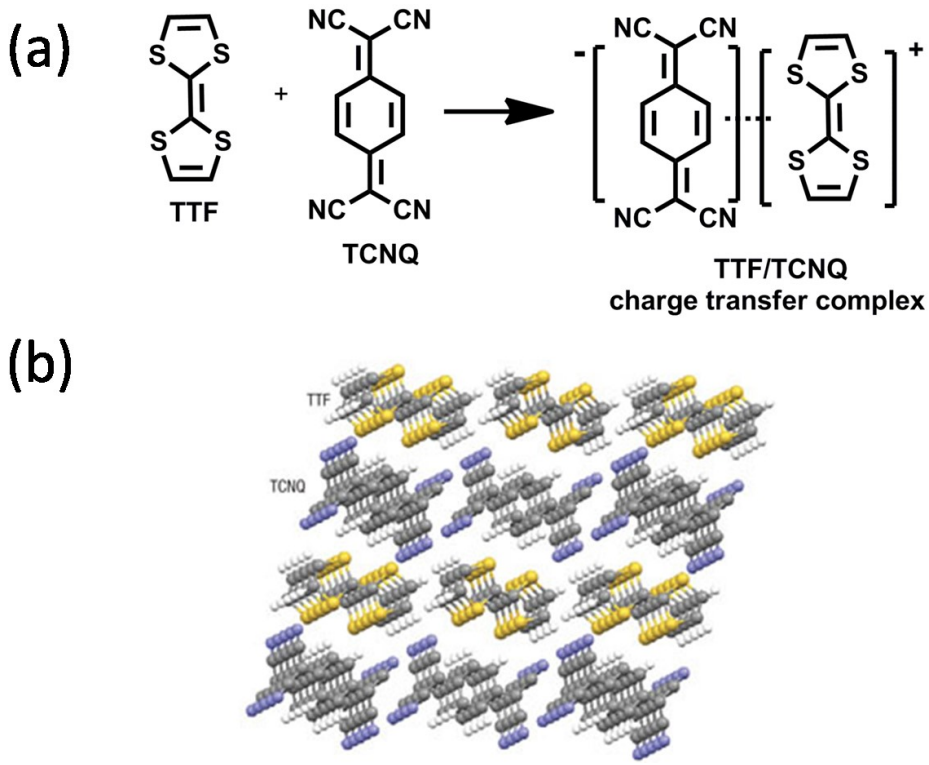

Figure 1.5 A prototype charge-transfer compound TTF-TCNQ: (a) schematic illustration of formation of TTF-TCNQ charge transfer complex; (b) arrangement of the TTF and TCNQ molecules in a crystal. Adapted from ref 72, published 2008 by the Nature Publishing Group.

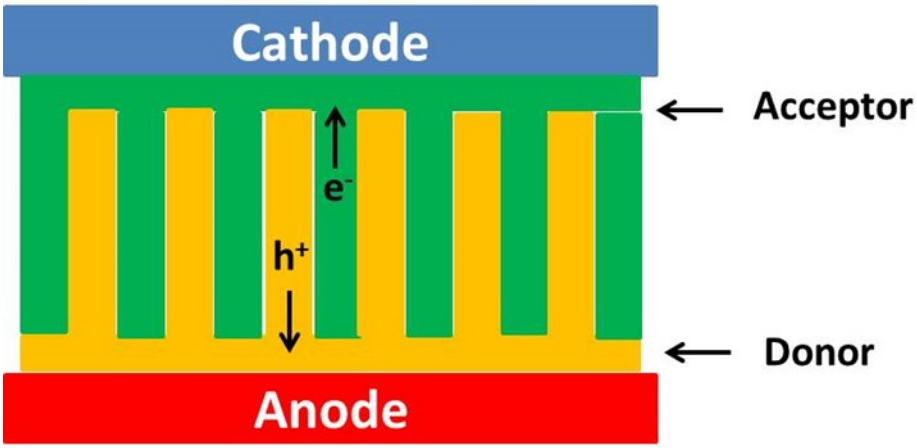

Figure 1.6 The ideal structure of a BHJ organic solar cell. Adapted from ref 10, published 2007 by the ACS Publications.

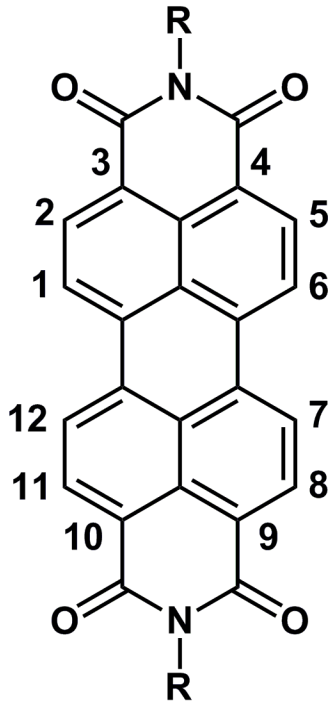

Figure 1.7 Chemical structure of a PTCDI molecule.

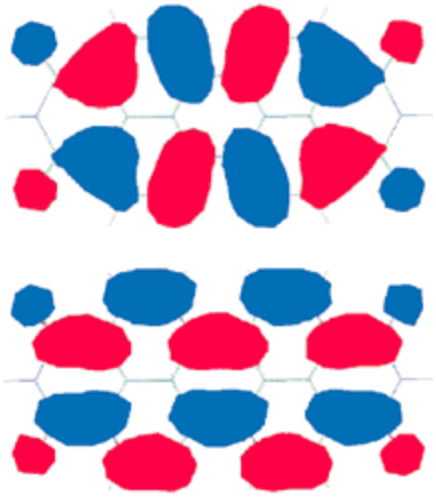

Figure 1.8 The frontier orbitals of the highest occupied molecular orbital (HOMO) (top) and lowest unoccupied molecular orbital (LUMO) (bottom) of PTCDI. Adapted from ref 86, published 2004 by The Royal Society of Chemistry.

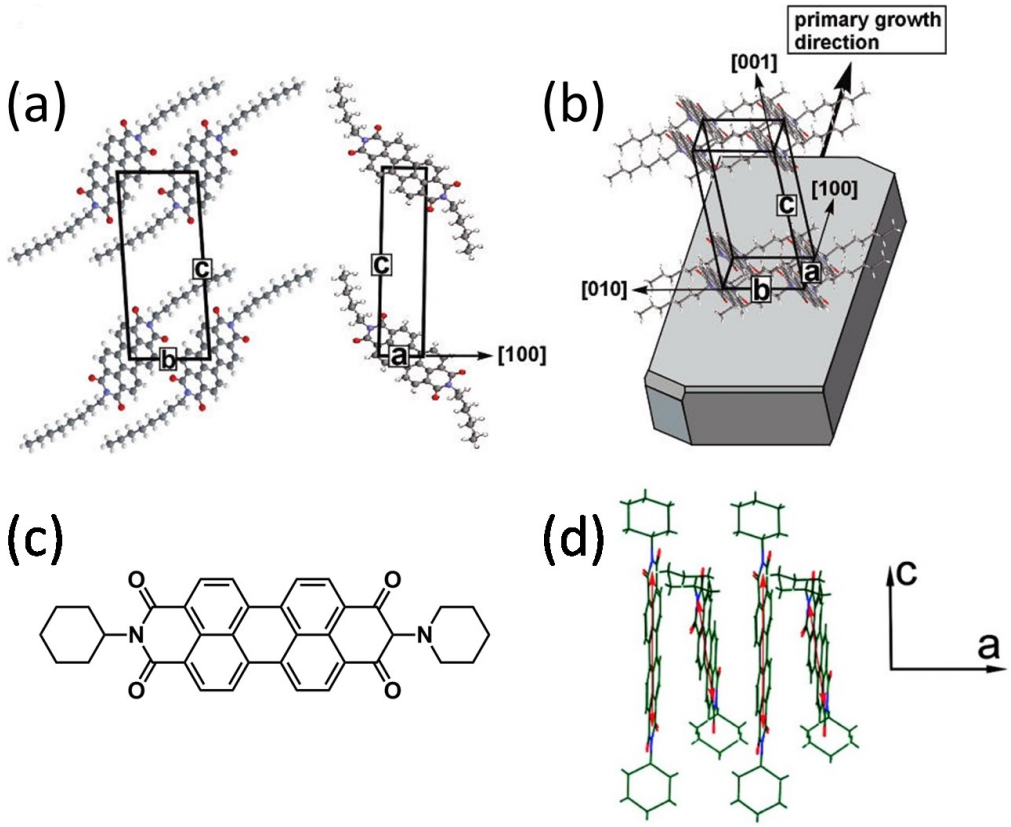

Figure 1.9 Molecular and crystal structure of PTCDIs: (a) the PTCDI-C8 unit cell as gained by single-crystal X-ray diffraction; (b) the theoretically predicated PTCDI-C8 crystal growth direction (adapted from ref 95, published 2007 by the ACS Publications); (c) the chemical structure of CH-PTCDI; (d) the filp-flap molecular stacking along the [100] direction (adapted from ref 96, published 2009 by the ACS Publications).

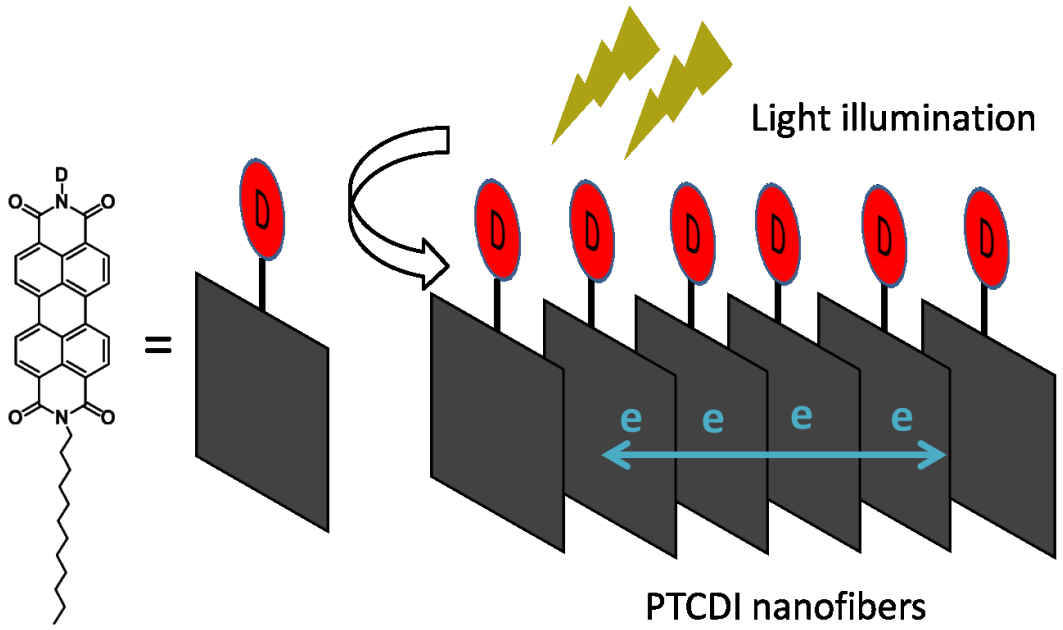

Figure 1.10 A schematic diagram showing the electron transport properties in PTCDI nanofibers with D-A structure.

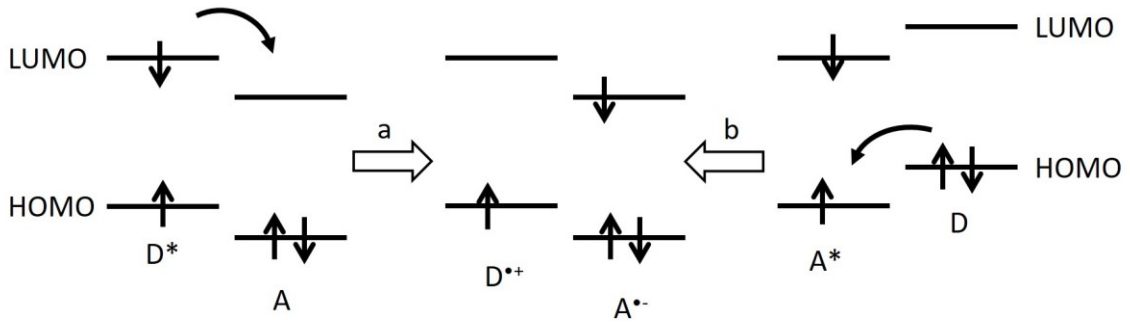

Figure 1.11 Photoinduced electron transfer between donor and acceptor with two possible processes: (a) electron transfers from excited donor to PTCDI or (b) electron moves from donor to excited PTCDI molecules.

Table 1.1 Calculated diffusion lengths (L_D) for singlet (S) and triplet (T) excitons of crystalline (C.) and amorphous (Amorph.) films (adapted from refer 81, published 2009 by the AIP Publishing).

Material	Exciton	Crystallinity (Orientation)	L_D (nm)
NPD	S	Amorph.	5.1 ($\pm$1.0)
CBP	S	Amorph.	16.8 ($\pm$0.8)
SubPc	S	Amorph.	8.0 ($\pm$0.3)
PTCDA	S	C.-55 nm (flat)	10.4 ($\pm$1.0)
DIP	S	C.- > 150 nm (upright)	16.5 ($\pm$0.4)
DIP	S	C.-30 nm (flat)	21.8 ($\pm$0.6)
PtOEP	T-Mon.	C.- > 150 nm (upright)	18.0 ($\pm$0.6)
PtOEP	T-Dim.	C. - > 150 nm (upright)	13.1 ($\pm$0.5)

CHAPTER 2

CHEMICAL SELF-DOPING OF ORGANIC NANORIBBONS FOR HIGH CONDUCTIVITY AND POTENTIAL APPLICATION AS CHEMIRESISTIVE SENSOR[1]

2.1 Abstract

Intrinsically low electrical conductivity of organic semiconductors hinders their further development into practical electronic devices. Herein, we report on an efficient chemical self-doping to increase the conductivity through one-dimensional (1D) stacking arrangement of electron donor-acceptor (D-A) molecules. The D-A molecule employed was a 1-methylpiperidine-substituted perylene tetracarboxylic diimide (MP-PTCDI), of which the methylpiperidine moiety is a strong electron donor, and can form a charge transfer complex with PTCDI (acting as the acceptor), generating anionic radical of PTCDI as evidenced in molecular solutions. Upon self-assembling into nanoribbons through columnar π–π stacking, the intermolecular charge transfer interaction between methylpiperidine and PTCDI would be enhanced, and the electrons generated are

[1] Reprinted with permission from Wu, N.; Wang, C.; Bunes, B. R.; Zhang, Y.; Slattum, P. M.; Yang, X.; Zang, L., Chemical Self-doping of Organic Nanoribbons for High Conductivity and Potential Application as Chemiresistive Sensor. *ACS Appl. Mater. Interfaces* **2016**, *8*, 12360-12368. Copyright (2016) American Chemical Society.

delocalized along the π–π stacking of PTCDIs, leading to enhancement in conductivity. The conductive fiber materials thus produced can potentially be used as chemiresistive sensor for vapor detection of electron deficient chemicals such as hydrogen peroxide, taking advantage of the large surface area of nanofibers. As a major component of improvised explosives, hydrogen peroxide remains a critical signature chemical for public safety screening and monitoring.

2.2 Introduction

Organic semiconductors are an alternative to conventional inorganic semiconductors, and offer advantages such as mechanical flexibility and ease of solution processing. They have been applied in varying electronic devices, including organic field-effect transistors (OFETs),[1] organic light-emitting diodes (OLEDs),[2] photovoltaics,[3] photodetectors,[4] and sensors.[5,6] Unfortunately, their intrinsically low electrical conductivity,[7] due to properties such as the closed-shell electronic structures of the individual organic molecules and weak intermolecular interactions, hinders further development and more widespread applications. Studies have shown that electrical doping of organic semiconductors is an effective strategy to overcome this limitation,[8] enhancing conductivity by many orders of magnitude. Doping requires matched energy levels (redox potentials) between the host molecules and dopants.[8] Hence, the number of dopants is limited. Common dopants are small molecules like O_2,[9] Br_2, I_2,[10] and larger molecules, such as F4-TCNQ (perfluorinated tetracyanoquinodimethane),[11] and pyronin B.[12] Nevertheless, all of these are interstitial dopants which are mobile in the host materials,[8] so the electrical properties of the doped organic semiconductors may change in time as the dopants diffuse.

Therefore, exploration of a new type of dopant is important for achieving high quality organic semiconductor materials.

Substitutional n-type doping was previously achieved by introducing a zwitterionic dopant to the perylene tetracarboxylic diimide (PTCDI) molecules.[13-15] The dopant was a reduced species (anionic radical) of the host molecule, so they did not significantly alter the crystal structure and were fixed in the semiconductor lattice. The conductivity was dependent on the concentration of dopant and showed large enhancement even with small amount of dopants. Anionic radicals of PTCDI molecules can also be generated by interacting with reducing agent like hydrazine.[16] After exposure to hydrazine vapor, the nanobelts self-assembled from PTCDIs increased conductivity because of the formation of PTCDI anionic radicals, which provide electrons as the major charge carrier rapidly migrating along the long axis of nanobelt through π–π delocalization. With the similar process and mechanism, OFETs based on hydrazine doped PTCDI molecules were fabricated to achieve lower operating voltages and higher conductivity.[17]

Inspired by these works, we designed PTCDI molecules substituted with 1-methylpiperidine (MP) to construct self-doped semiconductor through one-dimensional (1D) self-assembly of the molecules into nanoribbons structure. The methylpiperidine moiety on one molecule, a strong electron donor (D), interacted with PTCDI on the other molecule (acting as the electron acceptor, A), generating anionic radicals of PTCDI. The resultant radicals functioned as the n-type dopants located in the lattice of the PTCDI semiconductors.[13-15] The similar side-group induced self-doping has also been widely exploited in conducting polymer materials, e.g., polyaniline.[18,19] The nanoribbon structure, dominated by the π–π stacking between the PTCDI planes, provides an

efficient pathway for long-range charge transport.[20] The nanoribbons reported in this study exhibited four orders of magnitude higher current compared to the 1D nanomaterials assembled from other PTCDI molecules under the same test conditions.[21]

With high conductivity, the n-type PTCDI nanoribbons can potentially be developed as a chemiresistive sensor for detection of electron deficient chemicals with a high signal-to-noise ratio, providing more reliable output signal and lower limit of detection. As indeed evidenced in this study, the PTCDI nanoribbons demonstrate sensitive chemiresistive response to the hydrogen peroxide (H_2O_2) vapor, enabling potential application in detection of improvised explosives, such as triacetone triperoxide (TATP), diacetone diperoxide (DADP), hexamethylene triperoxide diamine (HMTD), and simple liquid mixtures of concentrated hydrogen peroxide and fuels (e.g., alcohols, acetone).[22] H_2O_2 is commonly used as the chemical marker of these peroxide explosives. Current techniques for detecting H_2O_2 are fluorometric,[22-24] colorimetric,[25] and electrochemical methods,[26] but most of them are limited to detection in the liquid phase. It is still challenging to detect H_2O_2 vapor at trace level. The chemiresistive sensing technique has the advantages of trace vapor detection and enables fabricating a portable, low-power and simple sensor device.[27,28]

2.3 Experimental Section

2.3.1 Synthesis of N-dodecyl-N'-[(1-methylpiperidine-4-yl) methyl]-perylene-3,4,9,10-tetracarboxylic Diimide

The precursor compound, N-dodecyl-perylene-3,4,9,10-tetracarboxylic monoimide monoanhydride (Compound 1, Figure 2.1), was synthesized using a previous method.[21]

Subsequently, Compound 1 (100 mg), (1-methyl-4-piperidinyl)methanamine (Sigma-Aldrich, 71.3 mg), zinc acetate (Sigma-Aldrich, ACS reagent, 98%, 3.0 mg) and imidazole (Sigma-Aldrich, ACS reagent, > 99%, 1.5 g) were combined and heated to 150 °C for 8 hours. After cooling to room temperature, the reaction mixture was dispersed in 10% HCl (Fisher Chemical, 36.5 to 38.0%, w/w) solution to solubilize the imidazole, the insoluble product was collected by filtration and washed with water and methanol. The crude product was converted to the free base by dissolving in chloroform and washing with 10% NaOH (Sigma-Aldrich, ACS reagent, > 97.0%) solution. The organic layer was washed with water and dried over anhydrous Na_2SO_4 (Sigma-Aldrich, ACS reagent, > 99%). The reaction mixture was then purified by silica gel chromatography using 6.0% ethanol in chloroform as the eluent followed by recrystallization from chloroform/ethanol to give final product (54.7 mg, 46%). ^{1}H NMR (500 MHz, $CDCl_3$, TMS, ppm): δ = 8.65 (d, J = 8.0 Hz, 4H; perylene H), 8.57 (d, J = 8.0 Hz, 4H; perylene H), 4.21–4.14 (m, 4H; $(CO)_2NCH_2$), 2.87 (m, 2H; CHH*N(CH_3)CHH*), 2.26 (s, 3H; NCH_3), 1.96–1.88 (m, 2H; CH*HN(CH_3)CH*H), 1.79–1.71 (m, 4H; $(CH2*)_2CHCH_2N$), 1.34–1.22 (m, 21H,10CH_2, CH), 0.87 (t, J = 6.84 Hz, 3H; CH_3); ^{13}C NMR (125 MHz, $CDCl_3$, TMS, ppm): δ = 173.26, 163.88, 163.53, 137.05, 134.87, 134.70, 131.72, 131.56, 129.62, 129.54, 126.62, 123.60, 123.39, 123.32, 123.26, 116.49, 115.30, 55.65, 46.52, 40.95, 32.13, 30.46, 29.91, 29.84, 29.77, 29.60, 29.56, 28.34, 27.39, 22.89, 14.31. MALDI-TOF-MS: $[M+H^+]/z$ = 670.35.

2.3.2 Fabrication of Nanoribbons

Self-assembly of the MP-PTCDI molecules was performed through a solvent exchange process from a "good" solvent to a "bad" solvent, where the molecules have limited solubility in the "bad" solvent and thus self-assemble into one-dimensional nanostructures via molecular stacking.[21] In this study, we used a solution injection method to conduct the self-assembly in ethanol. Typically, 0.4 mL of MP-PTCDI solution (1.5 mmol L^{-1}) in chloroform was injected rapidly into a larger volume of ethanol (4 mL) and placed in the dark for 5 h. The nanoribbons were then transferred to substrates for further characterization and electrical measurements. Synthesis of MA-PTCDI and MO-PTCDI, and self-assembly into nanoribbons were performed according to the previously reported methods.[21] Synthesis of CH-PTCDI molecules and self-assembly into nanobelts were based on the previously reported methods.[29]

2.3.3 Materials Characterization

UV-Vis absorption spectra were collected with an Agilent Cary 100. Fluorescence spectra were acquired on an Agilent Eclipse spectrophotometer. AFM measurements were carried out on a Veeco MultiMode V scanning probe microscope in tapping mode. SEM measurement was performed with an FEI Nova Nano 630 (FEI Corporation) with a helix detector in low vacuum (0.43 Torr water pressure). To make samples for either AFM or SEM measurements, the MP-PTCDI nanoribbons were directly transferred from ethanol and deposited onto a silicon substrate coated with a polished 300 nm thick SiO_2 layer, and then dried in vacuum oven at room temperature in the dark. The bright field and fluorescence optical images were obtained with a Leica DMI4000B inverted

microscope equipped with an Acton SP-2356 Imaging Spectrograph system and Princeton Instrument Acton PIXIS: 400B Digital CCD Camera System for high resolution imaging

2.3.4 Current Measurement

Interdigitated electrodes (IDE) were used for all current measurements in this work. The IDE has a channel width of 2100 μm and a gap length of 50 μm, and was fabricated by a standard photolithography procedure on a silicon wafer with a 300 nm thermal oxide layer (Silicon Quest International). The electrodes were made by sputtering with 20 nm titanium adhesion layer and 50 nm gold layer. MP-PTCDI nanoribbons were deposited onto IDE by drop-casting, followed by drying in vacuum oven at room temperature in the dark. The electrical conductivity was measured under ambient conditions using a two-probe method on a Signatone S-1160 Probe Station combined with an Agilent 4156C Precision Semiconductor Analyzer. To compare the conductivity of different PTCDI nanomaterials, the nanofibers were assembled by injecting a given molar amount of PTCDI (12 nmol dissolved in a minimal volume of $CHCl_3$) into 100 μL ethanol. The nanofibers thus assembled were dispersed well in ethanol, which were then transferred onto the IDE by slow drop-casting to ensure uniform coverage over the whole IDE area. To compare the current enhancement ratio after surface coating with amines, 12 nmol of CH-PTCDI nanobelts were chosen as the standard, zero-doping material, and deposited onto the IDE. 1 μL of methanol solution containing different concentrations of the amines (1-methylpiperidine, TCI America, > 99.0%; hexylamine, Acros Organics, 99%; triethylamine, Sigma-Aldrich, 99%; aniline, Acros Organics, 99.5%, extra pure) were

drop cast onto the surface of the CH-PTCDI nanobelts, providing the varying molar amount of amine coated on the surface. To avoid the oxidation of amines during processing, the fresh amine solution was made for each measurement. ^{1}H NMR measurements were conducted for all the amines during the project period to assure that the high purity of amines remained throughout the experiments. 1-Methylpiperidine: ^{1}H NMR (300 MHz, $CDCl_3$, TMS, ppm): δ = 2.26 (m, 4H, CH_2CH_2*N), δ = 2.17 (s, 3H, NCH_3), δ = 1.52 (m, 4H, CH_2CH_2*CH_2), δ = 1.35 (m, 2H, CH_2CH_2*CH_2). Hexylamine: ^{1}H NMR (300 MHz, $CDCl_3$, TMS, ppm): δ = 2.64 (t, J = 6.0 Hz, 2H, NH_2), δ = 1.40–1.17 (m, 10H, $(CH_2)_5$), δ = 0.85 (t, J = 6.0 Hz, 3H, CH_3). Triethylamine: ^{1}H NMR (300 MHz, $CDCl_3$, TMS, ppm): δ = 2.49 (q, J = 6.0 Hz, 6H, CH_2), δ = 0.99 (t, J = 6.0 Hz, 9H, CH_3). Aniline: ^{1}H NMR (300 MHz, $CDCl_3$, TMS, ppm): δ = 7.20 (t, J = 6.0 Hz, 2H, CHCH*CH), δ = 6.80 (t, J = 6.0 Hz, 1H, CHCH*CH), δ = 6.72 (d, J = 6.0 Hz, 2H, CCH*CH), δ = 3.65 (s, 2H, NH_2).

2.3.5 Chemical Vapor Sensing Measurement

All chemical vapor sensing tests were conducted under ambient conditions in the dark. Figure 2.2 depicts the sensing and chemical vapor delivery systems. A certain amount of chemical vapor was pulled into a 50 mL syringe and delivered by syringe pump (NE-4000 New Era Pump System, Inc.) at a rate of 25 mL min^{-1} into the carrier gas. The carrier gas was dry air with a flow rate of 475 mL min^{-1}. The final concentration of chemical vapor in the testing chamber was calculated from the syringe volume and the concentration of original chemical vapor. The original H_2O_2 vapor was generated from 44.7 wt.% H_2O_2 solution (Sigma-Aldrich, 50 wt.% in H_2O).[30] The IDE chip (deposited

with PTCDI nanomaterials) was placed on a ceramic chip carrier connected by wire bonding. The ceramic chip carrier was fixed on a breadboard, enclosed in a small Teflon chamber (3.84 cm in length, 1.86 cm in width, and 2.41 cm in height), and connected to an Agilent 4156C Semiconductor Analyzer. A bias of 10 V was applied across the electrodes and the current through the sensor was monitored. For H_2O_2 testing, the chip was exposed to H_2O_2 vapor for 30 s with a recovery time of 2.5 min. For testing toward the common liquid samples, the exposure time was 30 s with a recovery time of 30 s. The sensing response time of MP-PTCDI nanoribbons was obtained by fitting the time-course current change profile to an exponential function,[31] which gives the response time as 1/e of the time constant obtained.

2.4 Results and Discussion

2.4.1 Synthesis of MP-PTCDI Molecules and Self-Assembly Into Nanoribbons

PTCDI-based molecules have been extensively explored for 1D self-assembly and optoelectronic applications in recent years.[20,32-35] Side-chain substitutions do not significantly influence the electronic property of the PTCDI backbone because the two imide positions in the PTCDI molecules are nodes in the π-orbitals.[32,36] This allows for comparative study of the PTCDI materials, for which the side-chain substitutions play an important role in intermolecular interactions, resulting in different electronic properties through charge transfer.[37] In this study, a PTCDI molecule substituted with 1-methylpiperidine moiety (Figure 2.3, denoted as MP-PTCDI) was designed and synthesized. The MP-PTCDI nanoribbons were fabricated using the previously reported

solution phase self-assembly method.[20,21,35] The morphology of MP-PTCDI nanoribbons was characterized by SEM and AFM (Figure 2.4). The nanoribbons are several micrometers in length and 100–300 nm in width. The thickness of the nanoribbons is estimated to be just about 15 nm (Figure 2.4b, AFM images and height-profile). Such shape-defined 1D nanoribbon structures are conducive to the construction of electronic devices. For comparative study, two other PTCDI molecules, MA-PTCDI and MO-PTCDI (both substituted with the same dodecyl alkyl chain, but with different groups on the other end, as shown in Figure 2.3), were also synthesized and assembled into nanoribbon structures following the previous reported methods.[21] Owing to the similar molecular structure, the two reference PTCDIs formed about the same nanoribbon morphology as the MP-PTCDI (see Table 2.1). The dimethylaniline moiety of MA-PTCDI acts as a strong electron donor under photoexcitation, whereas the methoxyphenyl is not an effective donor to PTCDI as evidenced from our previous investigation.[21] In the next section, we compared the electrical conductivity of the nanoribbons assembled from the three PTCDI building blocks shown in Figure 2.3, aiming to explore the effects of the side groups on self-doping.

2.4.2 High Conductivity and Mechanism Study

As shown in Figure 2.5, MP-PTCDI nanoribbons possess the highest electrical conductivity; the current of the MP-PTCDI nanoribbons is four orders of magnitude higher than the other PTCDI nanoribbon materials under the same test conditions. Considering the similar nanoribbon structures formed from the three PTCDIs (Table 2.1) and the fact that the π-electronic property of PTCDI backbone remains unchanged with

different side-substitutions, we concluded that the high conductivity observed for MP-PTCDI nanoribbons is largely caused by the methylpiperidine moiety.[19]

To gain insight into the high conductivity of MP-PTCDI nanoribbons, a case study model was constructed by coating 1-methylpiperidine molecules on N,N-di(cyclohexyl)-perylene-3,4,9,10-tetracarboxylic diimide (CH-PTCDI) nanobelts to investigate the influence of this specific substitution group on the conductivity of one-dimensional PTCDI nanomaterials.[38,39] The CH-PTCDI was selected because the cyclohexyl side-chain groups are neutral and inactive in charge transfer interaction, and the shape defined nanobelts can be easily fabricated from this molecule with high reproducibility.[29] In this study, 12 nmol of CH-PTCDI nanobelts were deposited onto interdigitated electrodes (IDEs) patterned on a silicon wafer, and a controlled amount of 1-methylpiperidine was drop-cast onto the nanobelts (Figure 2.6a). Negligible currents were measured for either pristine CH-PTCDI nanobelts (0.0012 nA at a bias of 10 V, Figure 2.7) or pure 1-methylpiperidine film drop-cast from 4 μmol amount (0.0055 nA at a bias of 10 V, Figure 2.7). In contrast, a much increased current was observed for the CH-PTCDI nanobelts coated with only 2 μmol of 1-methylpiperidine (0.45 nA at a bias of 10 V, Figure 2.7). The current increased further when more 1-methylpiperidine was deposited. The current increased to 32.5 μA, an enhancement ratio of 2×10^7 compared to the pristine nanobelt, when 4 μmol of 1-methylpiperidine was deposited (Figure 2.6b). An enhancement ratio of 8×10^6 was observed when 8 μmol of 1-methylpiperidine was deposited, indicating that the current increase started to reach saturation when more than 4 μmol of 1-methylpiperidine was cast (Figure 2.6b). This significant increase in conductivity is likely due to the chemical doping, which occurs through the donor-

acceptor (charge transfer) interaction between 1-methylpiperidine and PTCDI.

The morphology of the CH-PTCDI nanobelts before and after surface coating remained unchanged as characterized by SEM (Figure 2.6c, d). Interestingly, the built up surface charging on the pristine CH-PTCDI nanobelts was eliminated by surface coating with 1-methylpiperidine. The SEM image of pristine CH-PTCDI nanobelts shows bright imaging contrast on the surface of the nanobelts, which is a characteristic of the surface charge built up on the nonconductive sample after E-beam exposure during SEM measurement (Figure 2.6c).[40] However, such surface charging was suppressed after surface coating of the 1-methylpiperidine (Figure 2.6d). This phenomenon is common in SEM measurement performed on nonconductive samples, for which a thin layer of metal, such as Au, Pt, or Pd, is typically deposited on the sample surface to facilitate charge transmission and prevent charge building up.[40,41] Since the pure 1-methylpiperidine film is little conductive (Figure 2.7), the observed conductivity improvement should be due to the charge transfer interaction between 1-methylpiperidine and CH-PTCDI nanobelts, consistent with the current enhancement discussed above.

The charge transfer interaction between 1-methylpiperidine and CH-PTCDI was also confirmed by the fluorescence quenching measurements of PTCDI. MP-PTCDI solution in chloroform exhibits strong fluorescence emission, comparable to CH-PTCDI molecules in chloroform (Figure 2.8),[29] indicating that there is no intramolecular electron transfer in the MP-PTCDI molecule. However, no fluorescence emission was observed for the nanoribbons fabricated from the MP-PTCDI molecules (Figure 2.9a–c). By contrast, the CH-PTCDI nanobelts still have considerable fluorescence emission (Figure 2.9d–f). The fluorescence quenching within MP-PTCDI nanoribbons is likely caused by

the intermolecular electron transfer between 1-methylpiperidine on one molecule and the PTCDI part on the other molecule. To prove this intermolecular charge transfer, fluorescence spectra of the reference PTCDI, CH-PTCDI, were measured in chloroform solutions with and without addition of 1-methylpiperidine (Figure 2.10a). Significant fluorescence quenching (indicative of charge transfer interaction) was observed with increasing the concentration of 1-methylpiperidine, which follows the linear Stern-Volmer relationship (Figure 2.10b). The linear fitting gives the binding constant of 21.6 M^{-1} between 1-methylpiperidine and the PTCDI. The binding constant obtained is about one order of magnitude higher than those measured for the aromatic hydrocarbon donor-acceptor complexes reported by others.[42] The enhanced binding is largely due to the stronger electron donating capability of organic amines, compared to the aromatic hydrocarbons.

To determine whether other amines can interact with PTCDI as strong as 1-methylpiperidine, aniline, hexylamine, and triethylamine were selected for comparative testing. Following the same experimental procedure of surface doping as described above, different amount of amines were drop-cast onto the surface of the CH-PTCDI nanobelts. As shown in Figure 2.11a, when 0.5 μmol of amine was applied, no obvious current enhancement was obtained by coating with aniline, hexylamine, and triethylamine, whereas a 26-fold increase in current was observed by coating with 1-methylpiperidine under the same condition. However, significant increase in current was observed when the amount of hexylamine and triethylamine increased to 8 μmol, for which the enhancement ratios were about 3000 and 1800, respectively (though still three orders of magnitude lower than 1-methylpiperidine), whereas aniline still produced

negligible current even with as much as 12 μmol coated (Figure 2.11b).

Regarding the fact that the CH-PTCDI nanobelts coated by the three amines under study (1-methylpiperidine, hexylamine, and triethylamine) produced enhanced conductivity relative to the pristine CH-PTCDI nanobelts while those treated with aniline did not, we further studied the interaction between CH-PTCDI molecules and amines using UV-vis absorption spectroscopy. Inspired by our previous work,[16] in which a strong electron donor (e.g., hydrazine) reduced PTCDI molecules to anionic radicals, we also detected the PTCDI anionic radical upon adding the three amines into the oxygen free solution of CH-PTCDI in dimethyl sulfoxide (DMSO). The existence of three new absorption peaks at 708, 798, and 959 nm in the presence of 1-methylpiperidine indicates the formation of PTCDI anionic radicals (Figure 2.12).[16,17,43] In the absence of oxygen, the radicals are very stable. Upon exposure to air, the three characteristic peaks diminish with time, which further confirms the formation of oxygen-sensitive PTCDI anionic radicals. Moreover, analysis based on the redox potentials suggests that the electron transfer from 1-methylpiperidine to PTCDI is a thermodynamic favorable (spontaneous) process. The Gibbs free energy change (ΔG) of the electron transfer can be calculated from the redox potentials of species under certain concentrations; ΔG thus obtained will indicate if the electron transfer is a thermodynamic favorable (spontaneous) process.

The oxidation potential of 1-methylpiperidine (MP) is 1.08 V vs SCE,[44] and the reduction potential of PTCDI is –0.658 V vs SCE[45] (Note: the electronic property (redox potential) of PTCDI does not change significantly with the different side groups since the two imide positions are node in the π-conjugation). The starting concentration of PTCDI and MP used in Figure 2.12 were 10 μmol L^{-1} and 0.1 mol L^{-1}, respectively. When the

redox reaction reached its equilibrium as shown in Figure 2.12, the concentration of PTCDI anionic radical can be estimated to be about 1×10^{-7} mol/L, according to Beer-Lambert law (given the molar absorption coefficient of PTCDI anionic radical is ϵ = 36000 $M^{-1}.cm^{-1}$ at 956 nm,[13] peak absorbance = 0.0039 at that wavelength, $l_{\text{optical length}}$ = 1 cm). The concentration of the counterpart MP^+ should be the same as that of PTCDI anionic radical, 1×10^{-7} mol L^{-1}. So, from the Nernst equation (Equation 2.1), the electrical potential (ΔE) of the redox (electron transfer) reaction between MP and PTCDI can be calculated to be 0.042 V, which gives a negative ΔG (Equation 2.2), meaning a spontaneous process for the electron transfer in the solution phase. This is consistent with our observation as shown in Figure 2.12

$$\Delta E = \Delta E^0 - \frac{RT}{zF} ln \frac{[PTCDI^-][MP^+]}{[PTCDI][MP]} \; T = 293\; K \qquad 2.1$$

$$\Delta G = -nEF \qquad 2.2$$

In addition to 1-methylpiperidine, PTCDI anionic radicals were also generated by addition of hexylamine and triethylamine (Figure 2.13). However, no such anionic radicals were generated upon addition of aniline to the same deoxygenated solution of CH-PTCDI (Figure 2.13). This comparative observation is consistent with the above discussed results of conductivity enhancement upon casting of different amines, indicating that the effective charge transfer interaction (and thus generating PTCDI anionic radical) is the primary cause of the conductivity enhancement. The electrons thus generated can delocalize (migrate) along the $\pi-\pi$ stacking of PTCDIs,[20,34,46] acting as the

major charge carrier for the n-type material.

The electron donating strength of amines can be evaluated by the oxidation potentials as others did for evaluating the charge transfer in different donor-acceptor pairs.[42] Among all the amines used in this project, aniline would be the strongest electron donor from their oxidation potentials (1-methylpiperidine, E^{o}_{ox} = 1.08 V vs SCE;[44] hexylamine, E^{o}_{ox} = 1.44 V vs SCE;[47] triethylamine, E^{o}_{ox} = 0.99 V vs SCE;[48] aniline, E^{o}_{ox} = 0.86 V vs SCE[48]). However, as evidenced by our results, no charge transfer was observed between aniline and PTCDI even in the presence of a large excess of aniline (i.e., no significant current enhancement was observed with 12 μmol aniline coated on the CH-PTCDI nanobelts, and no absorption peaks of PTCDI anionic radical were detected in the deoxygenated DMSO solution of CH-PTCDI (10 μmol L^{-1}) in the presence of excessive aniline (0.1 mol L^{-1})). The lack of charge transfer between aniline and PTCDI might be due to the weak nucleophilicity of aniline,[49] which prevents the strong donor-acceptor interaction.

On the basis of the aforementioned results and discussion, we propose a possible n-type doping mechanism, which is a result of the generation of PTCDI anionic radicals, to explain the high conductivity of the MP-PTCDI nanoribbons. As demonstrated in Figure 2.14, upon self-assembly into nanoribbons, the side-groups of 1-methylpiperidine are in close proximity of the PTCDI backbones, enabling charge transfer interaction to form PTCDI anionic radicals (the reduction of PTCDI by 1-methylpiperidine should be more thermodynamically favored in solid state compared to solution phase due to the much higher local concentration in solid). Owing to the efficient intramolecular π-electron delocalization within the PTCDI plane, the electron (anionic radical) generated can be

well stabilized (against charge recombination) as observed in the UV-vis absorption spectral measurement (Figure 2.12). When this occurs inside the nanoribbons, the electron can effectively survive from the scavenging by oxygen, making the high conductivity gained sustainable even in the ambient environment as indeed observed in this study (Figure 2.5 and Figure 2.6). With an applied bias, the self-doped electrons rapidly migrate along the long axis of the nanoribbon facilitated by the intermolecular π–π electron delocalization,[16,46,50] leading to the high conductivity. The resultant PTCDI anionic radical is an n-type dopant and is similar to the ones employed in other works,[13-15] in which the substitutional dopant was a zwitterionic molecule, a PTCDI anionic radical linked to an amine centered cation (a reduced analogue of the PTCDI host molecule). An n-doped PTCDI film was fabricated by spin-coating mixed PTCDI dopant and host materials solution, resulting in ten orders of magnitude of increase in conductivity with just 1% doping. The doping process reported in this work is also similar to the self-doped conductor of tetrathiafulvalene (TTF) derivative.[51] TTFCOOH is an insulator, but upon reaction with NH_3, it switches into a conductor $TTFCOO^{-}NH_4^{+}$ with a conductivity of 2×10^{-4} S cm^{-1}. It was demonstrated that the conductivity gained in the salt came from a radical species $TTF^{\bullet+}COO^{-}NH_4^{+}$ generated by self-protonation of the TTF moiety.

2.4.3 Chemiresistive Sensing for Hydrogen Peroxide Vapor Detection

With the increased electrical conductivity by self-doping, MP-PTCDI nanoribbons can be a potential building material for chemiresistive sensors, for which the high conductivity improves the signal-to-noise ratio and simplifies the system design. A

chemiresistive sensor based on the nanoribbons benefits from the large surface area and continuous porosity formed by the interlaced nanoribbons deposited on the substrate. Combination of these two features enhances the adsorption and diffusion (accumulation) of gas analytes, thus increasing the sensitivity to the analytes. The n-type character of the PTCDI material allows for chemiresistive sensing of electron deficient analytes, which can be bound to the surface, causing charge depletion of the material. In this study we chosen H_2O_2 vapor as the target analyte because it is a critical signature for the peroxide explosives including both the synthetic ones (e.g., TATP, DADP and HMTD) and the simple liquid mixtures of H_2O_2 and the fuels.[22]

Figure 2.15 shows the real-time electrical current profile of a MP-PTCDI nanoribbon chemiresistor sensor in response to H_2O_2 vapor. Upon exposure to H_2O_2 vapor (18.5 ppm), there is an instantaneous decrease in current of about 50% (Figure 2.16 demonstrates how to calculate the current decrease of MP-PTCDI nanoribbons in response to H_2O_2 vapor). A very short response time of 19.5 s is attributed to the large surface area of nanoribbons and expedient diffusion of H_2O_2 vapor. The response is concentration dependent. Figure 2.15b shows a plot of relative sensor response as a function of the concentration of H_2O_2 vapor, which can be fit well into the Langmuir absorption model (Equation 2.3).[5]

$$\frac{I_0 - I}{I_0} = \frac{c \cdot k \cdot [H_2O_2]}{1 + k \cdot [H_2O_2]} \qquad 2.3$$

where c is a proportional constant; k is a static equilibrium constant; $[H_2O_2]$ is the vapor concentration of H_2O_2. Fitting the date in Figure 2.15b gives c = 67.42, k = 0.15, with a

$R^2 = 0.9512$. The lowest concentration of H_2O_2 vapor that was tested in this study was 0.6 ppm, which represents the lowest level that can be provided by the present experimental setup.[52] This level of H_2O_2 vapor represents two orders of magnitude dilution of the saturated vapor of commercial 50 wt% H_2O_2 solution. The irreversible sensor response towards H_2O_2 is attributed to the strong surface binding of H_2O_2 and the permanent oxidation of 1-methylpiperidine groups by H_2O_2 ($E^o_{red} = 1.78$ V, vs SCE).[53]

In addition to the high sensitivity, the MP-PTCDI nanoribbons also demonstrated high selectivity towards H_2O_2 vapor against water and the common organic liquids, facilitating the development into practical sensing applications. Such general selectivity was investigated by measuring the sensor response toward the vapor of various common liquids, including water, acetone, ethyl acetate, dichloromethane, methanol, ethanol, toluene, and hexane. In contrast to the irreversible decrease response caused by H_2O_2 vapor, exposure to these liquids vapor resulted in reversible increase in current for the MP-PTCDI nanoribbons (Figure 2.17). The increased conductivity observed is likely a result of dipole interaction between MP-PTCDI nanoribbon and the liquid molecule.[54,55] Table 2.2 lists the dipole moments of all the liquid analytes tested[56] and the corresponding sensor responses measured at 5% of the saturated vapor concentration. Clearly, the sensing response and the dipole moment of the liquids are tightly correlated. For liquids with smaller dipole moments, the response is lower. For example, the vapor concentration of hexane used (8400 ppm) is much higher than many other analytes, such as ethyl acetate (4900 ppm), water (1100 ppm), ethanol (3000 ppm), toluene (1500 ppm), but the relative response is only 0.1%, the lowest among all chemicals studied here, because the dipole moment of hexane is less than 0.1 Debye, much lower than others.

2.5 Conclusions

In conclusion, the nanoribbons assembled from the 1-methylpiperidine substituted-PTCDI molecules possess extraordinarily high conductivity relative to other PTCDI-based nanostructures. The 1-methylpiperidine group plays a key role in the conductivity enhancement, as evidenced by systematic experiments and analysis of the interaction between a model PTCDI nanobelt and 1-methylpiperidine. Upon self-assembly into one-dimensional nanoribbons, the 1-methylpiperidine groups interact with the PTCDI core in stacking proximity to produce the PTCDI anionic radical, which acts as the n-type dopant in the PTCDI lattice. The doping process increases the charge carrier density within the PTCDI nanoribbons, and the one-dimensional π–π stacking of PTCDIs is efficient for long range charge migration, thereby resulting in high conductivity. The high conductivity obtained enables application in chemiresistive sensors. The PTCDI nanoribbons demonstrated highly sensitive response to H_2O_2 vapor through oxidation, rather than dipole moment interaction as in the case of common liquid vapor, thereby producing general selectivity toward H_2O_2 vapor. Owing to the high conductivity of MP-PTCDI nanoribbons, as well as the porous mesh-like morphology of the nanoribbon film, the lowest detected concentration of H_2O_2 vapor in this study was down to 0.6 ppm. This work provides an alternative approach to fabricating self-doped organic semiconductors with high conductivity by molecular engineering.

2.6 References

(1) Allard, S.; Forster, M.; Souharce, B.; Thiem, H.; Scherf, U. Organic Semiconductors for Solution-Processable Field-Effect Transistors (OFETs). *Angew. Chem., Int. Ed.* **2008**, *47*, 4070-4098.

(2) Gross, M.; Muller, D. C.; Nothofer, H.-G.; Scherf, U.; Neher, D.; Brauchle, C.; Meerholz, K. Improving the Performance of Doped π-Conjugated Polymers for Use in Organic Light-Emitting Diodes. *Nature* **2000**, *405*, 661-665.

(3) Hains, A. W.; Liang, Z.; Woodhouse, M. A.; Gregg, B. A. Molecular Semiconductors in Organic Photovoltaic Cells. *Chem. Rev.* **2010**, *110*, 6689-6735.

(4) Baeg, K.-J.; Binda, M.; Natali, D.; Caironi, M.; Noh, Y.-Y. Organic Light Detectors: Photodiodes and Phototransistors. *Adv. Mater.* **2013**, *25*, 4267-4295.

(5) Huang, H.; Gross, D. E.; Yang, X.; Moore, J. S.; Zang, L. One-Step Surface Doping of Organic Nanofibers to Achieve High Dark Conductivity and Chemiresistor Sensing of Amines. *ACS Appl. Mater. Interfaces* **2013**, *5*, 7704-7708.

(6) Medina-Sánchez, M.; Martínez-Domingo, C.; Ramon, E.; Merkoçi, A. An Inkjet-Printed Field-Effect Transistor for Label-Free Biosensing. *Adv. Funct. Mater.* **2014**, *24*, 6291-6302.

(7) Chan, C. K.; Kim, E. G.; Brédas, J. L.; Kahn, A. Molecular n-Type Doping of 1,4,5,8-Naphthalene Tetracarboxylic Dianhydride by Pyronin B Studied Using Direct and Inverse Photoelectron Spectroscopies. *Adv. Funct. Mater.* **2006**, *16*, 831-837.

(8) Walzer, K.; Maennig, B.; Pfeiffer, M.; Leo, K. Highly Efficient Organic Devices Based on Electrically Doped Transport Layers. *Chem. Rev.* **2007**, *107*, 1233-1271.

(9) Lu, C.-K.; Meng, H.-F. Hole Doping by Molecular Oxygen in Organic Semiconductors: Band-Structure Calculations. *Phys. Rev. B: Condens. Matter Mater. Phys.* **2007**, *75*, 235206.

(10) Yamamoto, Y.; Yoshino, K.; Inuishi, Y. Electrical Properties of Phthalocyanine-Halogen Complexes. *J. Phys. Soc. Jpn.* **1979**, *47*, 1887-1891.

(11) Maennig, B.; Pfeiffer, M.; Nollau, A.; Zhou, X.; Leo, K.; Simon, P. Controlled p-Type Doping of Polycrystalline and Amorphous Organic Layers: Self-Consistent Description of Conductivity and Field-Effect Mobility by a Microscopic Percolation Model. *Phys. Rev. B: Condens. Matter Mater. Phys.* **2001**, *64*, 195208.

(12) Werner, A. G.; Li, F.; Harada, K.; Pfeiffer, M.; Fritz, T.; Leo, K. Pyronin B as a Donor for n-Type Doping of Organic Thin Films. *Appl. Phys. Lett.* **2003**, *82*, 4495-4497.

(13) Gregg, B. A.; Cormier, R. A. Doping Molecular Semiconductors: n-Type Doping of a Liquid Crystal Perylene Diimide. *J. Am. Chem. Soc.* **2001**, *123*, 7959-7960.

(14) Chen, S.-G.; Branz, H. M.; Eaton, S. S.; Taylor, P. C.; Cormier, R. A.; Gregg, B. A. Substitutional n-Type Doping of an Organic Semiconductor Investigated by Electron Paramagnetic Resonance Spectroscopy. *J. Phys. Chem. B* **2004**, *108*, 17329-17336.

(15) Gregg, B. A.; Chen, S.-G.; Cormier, R. A. Coulomb Forces and Doping in Organic

Semiconductors. *Chem. Mater.* **2004**, *16*, 4586-4599.

(16) Che, Y.; Datar, A.; Yang, X.; Naddo, T.; Zhao, J.; Zang, L. Enhancing One-Dimensional Charge Transport through Intermolecular π-Electron Delocalization: Conductivity Improvement for Organic Nanobelts. *J. Am. Chem. Soc.* **2007**, *129*, 6354-6355.

(17) Arulkashmir, A.; Jain, B.; John, J. C.; Roy, K.; Krishnamoorthy, K. Chemically Doped Perylene Diimide Lamellae Based Field Effect Transistor With Low Operating Voltage and High Charge Carrier Mobility. *Chem. Commun.* **2014**, *50*, 326-328.

(18) Malinauskas, A. Self-Doped Polyanilines. *J. Power Sources* **2004**, *126*, 214-220.

(19) Yue, J.; Epstein, A. J. Synthesis of Self-Doped Conducting Polyaniline. *J. Am. Chem. Soc.* **1990**, *112*, 2800-2801.

(20) Zang, L.; Che, Y.; Moore, J. S. One-Dimensional Self-Assembly of Planar π-Conjugated Molecules: Adaptable Building Blocks for Organic Nanodevices. *Acc. Chem. Res.* **2008**, *41*, 1596-1608.

(21) Che, Y.; Yang, X.; Liu, G.; Yu, C.; Ji, H.; Zuo, J.; Zhao, J.; Zang, L. Ultrathin n-Type Organic Nanoribbons With High Photoconductivity and Application in Optoelectronic Vapor Sensing of Explosives. *J. Am. Chem. Soc.* **2010**, *132*, 5743-5750.

(22) Xu, M.; Han, J.-M.; Wang, C.; Yang, X.; Pei, J.; Zang, L. Fluorescence Ratiometric Sensor for Trace Vapor Detection of Hydrogen Peroxide. *ACS Appl. Mater. Interfaces* **2014**, *6*, 8708-8714.

(23) Xu, M.; Han, J.-M.; Zhang, Y.; Yang, X.; Zang, L. A Selective Fluorescence Turn-On Sensor for Trace Vapor Detection of Hydrogen Peroxide. *Chem. Commun.* **2013**, *49*, 11779-11781.

(24) Abo, M.; Urano, Y.; Hanaoka, K.; Terai, T.; Komatsu, T.; Nagano, T. Development of a Highly Sensitive Fluorescence Probe for Hydrogen Peroxide. *J. Am. Chem. Soc.* **2011**, *133*, 10629-10637.

(25) Xu, M.; Bunes, B. R.; Zang, L. Paper-Based Vapor Detection of Hydrogen Peroxide: Colorimetric Sensing With Tunable Interface. *ACS Appl. Mater. Interfaces* **2011**, *3*, 642-647.

(26) Bai, J.; Jiang, X. A Facile One-Pot Synthesis of Copper Sulfide-Decorated Reduced Graphene Oxide Composites for Enhanced Detecting of H_2O_2 in Biological Environments. *Anal. Chem.* **2013**, *85*, 8095-8101.

(27) Guo, P.; Zhao, G.; Chen, P.; Lei, B.; Jiang, L.; Zhang, H.; Hu, W.; Liu, M. Porphyrin Nanoassemblies via Surfactant-Assisted Assembly and Single Nanofiber Nanoelectronic Sensors for High-Performance H_2O_2 Vapor Sensing. *ACS Nano* **2014**, *8*, 3402-3411.

(28) Bohrer, F. I.; Colesniuc, C. N.; Park, J.; Schuller, I. K.; Kummel, A. C.; Trogler, W. C. Selective Detection of Vapor Phase Hydrogen Peroxide With Phthalocyanine Chemiresistors. *J. Am. Chem. Soc.* **2008**, *130*, 3712-3713.

(29) Che, Y.; Yang, X.; Balakrishnan, K.; Zuo, J.; Zang, L. Highly Polarized and Self-Waveguided Emission From Single-Crystalline Organic Nanobelts. *Chem. Mater.* **2009**, *21*, 2930-2934.

(30) Manatt, S. L.; Manatt, M. R. R. On the Analyses of Mixture Vapor Pressure Data: The Hydrogen Peroxide/Water System and Its Excess Thermodynamic Functions. *Chem.-Eur. J.* **2006**, *12*, 3695-3695.

(31) Wang, D.; Chen, A.; Jang, S.-H.; Davies, J.; Jen, A. K. Y. The Effect of Dipole Moment and Electron Deficiency of Analytes on the Chemiresistive Response of TiO_2(B) Nanowires. *Analyst* **2011**, *136*, 4179-4182.

(32) Wurthner, F. Perylene Bisimide Dyes as Versatile Building Blocks for Functional Supramolecular Architectures. *Chem. Commun.* **2004**, 1564-1579.

(33) Görl, D.; Zhang, X.; Würthner, F. Molecular Assemblies of Perylene Bisimide Dyes in Water. *Angew. Chem., Int. Ed.* **2012**, *51*, 6328-6348.

(34) Zang, L. Interfacial Donor–Acceptor Engineering of Nanofiber Materials to Achieve Photoconductivity and Applications. *Acc. Chem. Res.* **2015**, *48*, 2705-2714.

(35) Chen, S.; Slattum, P.; Wang, C.; Zang, L. Self-Assembly of Perylene Imide Molecules into 1D Nanostructures: Methods, Morphologies, and Applications. *Chem. Rev.* **2015**, 115, 11967-11998.

(36) Kazmaier, P. M.; Hoffmann, R. A Theoretical Study of Crystallochromy. Quantum Interference Effects in the Spectra of Perylene Pigments. *J. Am. Chem. Soc.* **1994**, *116*, 9684-9691.

(37) Lei, T.; Luo, J.; Wang, L.; Ma, Y.; Wang, J.; Cao, Y.; Pei, J. Highly Stable Blue Light-Emitting Materials With a Three-Dimensional Architecture: Improvement of Charge Injection and Electroluminescence Performance. *New J. Chem.* **2010**, *34*, 699-707.

(38) Che, Y.; Huang, H.; Xu, M.; Zhang, C.; Bunes, B. R.; Yang, X.; Zang, L. Interfacial Engineering of Organic Nanofibril Heterojunctions into Highly Photoconductive Materials. *J. Am. Chem. Soc.* **2011**, *133*, 1087-1091.

(39) Huang, H.; Chou, C.-E.; Che, Y.; Li, L.; Wang, C.; Yang, X.; Peng, Z.; Zang, L. Morphology Control of Nanofibril Donor–Acceptor Heterojunction to Achieve High Photoconductivity: Exploration of New Molecular Design Rule. *J. Am. Chem. Soc.* **2013**, *135*, 16490-16496.

(40) Cazaux, J. About the Mechanisms of Charging in EPMA, SEM, and ESEM With

Their Time Evolution. *Microsc. Microanal.* **2004**, *10*, 670-684.

(41) Moncrieff, D. A.; Robinson, V. N. E.; Harris, L. B. Charge Neutralisation of Insulating Surfaces in the SEM by Gas Ionisation. *J. Phys. D: Appl. Phys.* **1978**, *11*, 2315.

(42) Rathore, R.; Lindeman, S. V.; Kochi, J. K. Charge-Transfer Probes for Molecular Recognition via Steric Hindrance in Donor-Acceptor Pairs. *J. Am. Chem. Soc.* **1997**, *119*, 9393-9404.

(43) Ghosh, I.; Ghosh, T.; Bardagi, J. I.; König, B. Reduction of Aryl Halides by Consecutive Visible Light-Induced Electron Transfer Processes. *Science* **2014**, *346*, 725-728.

(44) Jakubiak, J.; Allonas, X.; Fouassier, J. P.; Sionkowska, A.; Andrzejewska, E.; Linden, L. Å.; Rabek, J. F. Camphorquinone-Amines Photoinitating Systems for the Initiation of Free Radical Polymerization. *Polymer* **2003**, *44*, 5219-5226.

(45) Kim, J. Y.; Bard, A. J. Organic Donor/Acceptor Heterojunction Photovoltaic Devices Based on Zinc Phthalocyanine and a Liquid Crystalline Perylene Diimide. *Chem. Phys. Lett.* **2004**, *383*, 11-15.

(46) Coropceanu, V.; Cornil, J.; da Silva Filho, D. A.; Olivier, Y.; Silbey, R.; Brédas, J.-L. Charge Transport in Organic Semiconductors. *Chem. Rev.* **2007**, *107*, 926-952.

(47) Barnes, K. K.; Mann, C. K. Electrochemical Oxidation of Primary Aliphatic Amines. *J. Org. Chem.* **1967**, *32*, 1474-1479.

(48) Reppy, M. A.; Cooper, M. E.; Smithers, J. L.; Gin, D. L. A Novel Fluorescent Monomer for the Selective Detection of Phenols and Anilines. *J. Org. Chem.* **1999**, *64*, 4191-4195.

(49) Bunnett, J. F.; Davis, G. T. The Nucleophilic Reactivity of Aniline, Hydrazine and Phenoxide Ion Toward 2,4-Dinitrochlorobenzene1. *J. Am. Chem. Soc.* **1958**, *80*, 4337-4339.

(50) Supur, M.; Fukuzumi, S. Energy and Electron Transfer of One-Dimensional Nanomaterials of Perylenediimides. *ECS J. Solid State Sci. Technol.* **2013**, *2*, M3051-M3062.

(51) Kobayashi, Y.; Yoshioka, M.; Saigo, K.; Hashizume, D.; Ogura, T. Hydrogen-Bonding-Assisted Self-Doping in Tetrathiafulvalene (TTF) Conductor. *J. Am. Chem. Soc.* **2009**, *131*, 9995-10002.

(52) Li, J.; Lu, Y.; Ye, Q.; Cinke, M.; Han, J.; Meyyappan, M. Carbon Nanotube Sensors for Gas and Organic Vapor Detection. *Nano Lett.* **2003**, *3*, 929-933.

(53) Islam, A.-z. N.; Tofik, N. I.; Murtuza, N. T. Coherent-Synchronized Oxidation of 4-

Ethylpyridine and Piperidine by Hydrogen Peroxide. *J. Chem. Chem. Eng.* **2013**, *7*, 76-80.

(54) Carsten, B.; Szarko, J. M.; Son, H. J.; Wang, W.; Lu, L.; He, F.; Rolczynski, B. S.; Lou, S. J.; Chen, L. X.; Yu, L. Examining the Effect of the Dipole Moment on Charge Separation in Donor–Acceptor Polymers for Organic Photovoltaic Applications. *J. Am. Chem. Soc.* **2011**, *133*, 20468-20475.

(55) Wang, B.; Haick, H. Effect of Functional Groups on the Sensing Properties of Silicon Nanowires toward Volatile Compounds. *ACS Appl. Mater. Interfaces* **2013**, *5*, 2289-2299.

(56) Haynes, W. M. *CRC Handbook of Chemistry and Physics*, 91st ed; CRC Press: Boulder, CO, USA, 2010-2011.

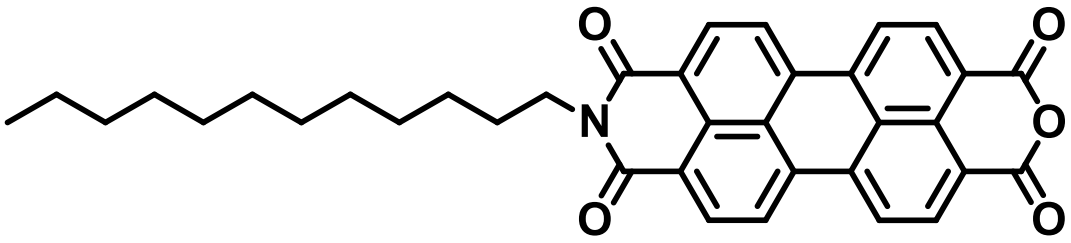

Compound 1

Figure 2.1 Chemical structure of Compound 1.

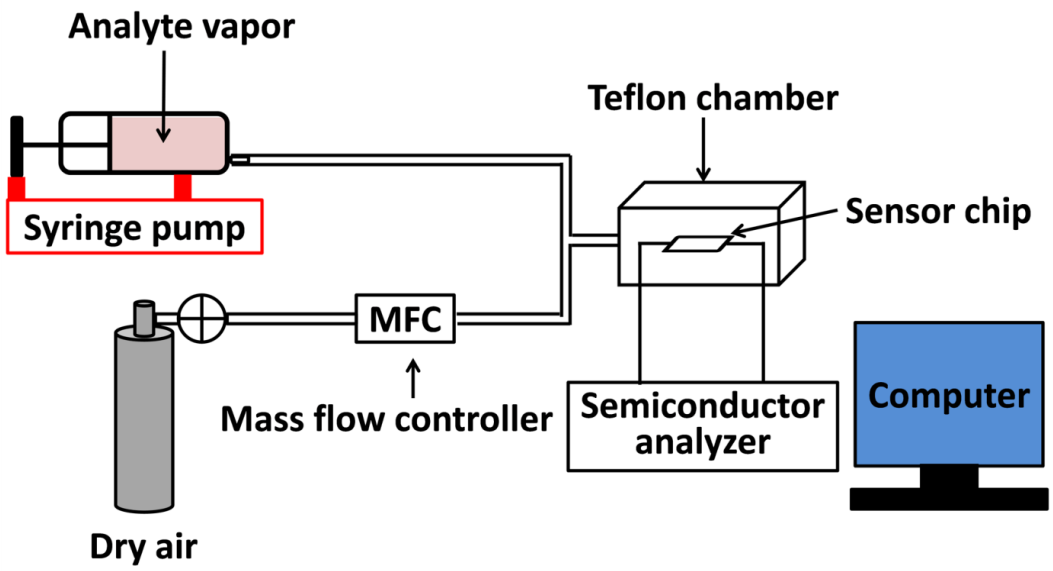

Figure 2.2 Schematic diagram of the vapor sensing measurement system.

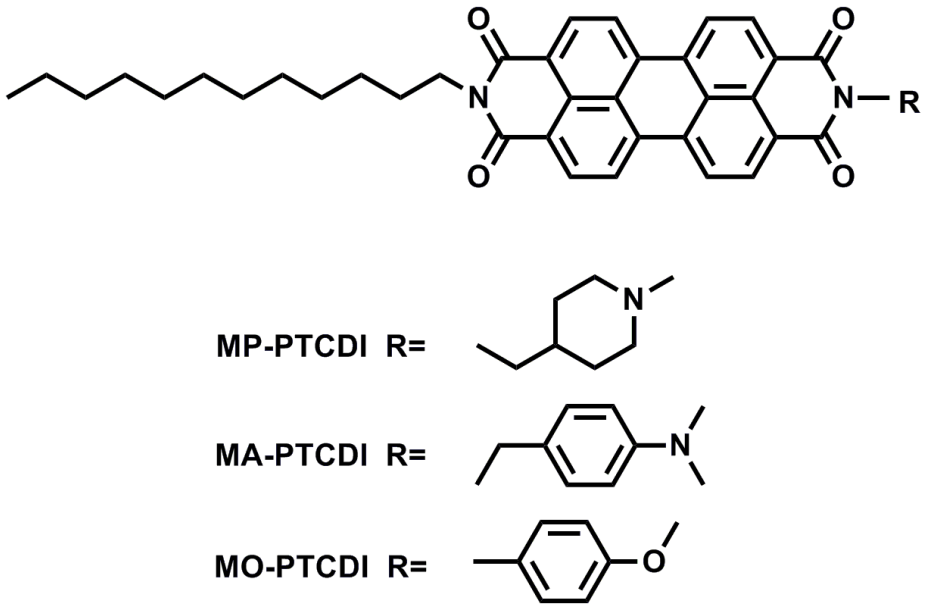

Figure 2.3 Molecular structures of MP-PTCDI and two other PTCDI analogues, MA-PTCDI and MO-PTCDI employed for comparative study.

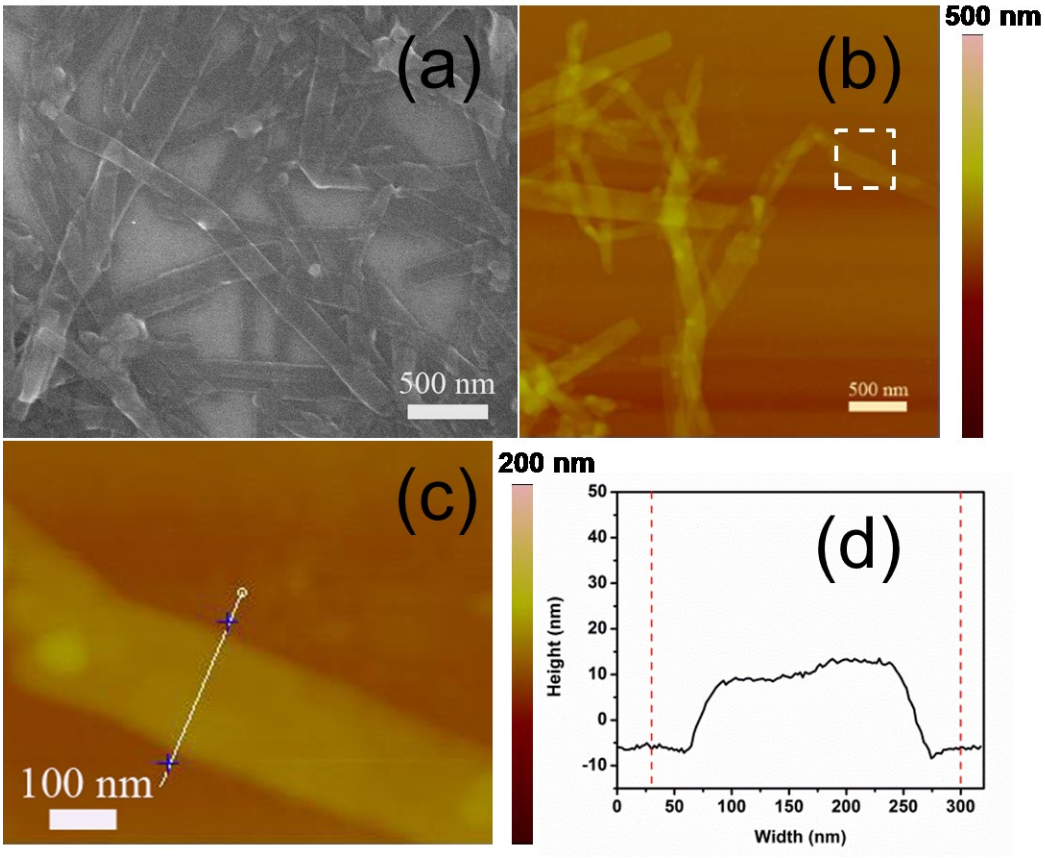

Figure 2.4 Morphology of MP-PTCDI nanoribbons: (a) SEM image; (b) AFM image; (c) enlarged AFM image of the MP-PTCDI nanoribbon in the selected area in panel b; (d) the height-profile corresponding to the white line in panel c.

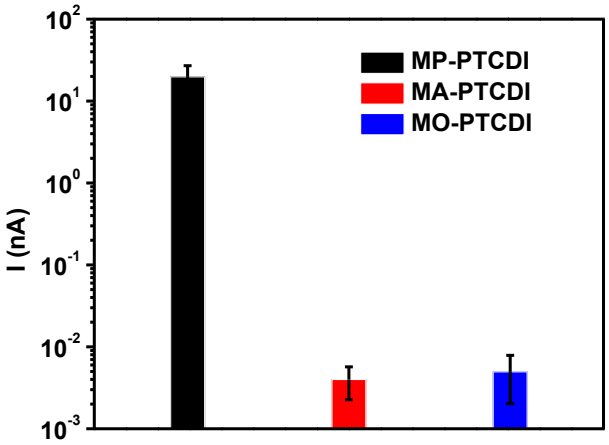

Figure 2.5 Comparison of the electrical current measured over three PTCDI nanoribbons deposited in the same molar amount (12 nmol), following the same experimental process. The current values were measured at a bias of 10 V. The error bars represent the standard deviation based on the current measured by three independent devices of each PTCDI nanoribbon.

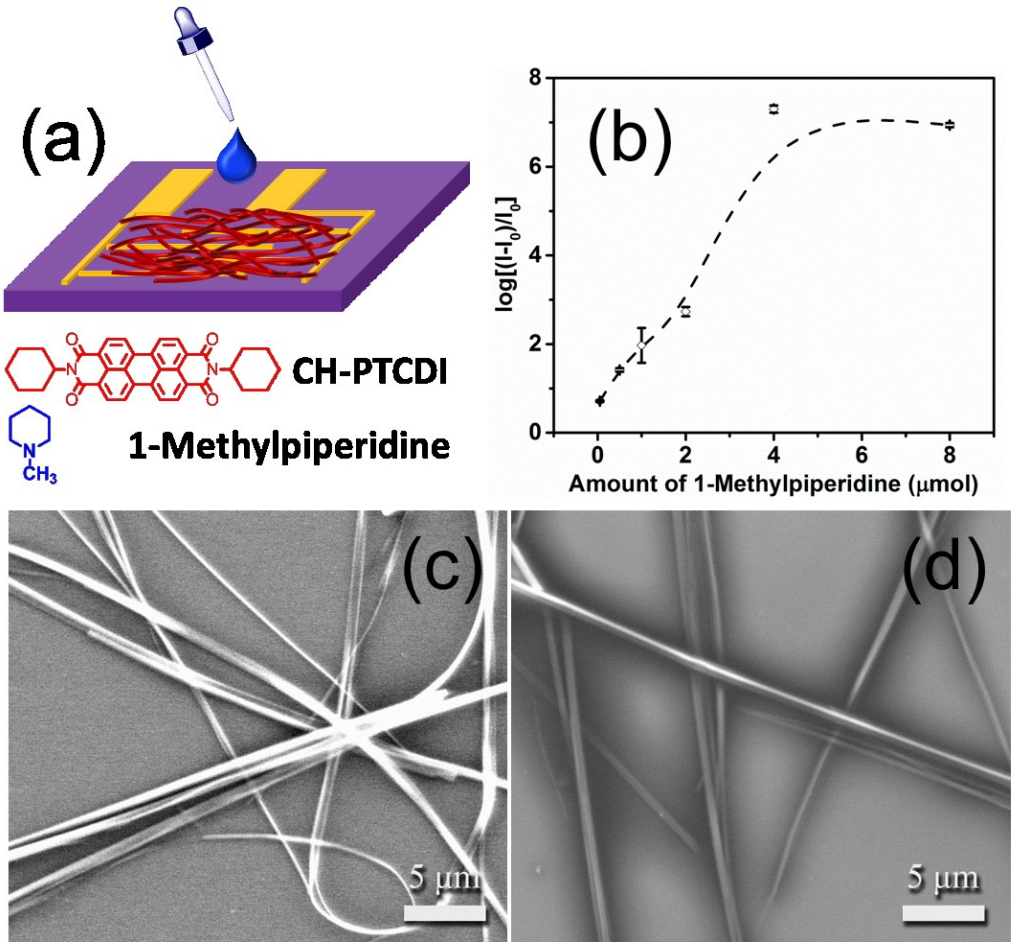

Figure 2.6 Increased current in CH-PTCDI nanobelts after surface coating with 1-methylpiperidine: (a) Schematic of the CH-PTCDI nanobelts deposited on the IDE and the surface coating by drop-casting the solution of 1-methylpiperidine. (b) The current enhancement ratio, $\log[(I-I_0)/I_0]$, measured over the CH-PTCDI nanobelts when coated with varying molar amounts of 1-methylpiperidine, where I_0 is the current of pristine CH-PTCDI nanobelts, and I is the current measured on the same nanobelts after coated with 1-methylpiperidine. The error bars stand for the standard deviation based on the values measured by three independent devices. All the current values were obtained at a bias of 10 V. (c, d) SEM images of the CH-PTCDI nanobelts before (c) and after (d) surface coating with 1-methylpiperidine.

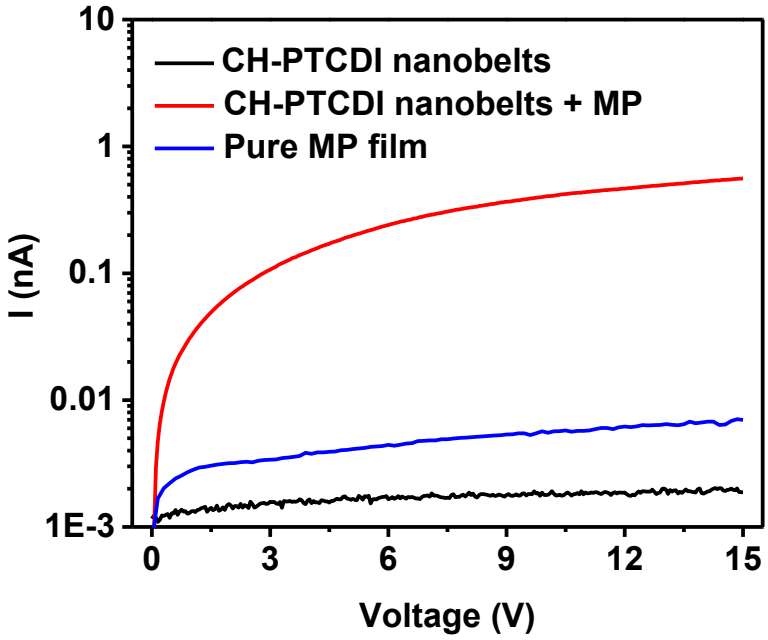

Figure 2.7 I-V curves of the CH-PTCDI nanobelts before (black) and after (red) surface coating with 2 μmol 1-methylpieridine (MP). The pure 1-methylpiperidine thin film drop-cast from 4 μmol amount is little conductive (blue).

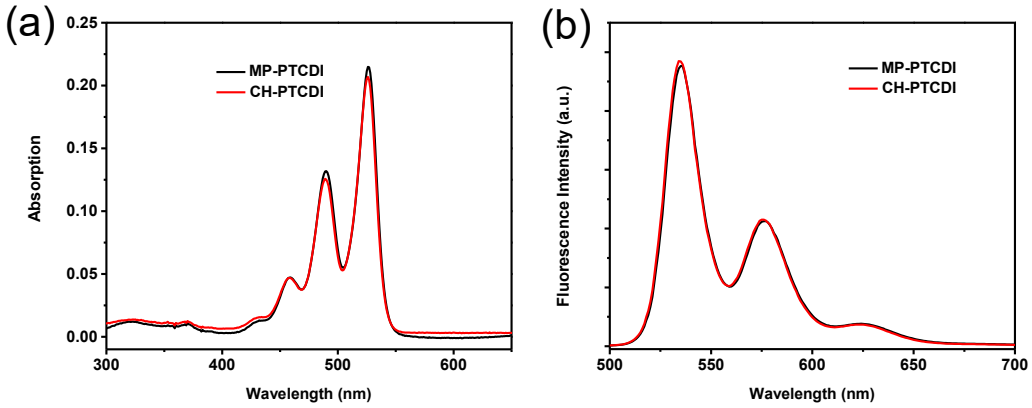

Figure 2.8 UV-vis absorption (a) and fluorescence (b) spectra of the chloroform solution (10 μmol L^{-1}) of MP-PTCDI (black) and CH-PTCDI (red). The excitation wavelength for fluorescence spectra was 490 nm.

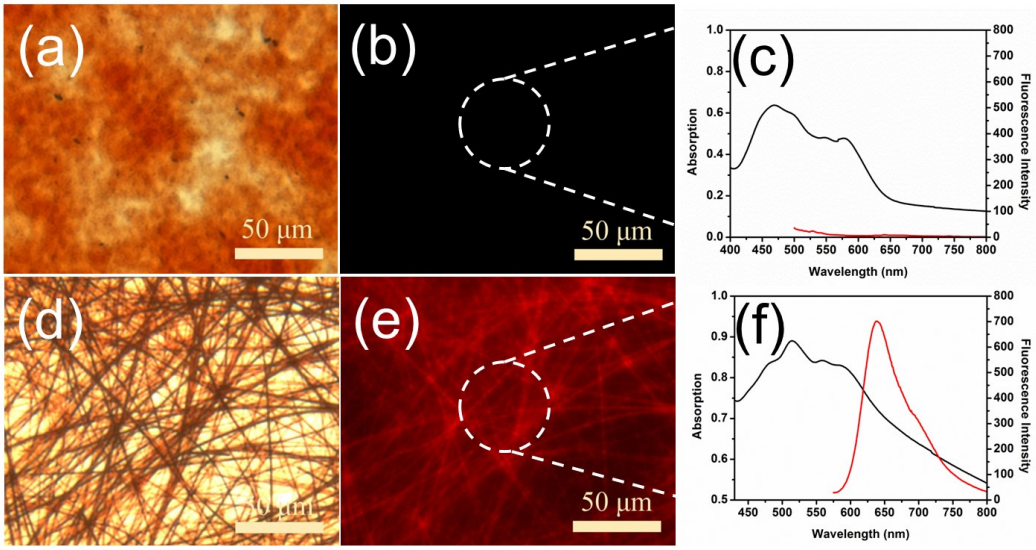

Figure 2.9 Morphologies, UV-vis absorption, and fluorescence emission of PTCDI thin films: (a, b) bright-field and fluorescent optical microscopy images of MP-PTCDI nanoribbons deposited on a quartz slide; (c) UV-vis absorption (black) and fluorescence (red) spectra of MP-PTCDI nanoribbons in the selected area (white cycle); (d, e) bright-field and fluorescent optical microscopy images of CH-PTCDI nanobelts deposited on a quartz slide; (f) UV-vis absorption (black) and fluorescence (red) spectra of CH-PTCDI nanobelts in the selected area (white cycle).

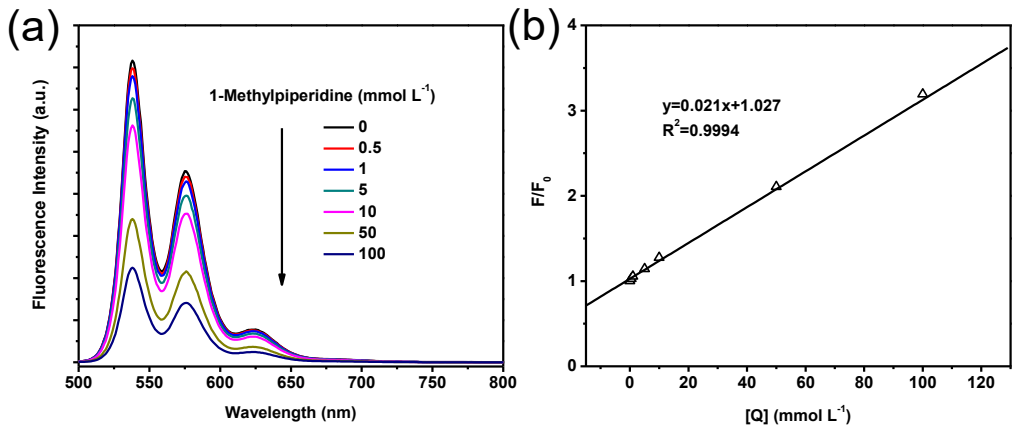

Figure 2.10 Significant fluorescence quenching of CH-PTCDI molecule when interacting with 1-methylpiperidine: (a) Fluorescence spectra of CH-PTCDI solution in chloroform (10 μmol L^{-1}) upon addition of 1-methylpiperidine at varying concentrations. The excitation wavelength was 490 nm. (b) Stern-Volmer plot of the fluorescence quenching shown in panel A.

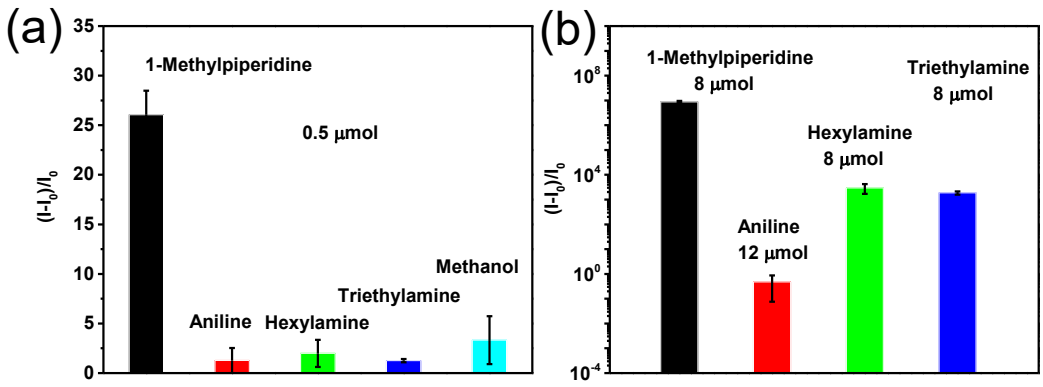

Figure 2.11 Comparative study of current in CH-PTCDI nanobelts after surface doping with various amines: (a) histogram of current enhancement ratio of CH-PTCDI nanobelts upon surface coating of 0.5 μmol different amines (1-methylpiperidine, aniline, hexylamine, triethylamine), methanol, which was used as the solvent for these amines, was also tested as the control; (b) histogram of current enhancement ratio of CH-PTCDI nanobelts upon surface-coating of much larger amount of amines (1-methylpiperidine 8 μmol, aniline 12 μmol, triethylamine 8 μmol, and hexylamine 8 μmol). The error bars represent the standard deviation based on the values measured by three independent devices of each sample. All current values in histogram were gained at a bias voltage of 10 V.

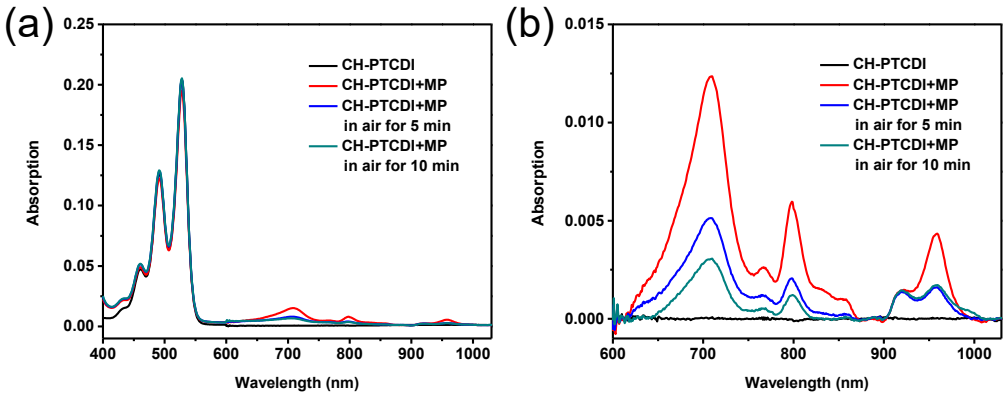

Figure 2.12 Detection of PTCDI anionic radicals: (a) UV-vis absorption spectra of deoxygenated DMSO solution of CH-PTCDI (10 μmol L^{-1}) before (black) and after (red) addition of excessive 1-methylpiperidine (MP, 0.1 mol L^{-1}), and the same solution after exposed to air for 5 min (blue) and 10 min (dark cyan); (b) enlarged UV-vis absorption spectra of panel a in the wavelength range of 600 nm to 1000 nm.

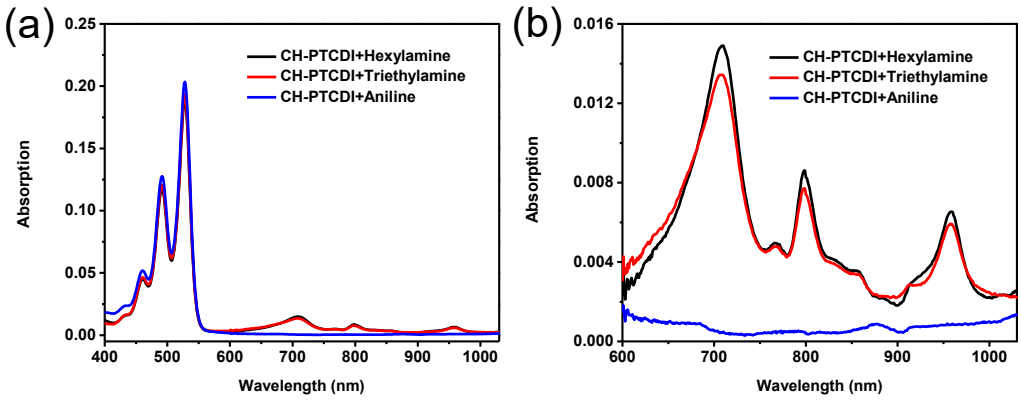

Figure 2.13 Detection of PTCDI anionic radicals: (a) UV-vis absorption spectra of deoxygenated DMSO solution of CH-PTCDI (10 μmol L^{-1}) in the presence of excessive amine (0.1 mol L^{-1}), hexylamine (black), triethylamine (red), aniline (blue); (b) enlarged UV-vis absorption spectra of panel a in the wavelength range of 600 to 1000 nm.

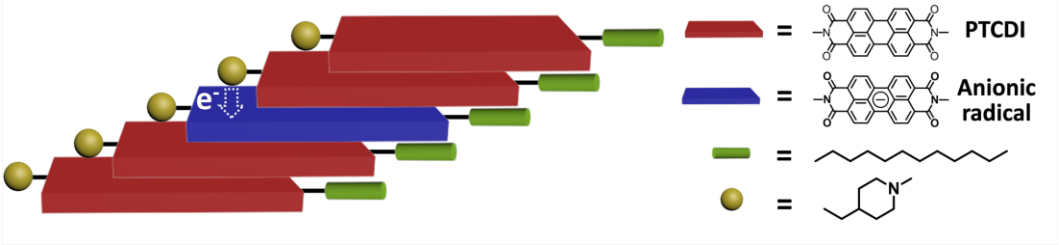

Figure 2.14 Schematic of the conductivity enhancement of MP-PTCDI nanoribbons.

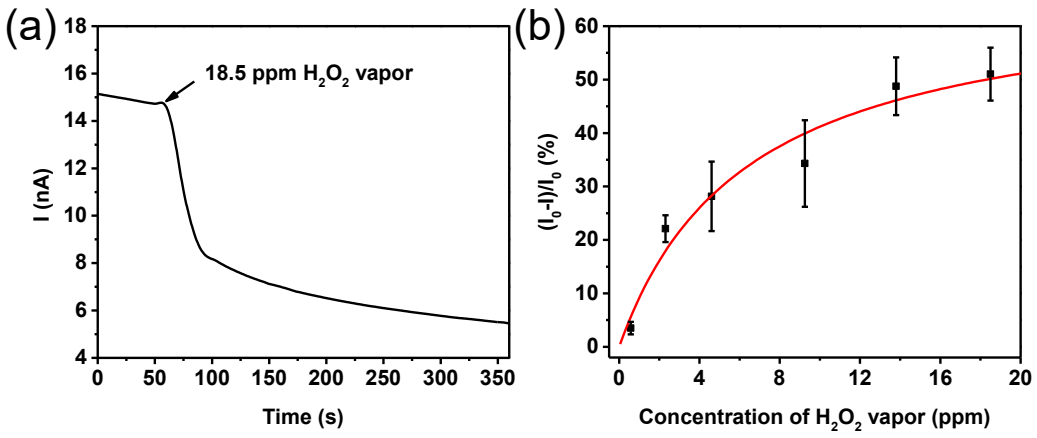

Figure 2.15 Real-time electrical current profile of a MP-PTCDI nanoribbon chemiresistor sensor in response to H_2O_2 vapor: (a) current measured over the MP-PTCDI nanoribbons in response to H_2O_2 vapor (18.5 ppm); (b) relative current change [$(I_0–I)/I_0$ (%)] as a function of the concentration of H_2O_2 vapor, where I and I_0 are the current measured before and after exposure to H_2O_2 vapor, respectively. The error bars represent the standard deviation of the relative current changes measured with three independent sensors.

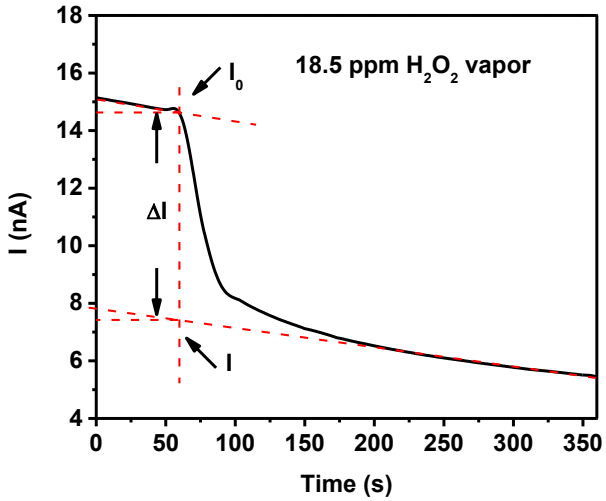

Figure 2.16 A plot demonstrating how to calculate the current decrease of MP-PTCDI nanoribbons in response to H_2O_2 vapor.

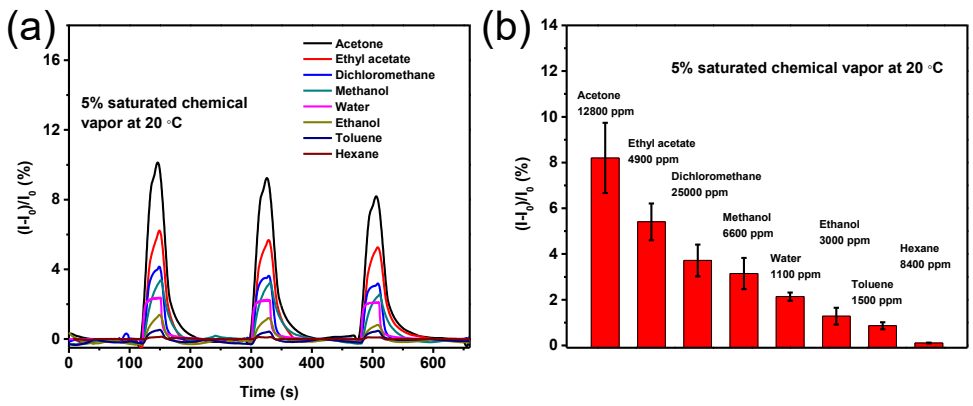

Figure 2.17 The selectivity of a MP-PTCDI nanoribbon chemiresistor sensor: (a) relative current change $((I–I_0)/I_0)$ of MP-PTCDI nanoribbons in three subsequent exposures toward the common organic liquids and water at 5% of the saturated vapor concentration; (b) average values of $(I–I_0)/I_0$ measured over the MP-PTCDI nanoribbons when exposed to the different liquids vapor at 5% saturated vapor concentration. The error bars represent the standard deviation of the relative current changes measured with three independent sensors.

Table 2.1 Comparison of morphology and size of PTCDI-based nanostructures.

Sample	Morphology	Thickness	Width	Length	Reference
MP-PTCDI	Nanoribbon	About 15 nm	100-300 nm	Several micrometers	This work
MA-PTCDI	Nanoribbon	About 5 nm	50-200 nm	Several micrometers	S1
MO-PTCDI	Nanoribbon	-	30-500 nm	-	S1

Table 2.2 The dipole moment of the liquid analytes tested and the corresponding sensor response measured at 5% of the saturated vapor concentration.

Analyte	μ (Debye)	$(I–I_0)/I_0$ (%)
Acetone	2.88	8.19
Ethyl acetate	1.78	5.40
Dichloromethane	1.60	3.71
Methanol	1.70	3.14
Water	1.85	2.13
Ethanol	1.69	1.28
Toluene	0.36	0.86
Hexane	≤ 0.1	0.10

CHAPTER 3

PERSISTENT PHOTOCONDUCTIVITY IN PERYLENE DIIMIDE NANOFIBER MATERIALS[1]

3.1 Abstract

Perylene tetracarboxylic diimide (PTCDI) derivatives have been extensively investigated for one-dimensional (1D) self-assembly and their applications in optoelectronic devices. Our study on self-assembled PTCDI nanofiber materials revealed a persistent photoconductivity (PPC) effect, which is sustained conductivity after illumination is terminated. A comprehensive understanding of the PPC effect in PTCDI nanofibril materials will enable us to explore and enhance their optoelectronic applications. Here, we have investigated the PPC effect in the nanofibers assembled from 1-Methylpiperidine-substituted perylene tetracarboxylic diimide (MP-PTCDI) with respect to the PPC relaxation at different temperatures, illumination power densities, molar amount and morphology of the PTCDI film deposited on the interdigitated electrodes. The photocurrent relaxation was also performed on several other PTCDI nanofiber materials for comparative study. We conclude that the significant PPC effect in

---

[1] Reproduced by permission from Wu, N.; Wang, C.; Slattum, P. M.; Zhang, Y; Yang, X.; Zang, L., Persistent Photoconductivity in Perylene Diimide Nanofiber Materials. *ACS Energy Lett.* **2016**, *1*, 906-912. Copyright (2016) American Chemical Society.

MP-PTCDI nanofibers can be attributed to the electrical potential fluctuations caused by the structure defects, which thus hinder the recombination of charge carriers. This study may provide new design rules for fabrication of molecular semiconductor materials with strong PPC in order to approach high efficiency of photovoltaic and photocatalysis.

3.2 Introduction

Perylene tetracarboxylic diimide (PTCDI) derivatives, forming a typical n-type organic semiconductor, have been receiving much research attention because of their high thermal- and photo-stability.[1,2] Their strong electron affinity and strong absorption in the visible light region make PTCDI a good candidate for next-generation photovoltaic devices[3-6] and photocatalytic materials.[1,7] In addition, self-assembly of PTCDI molecules often gives rise to the formation of well-defined nanofibril structures through the columnar π-π stacking between the perylene planes.[2] The as-prepared PTCDI nanofibers assist in the construction of the distinctive morphology of p-n junction nanostructures in photovoltaic devices to improve their performance,[4,6] for instance, the novel crystalline donor/acceptor (P3HT/PTCDI) shish-kebab structure,[4,8] in which the observed high photovoltage was likely due to this special intermolecular orientation. PTCDI nanofibril materials have the potential to be used in photocatalytic systems as well. Previous research has shown that PTCDI molecules with attached donor moieties were self-assembled into nanofibers, followed by coated with co-catalysts, such as TiO_2 and/or Pt,[1,7] or *g*-C_3N_4 and Pt,[9] showed excellent performance in the photocatalytic splitting of water for H_2 production. The excellent photocatalytic activity of the composite photocatalysts was attributed to PTCDIs' strong visible-light absorption, matched energy

level and effective charge separation with the co-catalysts.[1,7]

In this study, persistent photoconductivity (PPC), which is sustained conductivity after illumination is terminated,[10] was observed by accident in the nanofibers fabricated from a PTCDI molecule with a Donor-Acceptor (D-A) structure (1-Methylpiperidine substituted-PTCDI molecule, MP-PTCDI, shown in Figure 3.1). In general, the PPC effect is not so commonly observed in organic semiconductor materials as in inorganic counterparts. For PTCDI-based materials there have been few reports where the PPC effect was implied.[11,12] We believe that further study of the PPC effect and the dependence on materials structure will offer deep insight into the charge carrier storage and relaxation process within organic semiconductor materials (particularly PTCDIs), thus providing guidance in optimizing the photovoltaic and photocatalytic performance of these materials.

The PPC effect has been mostly observed and investigated in inorganic semiconductor compounds, alloys and heterojunctions.[10,13-17] Generally, the PPC effect is caused by a potential barrier that prohibits the recombination of photogenerated electron-hole pairs. There are multiple models to describe the PPC mechanism in regard to various material systems, such as random localized potential fluctuations (RLPF), large lattice relaxation (LLR) and microscopic barrier (MB).[10] In the RLPF model, carriers are separated by the potential fluctuations, which reduce the rate of recombination, producing PPC. For example, RLPF induced by composition fluctuation was found to be responsible for PPC observed in $Zn_{0.3}Cd_{0.7}Se$ mixed crystals[13] and $CdS_{0.5}Se_{0.5}$ semiconductor alloy.[15] In addition to the intrinsic sources, extrinsic origins of RLPF may also come from the substrate effect as was found in monolayer MoS_2 field effect

transistors.[10] In a LLR model, deep-level traps (DX centers) are considered to be the source of PPC. Under illumination, the DX center can be converted into a metastable shallow donor state, which produces a potential barrier due to the difference in lattice relaxation between the two states. The recapture of electrons by the DX center is prevented by the barrier, leading to the PPC effect.[17,18] The LLR model was supported by a study on n-type $Al_xGa_{1-x}As$, for which the PPC effect was produced by donor-related defects.[18] The MB model is based on the spatial macroscopic potential barrier, which separates the photoexcited electron-hole pairs, and this model explains well the PPC effect in many heterostructures, such as graphene/MoS_2,[16] quantum-dot/graphene,[19] chlorophyll/graphene.[20]

Although the PPC effect, as well as its influence on optoelectronic properties and performance, have been extensively studied on the inorganic semiconductors, there lacks of such detailed study on the organic materials. Especially, most of the PPC studies have been performed at low temperatures (e.g., from 17 K to 300 K).[14] Room temperature study of the PPC within organic materials would fill in the field with new knowledge by understanding better the sustained photoinduced charge separation.[21-23] In this work, an electron donor-acceptor PTCDI, MP-PTCDI (Figure 3.1), was chosen as the organic semiconductor material to study the PPC effect. For comparison, several other PTCDIs were also employed and investigated parallel under the same conditions. Moreover, the PTCDIs form well-defined nanofibers through solution phase self-assembly, and the 1D intermolecular arrangement (dominated by the cofacial π–π stacking) provides efficient charge transport pathway, which further enhances the charge separation and is suited for application in photocatalysis and photovoltaics.[24] As observed in this study, the PPC

decay time of MP-PTCDI nanofibers can be as long as 1058 s. The PPC decay was found to be dependent on the temperature, the irradiation power density, the film morphology and amount of nanofibers deposited on the interdigitated electrodes (IDE). Moreover, the side groups of PTCDI can be modified with electron donating moieties with different donation power (as shown in Figure 3.1), in order to investigate the influence of electron donor-acceptor interaction on the PPC. Donor-acceptor interaction, particularly under photoexcitation, creates charge separation and electrostatic traps, thus producing potential barriers that hinder the recombination of electron-hole pairs. Since the two imide positions within PTCDI are nodes in the π-orbitals, changing the substitutions at the two ends does not change significantly the electronic properties of PTCDI.[24,25] This enabled us to perform the comparative PPC studies employing different PTCDI molecules shown in Figure 3.1, from which the effect of electron donating group can be investigated.

3.3 Experimental Section

3.3.1 Synthesis of PTCDI Molecules and Fabrication Into Nanofiber Structures

The synthesis of MP-PTCDI, MA-PTCDI, MO-PTCDI, DD-PTCDI and CH-PTCDI followed the methods reported in our previous papers.[26-29] MT-PTCDI was synthesized similarly, as briefly described below. First, N-dodecyl-perylene-3,4,9,10-tetracarboxy monoimide monoanhydride was synthesized using the previously reported method.[26,27] 50 mg of the syntehsized monoanhydride was mixed with 4-(dimethylamino)butylamine (Sigma-Aldrich, 31.0 mg), zinc acetate (Sigma-Aldrich, ACS reagent, 98%, 1.0 mg) and imidazole (Sigma-Aldrich, ACS reagent, > 99%, 750.0 mg) in a tightly capped vial and

heated at 125 °C for 4 hours under magnetic stirring. The reaction was then terminated and cooled to room temperature, followed by addition of 2 N HCl solution to dissolve the imidazole. The red suspension was collected by filtration using 0.45 μm membrane filter and washed with distilled water and methanol. The red solid obtained was then dispersed in $CHCl_3$ (200 mL) and washed with saturated $NaHCO_3$ (Sigma-Aldrich, ACS reagent, ≥ 99.7%), water, brine and dried over Na_2SO_4 (Sigma-Aldrich, ACS reagent, > 99%). The product was then recrystallized from $CHCl_3$/CH_3CN and vacuum dried to afford 53.9 mg product (92%) as a very dark red solid. ^1H NMR (300 MHz, $CDCl_3$, TMS, ppm): δ = 8.55 (d, J = 6.0 Hz, 4H; perylene H), 8.45 (d, J = 6.0 Hz, 4H; perylene H), 4.24–4.16 (m, 4H; $(CO)_2NCH_2$), 2.35 (m, 2H; CH_2*$N(CH_3)_2$), 2.24 (s, 6H; $N(CH_3)_2$), 1.86–1.18 (m, 24H; $12CH_2$), 0.87 (t, J = 6.0 Hz, 3H; CH_2CH_3*). MALDI-TOF-MS: $[M+H^+]/z$ = 658.43.

The nanofibers were fabricated by injecting 1 mL of a chloroform solution of the PTCDI compound (0.1 mmol L^{-1}) into 5 mL of ethanol. The nanofibers were formed after aging at room temperature in dark overnight.

3.3.2 In Situ PTCDI Nanofiber Fabrication on a Substrate

The MP-PTCDI thin film was prepared by drop-casting 10 μL MP-PTCDI solution in chloroform (0.1 mmol L^{-1}) on a silicon substrate covered with 300 nm thick SiO_2 layer (with or without the pre-patterned IDEs). The freshly prepared thin film was dried in air for 1 h, or aged in an oven at 60 °C for 72 h, or annealed with ethanol vapor in a sealed chamber for 24 h. The ethanol-vapor annealing was conducted by placing the MP-PTCDI thin films into a sealed 60 mL jar, in which a 5 mL vial containing ethanol was placed to maintain the saturated vapor of ethanol. The films were kept in the vapor environment for

24 h to complete the annealing process.

3.3.3 MP-PTCDI Nanofibers Embedded in PEG-PPG-PEG Triblock Copolymer Matrix

The poly(ethylene glycol)-block-poly(propylene glycol)-block-poly(ethylene glycol) (PEG-PPG-PEG, average Mn ~1100, Sigma-Aldrich) was dissolved in ethanol. 10 μL MP-PTCDI solution in chloroform (0.1 mmol L^{-1}) was injected into the above PEG-PPG-PEG/ethanol solution (100 μL). The mass ratio of MP-PTCDI to PEG-PPG-PEG in this mixture is 10:1. After aging the mixture in dark overnight, the MP-PTCDI nanofibers were formed in situ in the polymer matrix and could be transferred onto the substrate for further measurements.

3.3.4 Materials Characterization

UV−vis absorption spectra were acquired with an Agilent Cary 100 UV-visible spectrophotometer. Fluorescence spectra were collected with an Agilent Eclipse spectrophotometer. SEM measurement was performed on an FEI Nova Nano 630 (FEI Corporation) with a helix detector in low vacuum (0.43 Torr water pressure). AFM measurements were performed on a Veeco MultiMode V scanning probe microscope in tapping mode. A silicon substrate coated with a polished 300 nm thick SiO2 layer was used as the substrate for both AFM and SEM measurements. The bright field and fluorescence optical microscopy images were obtained with a Leica DMI4000B inverted microscope equipped with an Acton SP-2356 Imaging Spectrograph system and Princeton Instrument Acton PIXIS: 400B Digital CCD Camera System. X-ray diffraction

patterns of PTCDI nanofiber thin films were obtained using a Bruker D2 Phase X-ray diffractometer with Cu Kα (λ = 1.5418 Å). The thin films for XRD measurement were prepared by drop-casting PTCDI nanofibers onto a clean glass slide substrate (D = 1.5 cm). Kelvin probe force microscopy (KPFM) was achieved on Bruker Dimension Icon scanning probe microscope. The surface potential was measured using Lift Mode with a conductive antimony doped silicon tips (SCM-PIT, Bruker) along with a cantilever coated with 20 nm Pt/Ir on both sides. Indium-doped tin oxide (ITO) coated glass slides (Delta Technology, R = 5-15 Ω) were used as the substrate for KPFM measurements.

3.3.5 Electrical Current Measurement

Interdigitated electrodes (IDEs) were used for all electrical current measurements in this work. The IDEs have a channel width of 2100 μm and a gap length of 80 μm, and was fabricated by a standard photolithography procedure on a silicon wafer covered with a 300 nm thermal oxide layer (Silicon Quest International). The electrodes were patterned by sputtering with 20 nm thick titanium adhesion layer and 50 nm thick gold layer. The electrical conductivity was measured under ambient conditions using a two-probe method on a Signatone S-1160 Probe Station combined with an Agilent 4156C Precision Semiconductor Analyzer. The *I-V* curves were measured for all the six PTCDI nanofibers both under dark and illumination in the bias range of 0-15 V. Typical *I-V* curves are shown in Figure 3.2. Although most nanofibers show linear relationship, some nanofiber like DD-PTCDI showed roughly two linear ranges, with smaller slope in low bias and higher slope in higher bias for the photocurrent. Therefore, the medium bias of 7 V was chosen for the photocurrent and PPC measurements. A tungsten lamp (Quartzline, 21 V,

150 W) was used as the white light source, and the light is guided into the probe station through a glass optical fiber, followed by focusing on the sample through the objective lens. The tungsten lamp used in this study provides white light covering from 400 nm to 900 nm, as measured in our previous study.[30] This white light was used here because it provides the visible light with energy in the absorption region of the PTCDI nanofibers (400-650 nm, Figure 3.3), which can initiate the highest occupied molecular orbital (HOMO) to lowest unoccupied molecular orbital (LUMO) transition of PTCDI,[27] thus enabling the electron transfer from the amine (lone pair) to the one-electron missed HOMO of singlet state of PTCDI. The irradiation power density can be adjusted with the illuminator (Dolan-Jenner Fiber-Lite MI-150 Fiber Optical Illuminator, 150 W). The optical power reaching the sample surface was measured by a power meter (Mells Griot broadband power/energy meter, 13PEM001). All the samples used for persistent photoconductivity study were stored under vacuum in dark at room temperature for two days before the measurement. To compare the persistent photoconductivity of different PTCDIs, the nanofibers were assembled by injecting 10 μL PTCDI solution in chloroform (0.1 mmol L^{-1}) into 100 μL ethanol. The as-assembled nanofibers were dispersed well in ethanol, followed by being transferred onto the IDEs by slow drop-casting to ensure uniform coverage over the whole IDEs area. To study the temperature dependent PPC, the IDEs chip was placed on a heating stage, of which the temperature was controlled by a temperature controller (INSTEC, STC 200).

3.4 Results and Discussions

Figure 3.4 shows the PPC results obtained with the MP-PTCDI nanofibers deposited on IDEs. After maintaining a stable current in dark, the MP-PTCDI nanofibers were then illuminated by white light with a spot size covering the whole nanofiber area. The nanofibers demonstrated high photoconductivity upon illumination, producing a photocurrent on/off ratio ranging from ca. 18 to 71 with the illumination power density increasing from 0.31 to 5.77 mW cm-2 under a bias voltage of 7 V (Figure 3.4a and Table 3.1). After termination of illumination, the photocurrent relaxed quite slowly to the dark current level, and the decay rate depends significantly on the illumination power density (Figure 3.4b). The PPC decay curves can be well-fitted by a single stretched exponential decay (Equation 3.1), namely Kohlrausch's law, as widely reported in the literature on PPC effect,[10,13]

$$I_{(t)} = I_0 \exp[-(t/\tau)]^{\beta} \quad (0 < \beta < 1) \qquad 3.1$$

where I_0 is the photocurrent before the illumination is removed, τ is the decay time constant, representative of the time scale of the decay process, and β is the deviation from a single-exponential decay. The decay time constant τ of the MP-PTCDI nanofibers under illumination with various illumination power densities are shown in Figure 3.4c and summarized in Table 3.1. It is noted that the decay time constant decreases with the increase of illumination power density. Upon increasing the illumination power density, a higher concentration of free charger carriers should be produced within the MP-PTCDI nanofibers,[11,24,27] as evidenced by the increased photocurrent on/off ratio and the shorter

time required for achieving photocurrent equilibrium (Table 3.1). The higher concentration of free charge carriers leads to a greater probability of recombination of charge carriers, and consequently faster decay of the photocurrent. The PPC observed with the MP-PTCDI nanofibers was also found reproducible as confirmed by cycling on and off the illumination in 300 s intervals (Figure 3.4d). When the light was turned on, the current increased rapidly. Upon termination of the illumination, the current dropped to about 50% of the photocurrent within 300 s in the first cycle, and this "on" and "off" photoswitching remained reversible and reproducible in the following cycles. The lowest current obtained at 300 s after the termination of light still stays at the level of about 50% of the maximal photocurrent generated in the first cycle, though the photocurrent generated in the later cycles drifted lower to some extent, likely due to the photooxidation,[27,31-33] as the experiments were run in air.

We also observed the wavelength dependence of the photoconductivity and PPC effect of MP-PTCDI nanofiber materials by using long-pass filters with cut-on wavelength of 550 and 700 nm, while keeping the flux of photons constant in both cases. As shown in Figure 3.5, with the 550 nm filter, the photocurrent on-off ratio obtained for MP-PTCDI nanofibers was ca. 19 and a significant PPC effect was observed with decay time of 269 s, whereas when 700 nm filter was used, there was no photoconductivity obtained for the same nanofibers, simply because the wavelength above 700 nm has less than the bandgap energy to initiate the HOMO to LUMO transition of PTCDI.[27]

As extensively investigated with GaN, the PPC effect was found to be structure dependent.[34],[35] For example, when fabricated as nanorods, the PPC effect of GaN was strongly related to the diameter of nanorods,[34] and a further enhanced PPC was observed

in nanoporous GaN formed by electrochemical etching.[35] Inspired by such research work on inorganic materials, we attempted to study how the structure (morphology) of MP-PTCDI materials would affect the PPC as observed in Figure 3.4. Taking advantage of the ease of molecular self-assembly of PTCDIs, the morphology of MP-PTCDI materials can be controlled via evaporation induced molecular assembly on the oxidized surface of silicon wafer (or silicon wafer pre-patterned with IDEs). Such in situ fabrication method allowed us to tune the morphology of molecular aggregates through thermal and solvent vapor annealing.[36] The AFM images in Figure 3.6 indicate the evolution of the MP-PTCDI nanofiber structure from the initially disordered particulate aggregate under different annealing processes. The drop-cast thin film formed directly from the evaporation in air showed partially dewetted patterns, and there was no obviously structure or ordered morphology (Figure 3.6a). By annealing at 60 °C for 72 h, an approximately uniform and worm-shaped pattern formed in the film (Figure 3.6b). Upon annealing in the vapor of ethanol (a poor solvent for MP-PTCDI) for 24 h, well-defined nanofiber structures were established (Figure 3.6c), where the dimension of the nanofibers is about 500-800 nm in length, and 200 nm in width. We investigated the PPC effect with the three MP-PTCDI thin films annealed under different conditions, and the results are shown in Figure 3.6d. The as prepared thin film shows the fastest decay in current (with $\tau = 53 \pm 3$ s), followed by the film thermally annealed at 60 °C ($\tau = 93 \pm 6$ s), and the nanofiber film annealed in ethanol vapor shows the slowest decay ($\tau = 119 \pm 10$ s). Clearly, the self-assembled 1D nanostructure with the most organized molecular packing through π-π stacking enhances the PPC effect in MP-PTCDI.

The PPC was also found to be dependent on the molar amount of MP-PTCDI

nanofibers deposited on the IDEs. The decay time constant increased with the molar amount of nanofibers, while the rate of increase slowed when more than 1 nmol of nanofibers were deposited, mainly because the efficient conductive channel of MP-PTCDI nanofibers becomes saturated on the IDEs used (Figure 3.7). We also investigated the PPC in a control sample, in which MP-PTCDI nanofibers were dispersed in a PEG-PPG-PEG polymer matrix. Upon dispersing in polymer matrix, the inter-fiber contact would be insulated by the polymer, thus excluding the possibility that the inter-fiber contact (junction) may contribute to the observed PPC. As expected, the average width of the fibers is now 200 nm larger than the value of pristine MP-PTCDI nanofibers due to the surface coating of polymers (Figure 3.8). The almost identical PPC observed in the control sample (Figure 3.9, the decay time of 103 s and 102 s for the pristine MP-PTCDI nanofibers and those embedded in polymer, respectively) suggested negligible contribution from the junctions of nanofibers. The origin of the PPC effect should be correlated to nanofiber structure and the 1D crystal lattice.

To further explore the mechanism of the observed PPC effect in the MP-PTCDI nanofibers, a series of other PTCDI molecules with different side groups were studied for comparison. Most of these PTCDIs contain a linear dodecyl chain on one side, but with different groups on the other side; CH-PTCDI is the only symmetric molecule with both sides substituted with cyclohexane group (Figure 3.1). All these PTCDIs were fabricated into nanofibers following the similar self-assembly process and investigated for the PPC under the same conditions as used for MP-PTCDI nanofibers. Interestingly, PPC was only found in the nanofibers fabricated from the PTCDIs substituted with strong electron-donating groups, such as MP-PTCDI, MT-PTCDI and MA-PTCDI (Figure 3.10), where

the PPC decay curves can be fitted with a single stretched exponential equation, as widely reported in the literature on PPC effect,[10,13] although the whole decay has a long tail that takes more than 1 h to reach the dark current baseline. In contrast, no significant PPC effect was observed for the nanofibers of PTCDIs with weak electron donors (e.g., MO-PTCDI, DD-PTCDI and CH-PTCDI), for which the photocurrent returned relatively quickly to the dark current level in less than 10 s, and the PPC decay curves of which do not fit into the same exponential equation (Equation 3.1), implying no significant PPC effect.

All the six PTCDI molecules employed in this work were found to form well-defined nanofibers as evidenced in Figure 3.8a, Figure 3.11 and our previous self-assembly studies.[26-29] The X-ray diffraction (XRD) patterns also indicate highly ordered 1D columnar microstructures, with the inter-columnar spacing determined by the well-defined peaks around 4.0°, to be 23.43, 21.08, 22.25, 27.35, 25.38 and 18.10 Å for MP-, MT-, MA-, MO-, DD- and CH-PTCDI nanofibers, respectively (Figure 3.12).[28,29,37,38] However, the detailed molecule packing patterns are different as revealed by XRD patterns because the side group modification affects the molecular packing.[25,28,37] From our observation and results in Figure 3.10, it is unlikely that the different molecular packing or slight difference in morphology contributes significantly to the PPC. For example, even though DD-PTCDI and CH-PTCDI demonstrate great difference in molecular packing due to the side group effect (slipped stacking along the [100] direction for DD-PTCDI[39,40] vs. flip-flap stacking for CH-PTCDI along the [100] direction[29]), none of them demonstrates significant PPC, implying that tuning the molecular packing does not likely produce PPC. Therefore, the observed PPC is more of correlation with the

donor-acceptor structure of PTCDI, which creates charge separation state through photoinduced electron transfer from the donor (the amine moiety) to acceptor (the PTCDI central core).[27,41] While the photoinduced electron transfer primarily occurs through an intramolecular process, it can also happen via an intermolecular process when the donor and acceptor are arranged in close proximity in the molecular assembly of nanofibers.[26,42,43] The charge separation between donor and acceptor can further be enhanced by the efficient electron delocalization along the π-π stacking of PTCDI planes.[2,24,26,27,44] When the charge (negative or positive) is trapped at a molecule site, it may change the local dipole moment and the molecule orientation in the stacking as well, thus creating a local defect. It has also been widely argued in literatures that charge traps may come from the donors (acting as nucleophilic sites) and acceptors (as electrophilic sites) depending on the D-A association, which in turn can be controlled by the D-A strength and relative ratio of D and A moieties, as applied in memory devices.[45] The electrostatic potential fluctuation around the defect acts as an energy barrier preventing the charge recombination between electrons and holes, leading to PPC, similar to what was observed in inorganic semiconductor materials as described by the RLPF model.[10,13-17]

The photoinduced charge separation within the MP-PTCDI nanofibers can be confirmed by Kelvin probe force microscopy measurement (KPFM), which images the surface potential change of material caused by charge separation.[43,46,47] As shown in Figure 3.13a, well-defined morphology of the MP-PTCDI nanofibers was imaged by the tapping mode AFM. Figure 3.13b and d show the surface potential images of MP-PTCDI nanofibers in dark and after illumination, respectively. The statistic distributions of the

relative surface potential measured accordingly are plotted in Figure 3.13c and e. Upon illumination, the surface potential of MP-PTCDI nanofibers became more negative (about -13 mV shift), indicating the significant charge separation driven by photoexcitation, which has been confirmed by the transient absorption spectral study.[48]

In addition to the photoinduced charge separation, strong electron donor can also initiate charge separation in the dark through steady state charge-transfer interaction between the MP moiety (1-Methylpiperidine moiety) on one molecule and the PTCDI part on the other molecule, as recently observed in our lab on the MP-PTCDI nanofibers[26] and other PTCDI materials.[44,49] The pre-formed charge carriers not only increase the electrical conductivity, but meanwhile also create more structural defects that enhance the PPC as discussed above. In contrast, the nanofibers of MA-PTCDI did not demonstrate such dark conductivity due to the lack of effective charge-transfer interaction between MA (N,N-Dimethylaniline moiety) and PTCDI, and as a result, the PPC effect observed was minimal compared to that of MP-PTCDI (Figure 3.10) likely due to the intrinsically low density of defects in MA-PTCDI material. On the other hand, significant PPC was observed for the nanofibers of MT-PTCDI (Figure 3.10), which can be attributed to the high density of charge carriers in steady state and the more defects thus created, similar to the case of MP-PTCDI. To confirm the steady state charge transfer within MT-PTCDI nanofibers, we measured the fluorescence of both the molecular solution in chloroform (Figure 3.14) and the nanofibers deposited on quartz surface (Figure 3.15). The strong fluorescence measured for the MT-PTCDI molecules implies no photoinduced intramolecular electron transfer, which is consistent with the long donor-acceptor distance between the terminal amine and PTCDI.[26,27,50] However,

when assembled into nanofibers the MT-PTCDI molecules stack closely together, thus bringing the MT (N,N-Dimethylbutylamine moiety) and PTCDI moieties in proximity, allowing for effective charge transfer interaction, as supported by the complete fluorescence quenching in the nanofiber state (Figure 3.15). Such strong intermolecular charge transfer interaction would increase the charge carrier density, as well as the defects that account for the significant PPC observed. The increased charge carrier density within MT-PTCDI nanofibers was also evidenced by the high dark current measured (0.008 μA at a bias of 7 V), comparable to that of MP-PTCDI nanofibers (0.010 μA at a bias of 7 V), but much higher than that of MA-PTCDI nanofibers (7.0×10^{-5} μA at a bias of 7 V), which were all measured under the same conditions.

According to the RLPF model,[10,13-17] we attribute the observed PPC in PTCDI nanofibers to the charge relevant defects, which generate a potential barrier preventing the recombination of photogenerated charge carriers. The potential barrier can be estimated from the temperature dependent measurement of the PPC decay kinetics. Figure 3.16 shows the typical PPC decay curves measured on the MP-PTCDI nanofibers at different temperatures. It is clearly seen that the PPC effect gets more significant with a decrease in temperature. The decay time constants extracted from the curves show rapid decreasing at higher temperature (Figure 3.17). This temperature dependence indicates a typical thermally activated process for the charge recombination, which can be described by an Arrhenius equation (Equation 3.2),[14,35]

$$\tau = \tau_0 \exp[\Delta E / k_B T] \qquad 3.2$$

where τ is the decay time constant at any experimental temperature, τ_0 is the decay time constant at temperature of zero K, ΔE is the potential barrier of the charge recombination, k_B is the Boltzmann constant, and T is the temperature in the unit of Kelvin. Logarithmic plot of τ as a function of 1/T should give a linear relationship (R^2 = 0.9840) as indeed shown in Figure 3.16b. The slope of the linear fit gives value of potential barrier, 137 meV. This value is on the same level as those reported for n-type GaN.[14,17] This high activation barrier helps prevent the charge recombination, thereby enhancing the photovoltaic or photocatalytic efficiency when these PTCDIs are used as the photoresponsive materials.

3.5 Conclusions

In conclusion, we have studied the PPC effect in PTCDI nanofiber materials. It was found that the PTCDIs containing strong electron donor groups demonstrated significant PPC effect when fabricated into nanofiber materials. This is likely due to the defects formed from the charge separation within the molecular stacks, wherein electrical potential barrier created around the defects prevent the recombination of the photogenerated charge carriers. The extended electron delocalization along the π-π stacking (the long axis of nanofiber) further enhances the charge separation, creating more charge relevant defects, resulting in more pronounced PPC. Since the charge recombination is typically a thermally activated process, the PPC shows strong temperature dependence. Linear fitting between the PPC decay time and temperature gives estimation of the activation barrier (energy), 137 meV, which is comparable to that obtained for the inorganic semiconductors such as n-type GaN. This work provides, for

the first time, systematic investigations on the PPC effect in PTCDI based materials (particularly the nanofibers), and the results will help understand the mechanism and design new material structures for sustained charge separation in order to further enhance the photovoltaic and photocatalytic efficiency of organic semiconductor materials.

3.6 References

(1) Chen, S.; Slattum, P.; Wang, C.; Zang, L. Self-Assembly of Perylene Imide Molecules Into 1D Nanostructures: Methods, Morphologies, and Applications. *Chem. Rev.* **2015**, *115*, 11967-11998.

(2) Zang, L.; Che, Y.; Moore, J. S. One-Dimensional Self-Assembly of Planar π-Conjugated Molecules: Adaptable Building Blocks for Organic Nanodevices. *Acc. Chem. Res.* **2008**, *41*, 1596-1608.

(3) Hains, A. W.; Liang, Z.; Woodhouse, M. A.; Gregg, B. A. Molecular Semiconductors in Organic Photovoltaic Cells. *Chem. Rev.* **2010**, *110*, 6689-6735.

(4) Li, L.; Jacobs, D. L.; Bunes, B. R.; Huang, H.; Yang, X.; Zang, L. Anomalous High Photovoltages Observed in Shish Kebab-Like Organic p-n Junction Nanostructures. *Polym. Chem.* **2014**, *5*, 309-313.

(5) Kim, J. Y.; Bard, A. J. Organic Donor/Acceptor Heterojunction Photovoltaic Devices Based on Zinc Phthalocyanine and a Liquid Crystalline Perylene Diimide. *Chem. Phys. Lett.* **2004**, *383*, 11-15.

(6) Wicklein, A.; Ghosh, S.; Sommer, M.; Würthner, F.; Thelakkat, M. Self-Assembly of Semiconductor Organogelator Nanowires for Photoinduced Charge Separation. *ACS Nano* **2009**, *3*, 1107-1114.

(7) Chen, S.; Jacobs, D. L.; Xu, J.; Li, Y.; Wang, C.; Zang, L. 1D Nanofiber Composites of Perylene Diimides for Visible-Light-Driven Hydrogen Evolution From Water. *RSC Adv.* **2014**, *4*, 48486-48491.

(8) Bu, L.; Pentzer, E.; Bokel, F. A.; Emrick, T.; Hayward, R. C. Growth of Polythiophene/Perylene Tetracarboxydiimide Donor/Acceptor Shish-Kebab Nanostructures by Coupled Crystal Modification. *ACS Nano* **2012**, *6*, 10924-10929.

(9) Chen, S.; Wang, C.; Bunes, B. R.; Li, Y.; Wang, C.; Zang, L. Enhancement of Visible-Light-Driven Photocatalytic H_2 Evolution from Water over *g*-C_3N_4 through Combination With Perylene Diimide Aggregates. *Appl. Catal., A* **2015**, *498*, 63-68.

(10) Wu, Y.-C.; Liu, C.-H.; Chen, S.-Y.; Shih, F.-Y.; Ho, P.-H.; Chen, C.-W.; Liang, C.-

T.; Wang, W.-H. Extrinsic Origin of Persistent Photoconductivity in Monolayer MoS_2 Field Effect Transistors. *Sci. Rep.* **2015**, *5*, 11472.

(11) Mukherjee, B.; Sim, K.; Shin, T. J.; Lee, J.; Mukherjee, M.; Ree, M.; Pyo, S. Organic Phototransistors Based on Solution Grown, Ordered Single Crystalline Arrays of a π-Conjugated Molecule. *J. Mater. Chem.* **2012**, *22*, 3192-3200.

(12) Draper, E. R.; Walsh, J. J.; McDonald, T. O.; Zwijnenburg, M. A.; Cameron, P. J.; Cowan, A. J.; Adams, D. J. Air-Stable Photoconductive Films Formed From Perylene Bisimide Gelators. *J. Mater. Chem. C* **2014**, *2*, 5570-5575.

(13) Jiang, H. X.; Lin, J. Y. Persistent Photoconductivity and Related Critical Phenomena in $Zn_{0.3}Cd_{0.7}Se$. *Phys. Rev. B: Condens. Matter Mater. Phys.* **1989**, *40*, 10025-10028.

(14) Chen, H. M.; Chen, Y. F.; Lee, M. C.; Feng, M. S. Yellow Luminescence in n-Type GaN Epitaxial Films. *Phys. Rev. B: Condens. Matter Mater. Phys.* **1997**, *56*, 6942-6946.

(15) Dissanayake, A. S.; Huang, S. X.; Jiang, H. X.; Lin, J. Y. Charge Storage and Persistent Photoconductivity in a $CdS_{0.5}Se_{0.5}$ Semiconductor Alloy. *Phys. Rev. B: Condens. Matter Mater. Phys.* **1991**, *44*, 13343-13348.

(16) Roy, K.; Padmanabhan, M.; Goswami, S.; Sai, T. P.; Ramalingam, G.; Raghavan, S.; Ghosh, A. Graphene-MoS_2 Hybrid Structures for Multifunctional Photoresponsive Memory Devices. *Nat. Nanotechnol.* **2013**, *8*, 826-830.

(17) Hirsch, M. T.; Wolk, J. A.; Walukiewicz, W.; Haller, E. E. Persistent Photoconductivity in n-Type GaN. *Appl. Phys. Lett.* **1997**, *71*, 1098-1100.

(18) Lang, D. V.; Logan, R. A. Large-Lattice-Relaxation Model for Persistent Photoconductivity in Compound Semiconductors. *Phys. Rev. Lett.* **1977**, *39*, 635-639.

(19) Konstantatos, G.; Badioli, M.; Gaudreau, L.; Osmond, J.; Bernechea, M.; de Arquer, F. P. G.; Gatti, F.; Koppens, F. H. L. Hybrid Graphene-Quantum Dot Phototransistors With Ultrahigh Gain. *Nat. Nanotechnol.* **2012**, *7*, 363-368.

(20) Chen, S.-Y.; Lu, Y.-Y.; Shih, F.-Y.; Ho, P.-H.; Chen, Y.-F.; Chen, C.-W.; Chen, Y.-T.; Wang, W.-H. Biologically Inspired Graphene-Chlorophyll Phototransistors With High Gain. *Carbon* **2013**, *63*, 23-29.

(21) Dutta, S.; Narayan, K. S. Nonexponential Relaxation of Photoinduced Conductance in Organic Field Effect Transistors. *Phys. Rev. B: Condens. Matter Mater. Phys.* **2003**, *68*, 125208.

(22) Bubb, D. M.; O'Malley, S. M.; Antonacci, C.; Belmont, R.; McGill, R. A.; Crimi, C. Observation of Persistent Photoconductivity in Conducting Polyaniline Thin Films. *Appl. Phys. A: Mater. Sci. Process.* **2005**, *81*, 119-125.

(23) Nga Ng, T.; Fujieda, I.; Street, R. A.; Veres, J. Persistent Photoconductivity Effects in Printed n-Channel Organic Transistors. *J. Appl. Phys.* **2013**, *113*, 094506.

(24) Zang, L. Interfacial Donor–Acceptor Engineering of Nanofiber Materials to Achieve Photoconductivity and Applications. *Acc. Chem. Res.* **2015**, *48*, 2705-2714.

(25) Würthner, F. Perylene Bisimide Dyes as Versatile Building Blocks for Functional Supramolecular Architectures. *Chem. Commun.* **2004**, 1564-1579.

(26) Wu, N.; Wang, C.; Bunes, B. R.; Zhang, Y.; Slattum, P. M.; Yang, X.; Zang, L. Chemical Self-Doping of Organic Nanoribbons for High Conductivity and Potential Application as Chemiresistive Sensor. *ACS Appl. Mater. Interfaces* **2016**, *8*, 12360-12368.

(27) Che, Y.; Yang, X.; Liu, G.; Yu, C.; Ji, H.; Zuo, J.; Zhao, J.; Zang, L. Ultrathin n-Type Organic Nanoribbons With High Photoconductivity and Application in Optoelectronic Vapor Sensing of Explosives. *J. Am. Chem. Soc.* **2010**, *132*, 5743-5750.

(28) Balakrishnan, K.; Datar, A.; Naddo, T.; Huang, J.; Oitker, R.; Yen, M.; Zhao, J.; Zang, L. Effect of Side-Chain Substituents on Self-Assembly of Perylene Diimide Molecules: Morphology Control. *J. Am. Chem. Soc.* **2006**, *128*, 7390-7398.

(29) Che, Y.; Yang, X.; Balakrishnan, K.; Zuo, J.; Zang, L. Highly Polarized and Self-Waveguided Emission From Single-Crystalline Organic Nanobelts. *Chem. Mater.* **2009**, *21*, 2930-2934.

(30) Bunes, B. R.; Xu, M.; Zhang, Y.; Gross, D. E.; Saha, A.; Jacobs, D. L.; Yang, X.; Moore, J. S.; Zang, L. Photodoping and Enhanced Visible Light Absorption in Single-Walled Carbon Nanotubes Functionalized With a Wide Band Gap Oligomer. *Adv. Mater.* **2015**, *27*, 162-167.

(31) Mateker, W. R.; Heumueller, T.; Cheacharoen, R.; Sachs-Quintana, I. T.; McGehee, M. D.; Warnan, J.; Beaujuge, P. M.; Liu, X.; Bazan, G. C. Molecular Packing and Arrangement Govern the Photo-Oxidative Stability of Organic Photovoltaic Materials. *Chem. Mater.* **2015**, *27*, 6345-6353.

(32) Sai, N.; Leung, K.; Zador, J.; Henkelman, G. First Principles Study of Photo-Oxidation Degradation Mechanisms in P3HT for Organic Solar Cells. *Phys. Chem. Chem. Phys.* **2014**, *16*, 8092-8099.

(33) Rivaton, A.; Tournebize, A.; Gaume, J.; Bussière, P.-O.; Gardette, J.-L.; Therias, S. Photostability of Organic Materials Used in Polymer Solar Cells. *Polym. Int.* **2014**, *63*, 1335-1345.

(34) Polenta, L.; Rossi, M.; Cavallini, A.; Calarco, R.; Marso, M.; Meijers, R.; Richter, T.; Stoica, T.; Lüth, H. Investigation on Localized States in GaN Nanowires. *ACS Nano* **2008**, *2*, 287-292.

(35) Lee, Y.-H.; Kang, J.-H.; Ryu, S.-W. Enhanced Photocurrent and Persistent

Photoconductivity in Nanoporous GaN Formed by Electrochemical Etching. *Thin Solid Films* **2013**, *540*, 150-154.

(36) Datar, A.; Oitker, R.; Zang, L. Surface-Assisted One-Dimensional Self-Assembly of a Perylene Based Semiconductor Molecule. *Chem. Commun.* **2006**, 1649-1651.

(37) Jones, B. A.; Facchetti, A.; Wasielewski, M. R.; Marks, T. J. Tuning Orbital Energetics in Arylene Diimide Semiconductors. Materials Design for Ambient Stability of n-Type Charge Transport. *J. Am. Chem. Soc.* **2007**, *129*, 15259-15278.

(38) Huang, Y.; Fu, L.; Zou, W.; Zhang, F.; Wei, Z. Ammonia Sensory Properties Based on Single-Crystalline Micro/Nanostructures of Perylenediimide Derivatives: Core-Substituted Effect. *J. Phys. Chem. C* **2011**, *115*, 10399-10404.

(39) Bao, Q.; Goh, B. M.; Yan, B.; Yu, T.; Shen, Z.; Loh, K. P. Polarized Emission and Optical Waveguide in Crystalline Perylene Diimide Microwires. *Adv. Mater.* **2010**, *22*, 3661-3666.

(40) Briseno, A. L.; Mannsfeld, S. C. B.; Reese, C.; Hancock, J. M.; Xiong, Y.; Jenekhe, S. A.; Bao, Z.; Xia, Y. Perylenediimide Nanowires and Their Use in Fabricating Field-Effect Transistors and Complementary Inverters. *Nano Lett.* **2007**, *7*, 2847-2853.

(41) Zang, L.; Liu, R.; Holman, M. W.; Nguyen, K. T.; Adams, D. M. A Single-Molecule Probe Based on Intramolecular Electron Transfer. *J. Am. Chem. Soc.* **2002**, *124*, 10640-10641.

(42) Che, Y.; Huang, H.; Xu, M.; Zhang, C.; Bunes, B. R.; Yang, X.; Zang, L. Interfacial Engineering of Organic Nanofibril Heterojunctions Into Highly Photoconductive Materials. *J. Am. Chem. Soc.* **2011**, *133*, 1087-1091.

(43) Huang, H.; Chou, C.-E.; Che, Y.; Li, L.; Wang, C.; Yang, X.; Peng, Z.; Zang, L. Morphology Control of Nanofibril Donor–Acceptor Heterojunction to Achieve High Photoconductivity: Exploration of New Molecular Design Rule. *J. Am. Chem. Soc.* **2013**, *135*, 16490-16496.

(44) Che, Y.; Datar, A.; Yang, X.; Naddo, T.; Zhao, J.; Zang, L. Enhancing One-Dimensional Charge Transport through Intermolecular π-Electron Delocalization: Conductivity Improvement for Organic Nanobelts. *J. Am. Chem. Soc.* **2007**, *129*, 6354-6355.

(45) Liu, C.-L.; Chen, W.-C. Donor-Acceptor Polymers for Advanced Memory Device Applications. *Polym. Chem.* **2011**, *2*, 2169-2174.

(46) Palermo, V.; Otten, M. B. J.; Liscio, A.; Schwartz, E.; de Witte, P. A. J.; Castriciano, M. A.; Wienk, M. M.; Nolde, F.; De Luca, G.; Cornelissen, J. J. L. M.; et al. The Relationship Between Nanoscale Architecture and Function in Photovoltaic Multichromophoric Arrays as Visualized by Kelvin Probe Force Microscopy. *J. Am. Chem. Soc.* **2008**, *130*, 14605-14614.

(47) Liscio, A.; De Luca, G.; Nolde, F.; Palermo, V.; Müllen, K.; Samorì, P. Photovoltaic Charge Generation Visualized at the Nanoscale: A Proof of Principle. *J. Am. Chem. Soc.* **2008**, *130*, 780-781.

(48) Walsh, J. J.; Lee, J. R.; Draper, E. R.; King, S. M.; Jäckel, F.; Zwijnenburg, M. A.; Adams, D. J.; Cowan, A. J. Controlling Visible Light Driven Photoconductivity in Self-Assembled Perylene Bisimide Structures. *J. Phys. Chem. C* **2016**, *120*, 18479-18486.

(49) Arulkashmir, A.; Jain, B.; John, J. C.; Roy, K.; Krishnamoorthy, K. Chemically Doped Perylene Diimide Lamellae Based Field Effect Transistor With Low Operating Voltage and High Charge Carrier Mobility. *Chem. Commun.* **2014**, *50*, 326-328.

(50) Adams, D. M.; Brus, L.; Chidsey, C. E. D.; Creager, S.; Creutz, C.; Kagan, C. R.; Kamat, P. V.; Lieberman, M.; Lindsay, S.; Marcus, R. A.; et al. Charge Transfer on the Nanoscale: Current Status. *J. Phys. Chem. B* **2003**, *107*, 6668-6697.

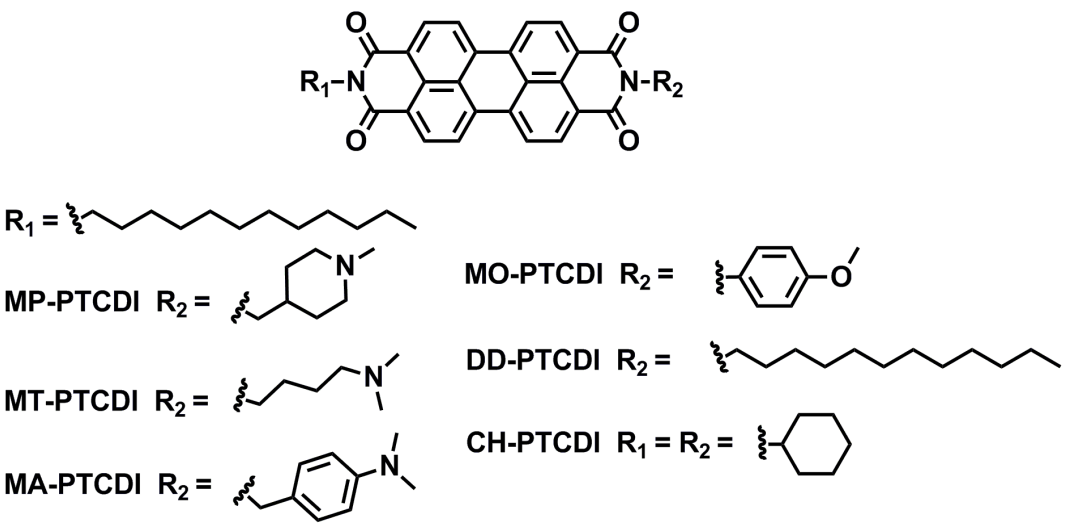

Figure 3.1 Molecular structures of PTCDI building blocks used in this study.

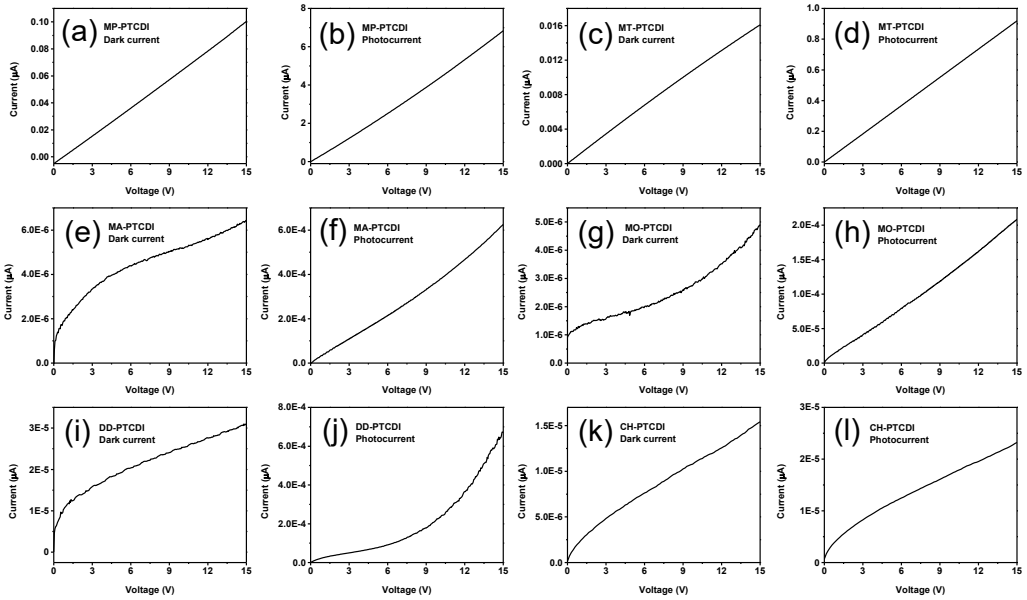

Figure 3.2 *I-V* curves of (a) MP-PTCDI, (c) MT-PTCDI, (e) MA-PTCDI, (g) MO-PTCDI, (i) DD-PTCDI and (k) CH-PTCDI nanofibers in dark; and (b) MP-PTCDI, (d) MT-PTCDI, (f) MA-PTCDI, (h) MO-PTCDI, (j) DD-PTCDI and (l) CH-PTCDI nanofibers with white light illumination (3.50 mW cm^{-2}).

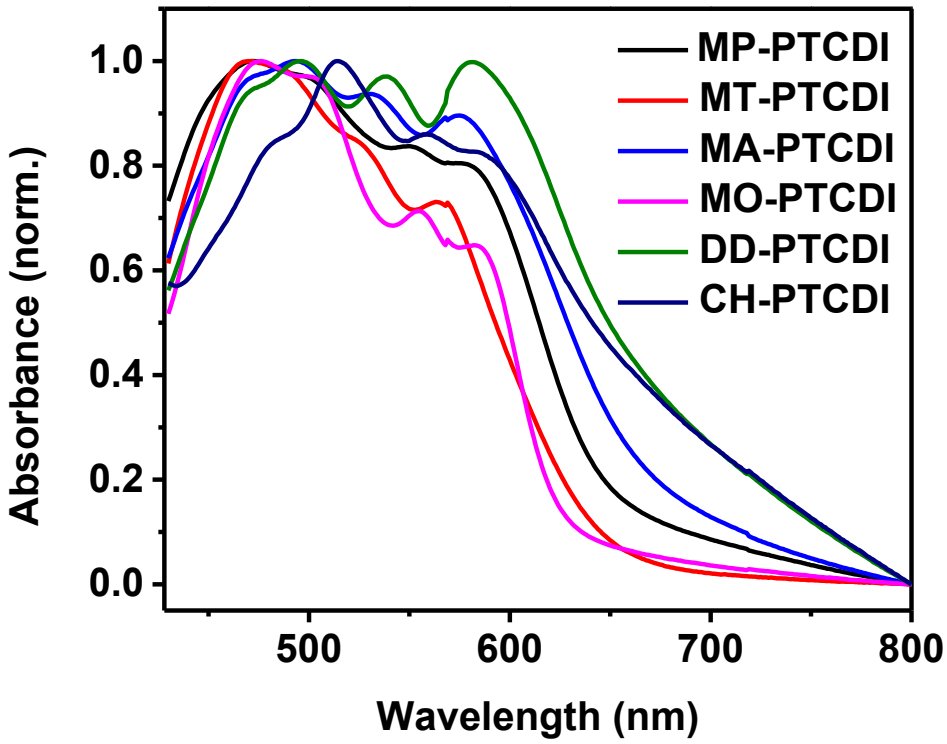

Figure 3.3 UV-vis absorption spectra of solid state PTCDI nanofibers studied in this work.

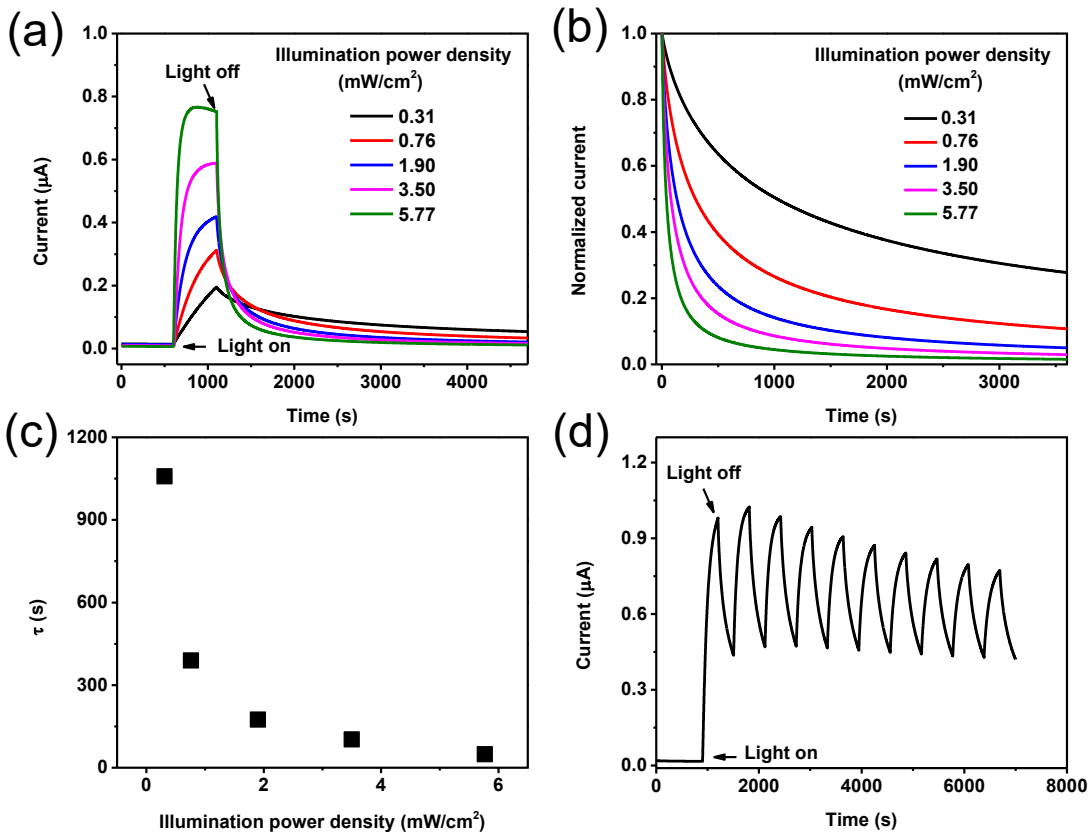

Figure 3.4 Photocurrent response of MP-PTCDI nanofibers: (a) electric current profiles of MP-PTCDI nanofibers under ambient condition with various white light illumination power densities; (b) decay of the photocurrent in panel a (normalized) generated at different illumination power densities after removal of the light; (c) photocurrent decay time constant (τ) as a function of illumination power density; (d) multi-cycle photocurrent response of the MP-PTCDI nanofibers by repeatedly switching on and off the illumination (3.50 mW cm^{-2}) in a 300 s interval. All the measurements were under the bias voltage of 7 V.

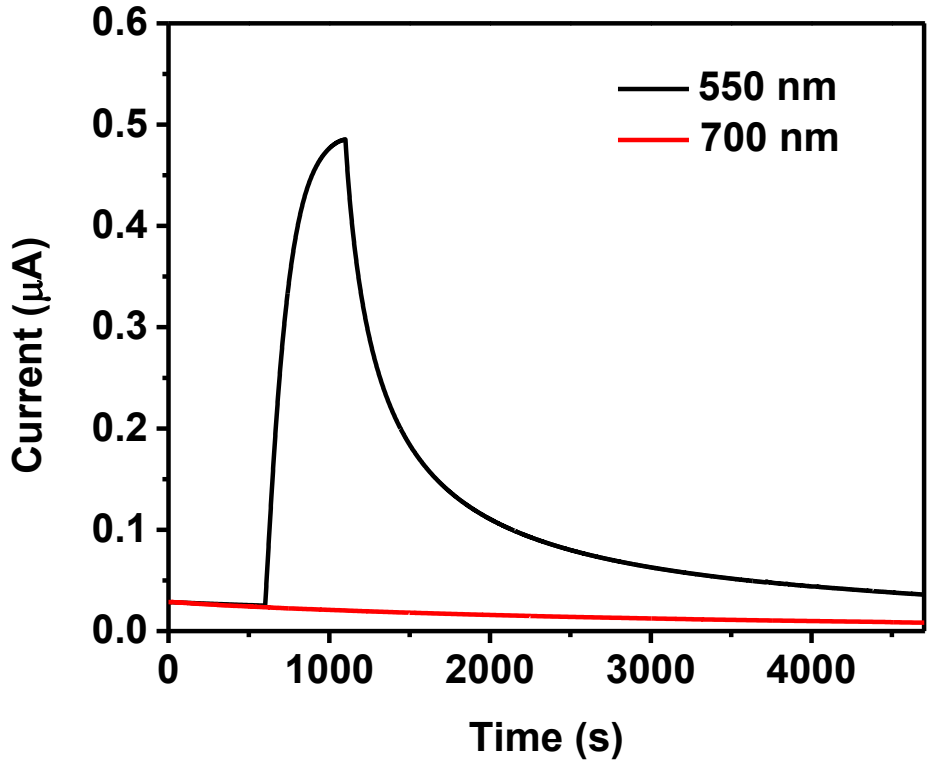

Figure 3.5 Wavelength-dependent photocurrent response of MP-PTCDI nanofibers using long-pass filters with cut-on wavelength of 550 and 700 nm; the flux of photons was kept constant for all the measurements.

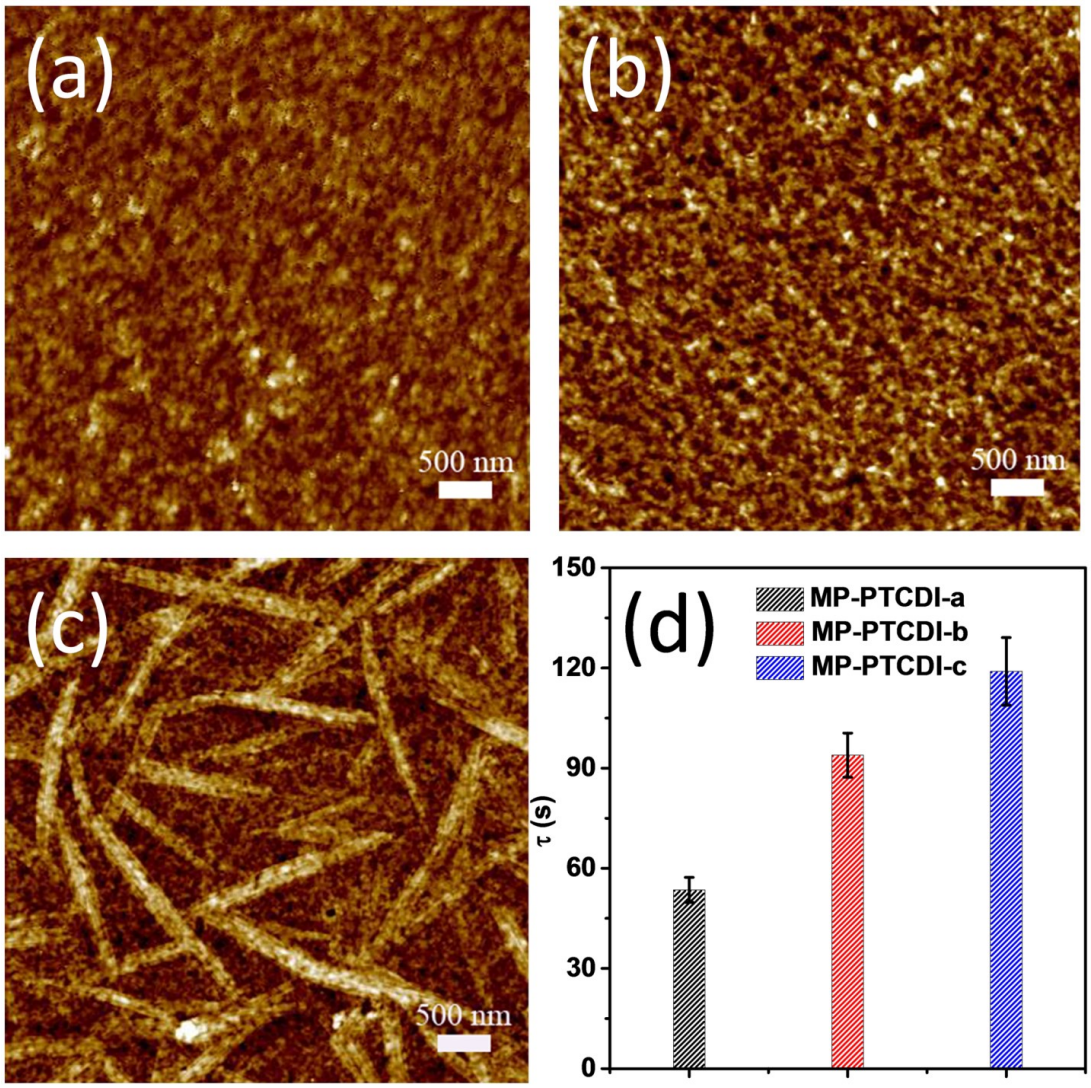

Figure 3.6 AFM images of MP-PTCDI thin film drop-cast on silicon wafer after consequent treatments: (a) dried in air for 1 h; (b) aged at 60 °C for 72 h; (c) annealed in ethanol vapor for 24 h; (d) comparison of the PPC decay time constant (τ) of the MP-PTCDI thin film deposited on silicon wafer pre-patterned with IDEs formed in panels a, b and c, respectively. The error bars represent the standard deviation based on the values measured by three independent devices of each condition. The irradiation power density was 3.50 mW cm^{-2}. The bias voltage was 7 V.

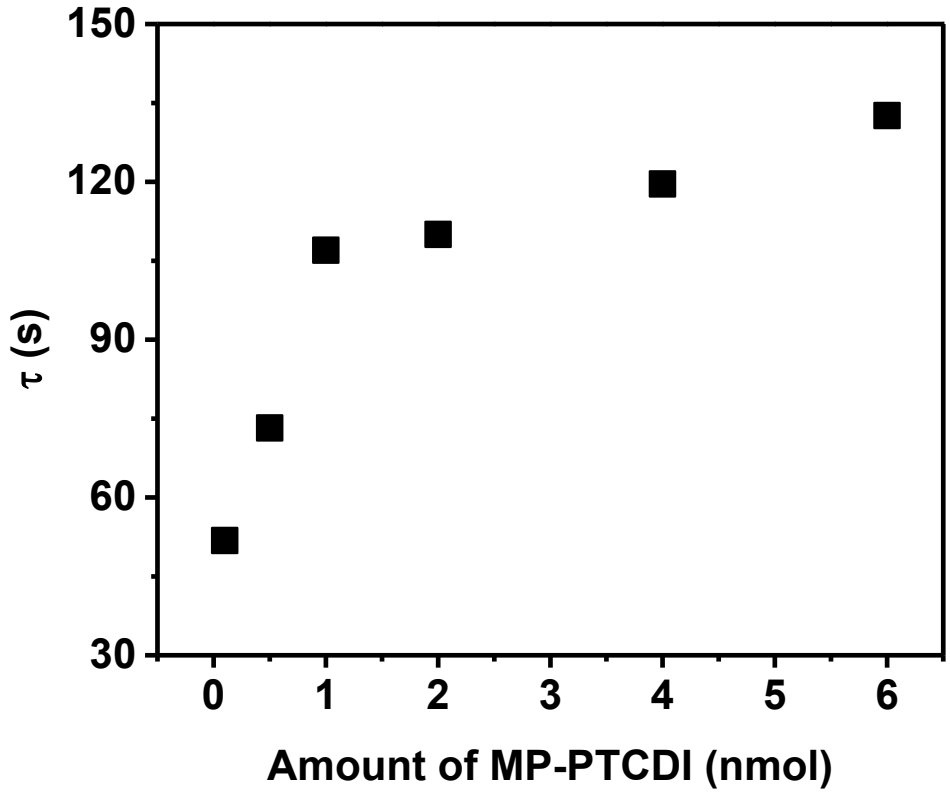

Figure 3.7 The decay time constant as a function of the molar amount of MP-PTCDI nanofibers deposited on the IDEs.

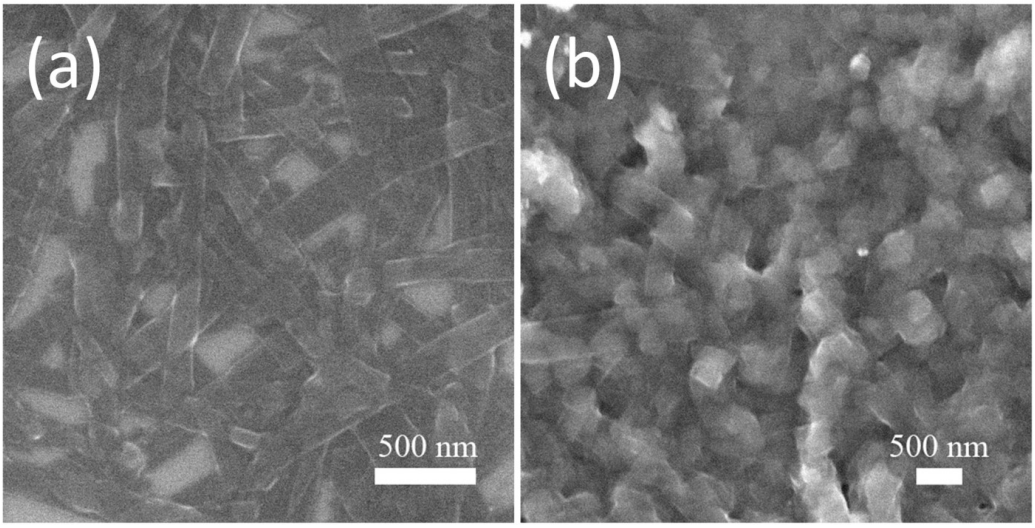

Figure 3.8 SEM images of (a) pristine MP-PTCDI nanofibers and (b) MP-PTCDI nanofibers embedded in PEG-PPG-PEG polymer matrix.

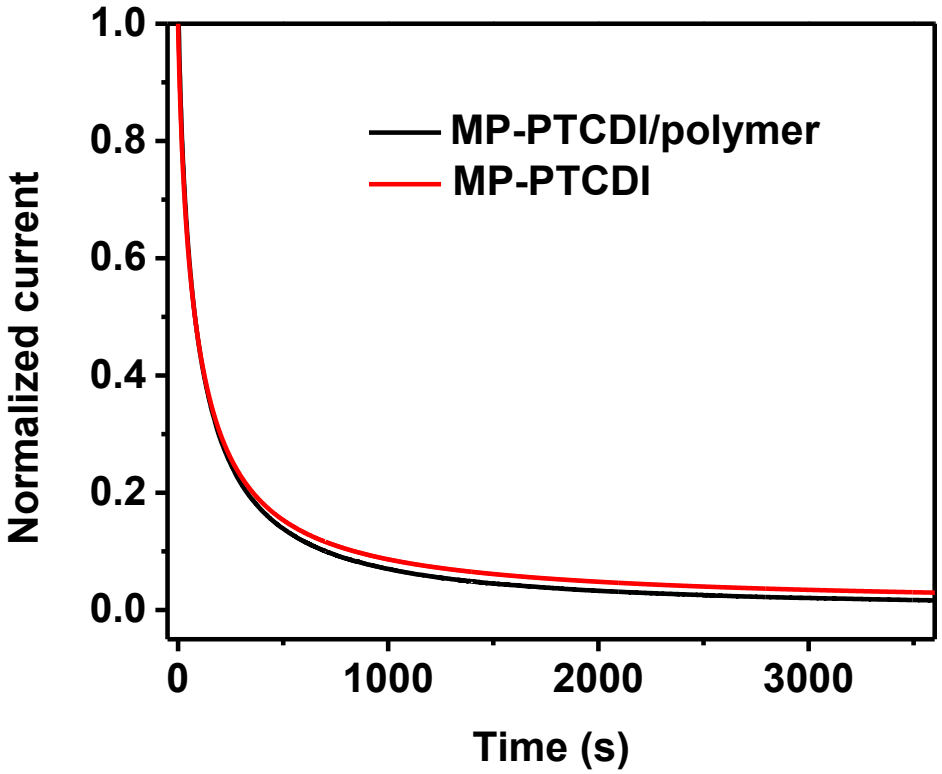

Figure 3.9 The PPC decay of MP-PTCDI nanofibers (red), in comparison to that of the nanofibers embedded in PEG-PPG-PEG matrix (black). The illumination power density was 3.50 mW cm^{-2}.

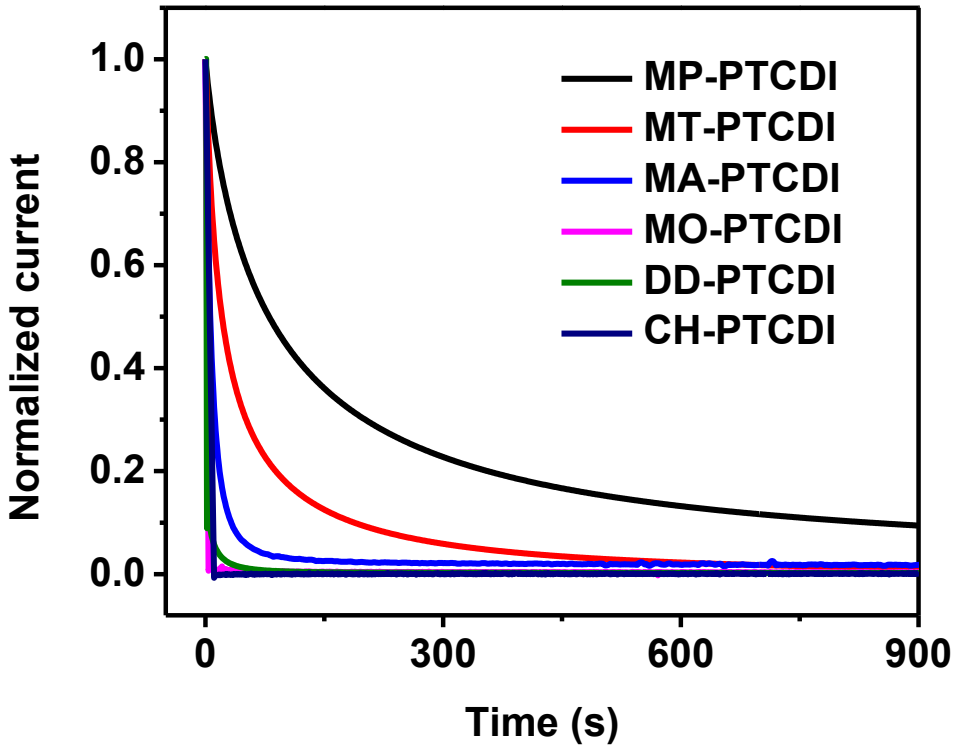

Figure 3.10 The PPC relaxation curves of various PTCDI nanofibril materials at room temperature. The irradiation power density was 3.50 mW cm^{-2}. The bias voltage was 7 V. The data were normalized to the photocurrent value right before turning off the light for each PTCDI nanofiber in order to compare the decay kinetics.

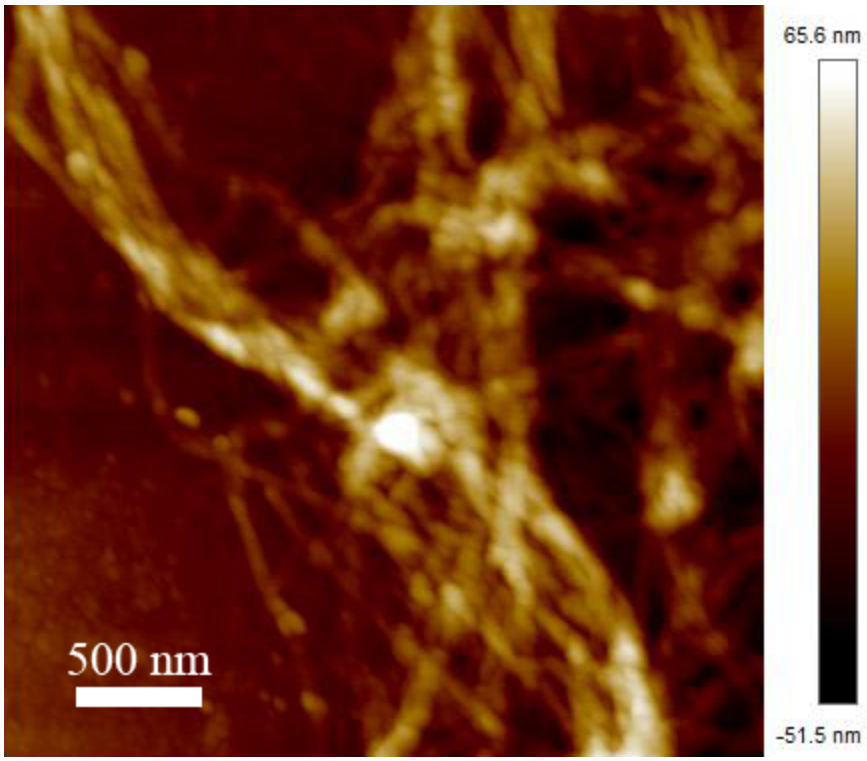

Figure 3.11 Tapping mode AFM topography image of MT-PTCDI nanofibers.

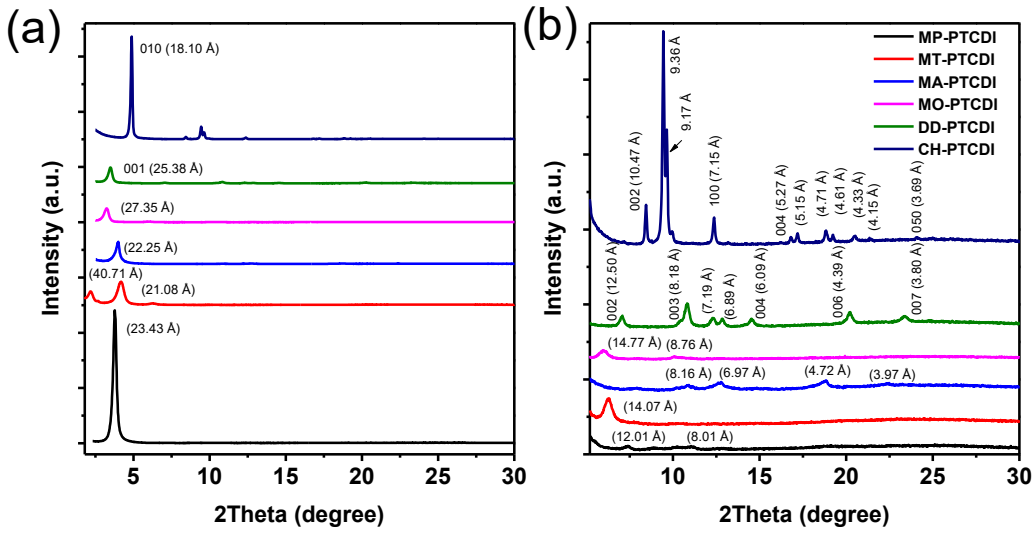

Figure 3.12 PTCDI nanofibers' crystal structures: (a) XRD patterns of PTCDI nanofibers studied in this work; (b) the full patterns ranging from 2θ = 5 to 30 degree. The XRD peaks of DD-PTCDI and CH-PTCDI nanofibers are in good agreement with the previous reports,[29,37,38] and can be indexed accordingly as marked in the figures. Since the single crystal structures of the other PTCDI materials (MP-PTCDI, MT-PTCDI, MA-PTCDI and MO-PTCDI) are unknown, we can't fully index the peaks, but the *d*-spacing values were calculated and labeled in the figures.

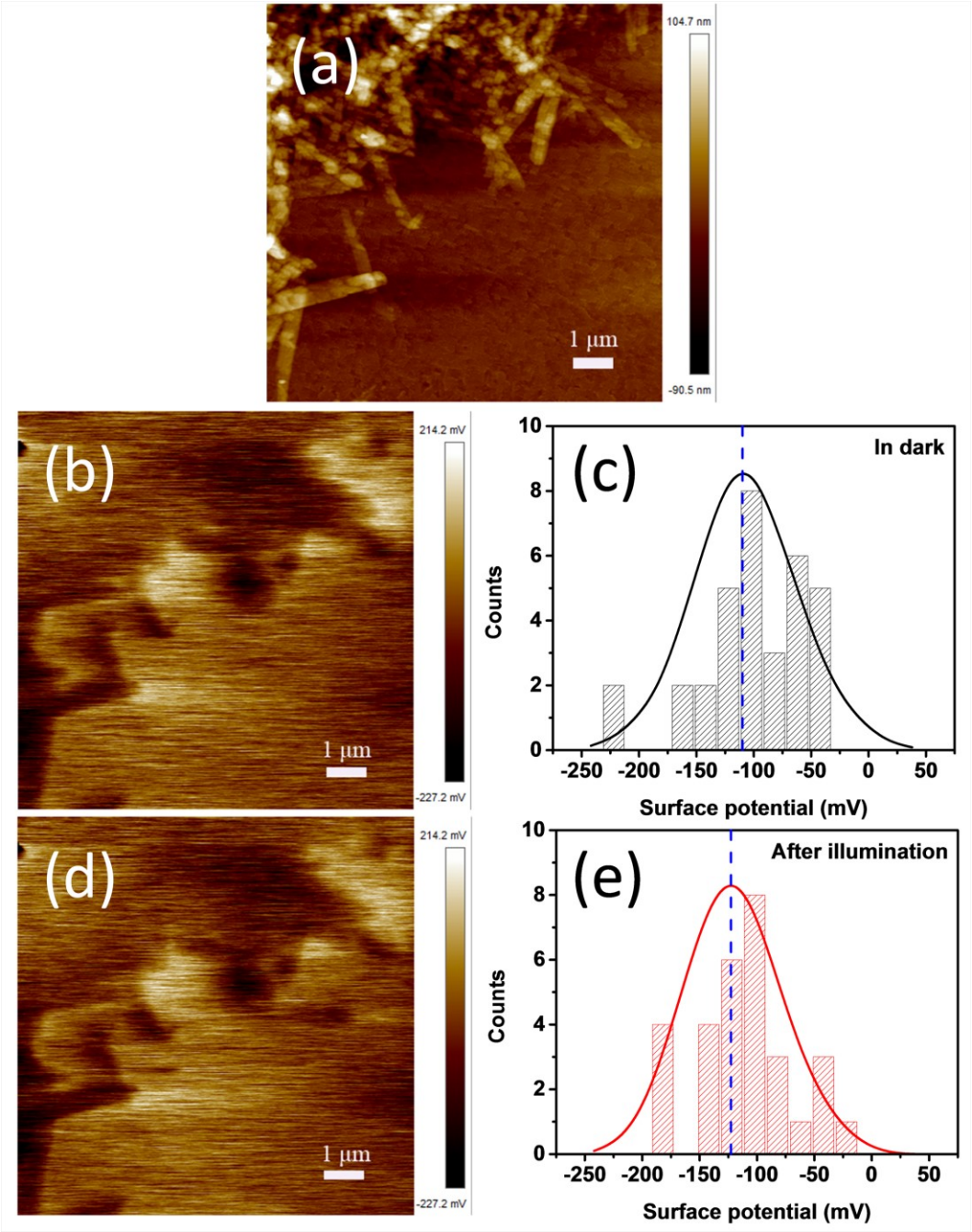

Figure 3.13 Evidences of photoinduced charge separation within the MP-PTCDI nanofibers: (a) tapping mode AFM topography image of MP-PTCDI nanofibers; surface potential images of the same area in panel a before (b) and after (d) illumination. The statistics distribution of the relative surface potential before (c) and after illumination (e).

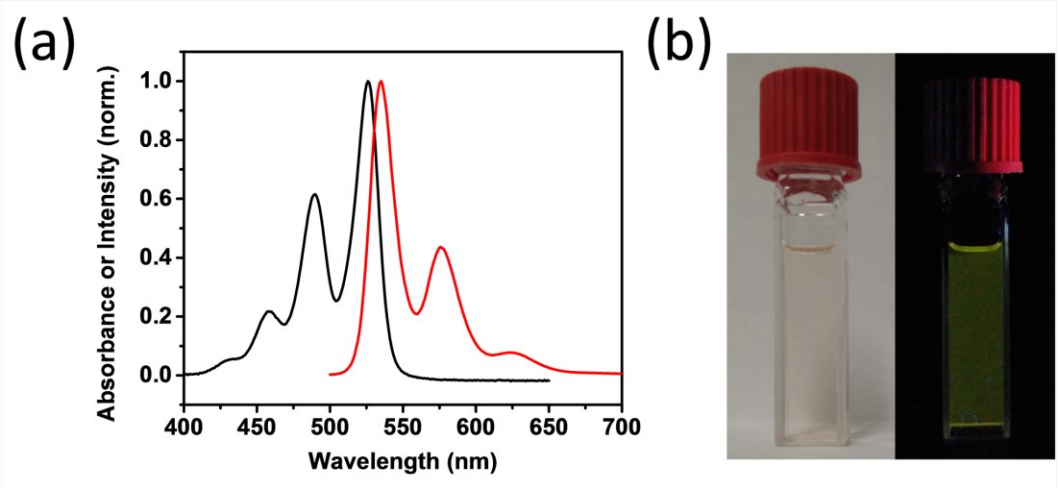

Figure 3.14 Study of MT-PTCDI solution in chloroform: (a) normalized UV-vis absorption (black) and fluorescence (red) spectra of MT-PTCDI solution in chloroform (2 μmol L^{-1}). The excitation wavelength for the fluorescence spectrum was 490 nm; (b) day light and fluorescence photographs (365 nm excitation) of 2 μmol L^{-1} solution of MT-PTCDI in chloroform.

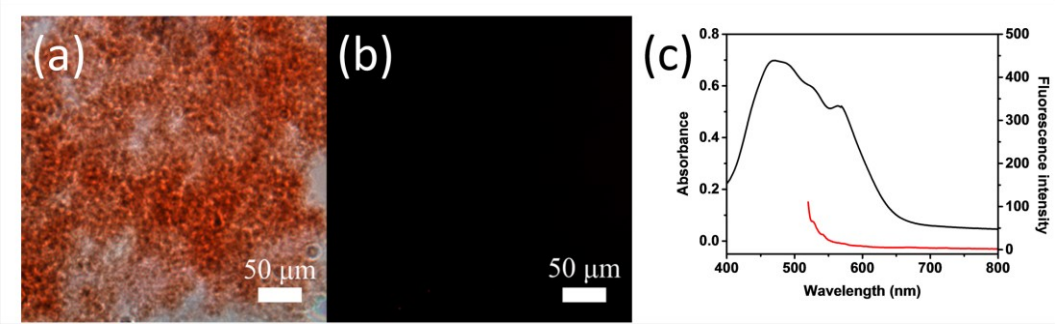

Figure 3.15 Morphology, UV-vis absorption, and fluorescence emission of MT-PTCDI thin film: (a, b) bright-field and fluorescence optical microscopy images of MT-PTCDI nanofibers deposited on a quartz slide; (c) UV-vis absorption (black) and fluorescence (red) spectra of MT-PTCDI nanofibers. The excitation wavelength for the fluorescence spectrum was 510 nm.

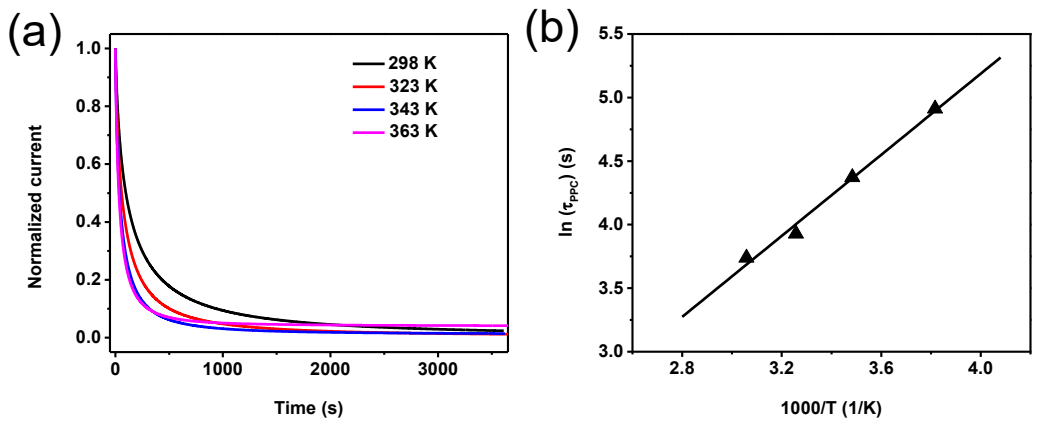

Figure 3.16 Temperature dependent PPC decay of MP-PTCDI nanofibers: (a) PPC decay curves of MP-PTCDI nanofibers measured at different temperatures; (b) logarithmic plot of the decay time constant as a function of reciprocal of temperature. The illumination power density was 3.50 mW cm^{-2}, and the bias voltage was 7 V.

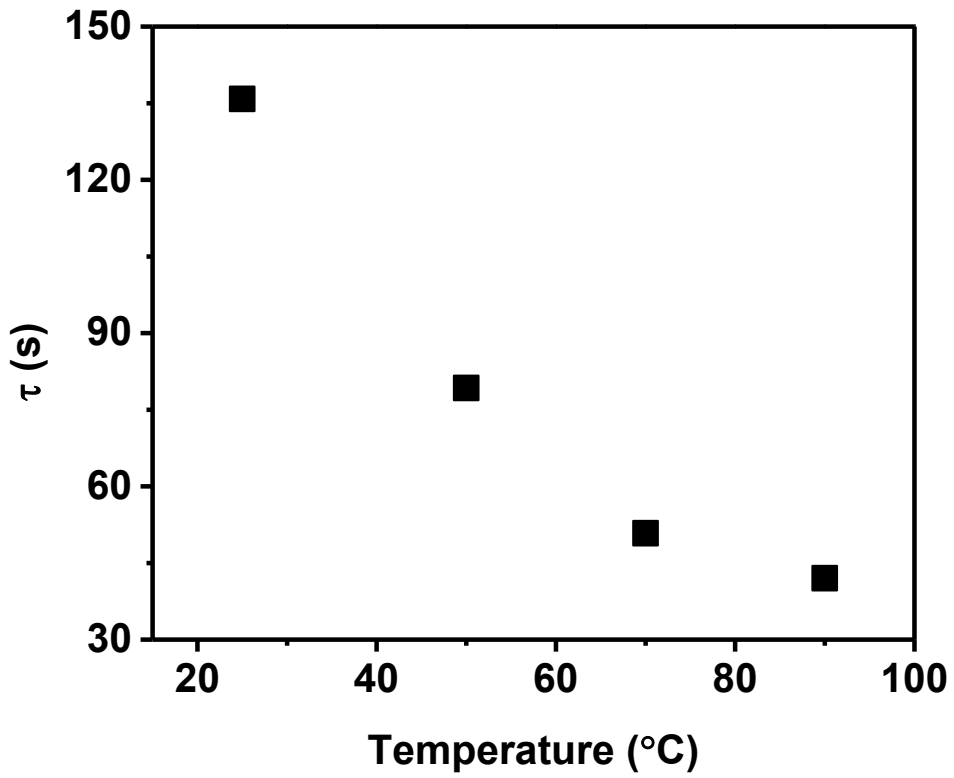

Figure 3.17 The PPC decay time constant (τ) of MP-PTCDI nanofibers at various temperatures.

Table 3.1 The photocurrent on/off ratio, decay time constant of MP-PTCDI nanofibers, and photocurrent equilibrium time under illumination with various power densities.

Irradiation power density (mW cm^{-2})	Photocurrent on/off ratio	Decay time constant (τ, s)	Photocurrent equilibrium time (s)
0.31	18	1058	>500
0.76	29	389	>500
1.90	39	174	>500
3.50	55	103	400
5.77	71	48	200

CHAPTER 4

THERMOACTIVATED ELECTRICAL CONDUCTIVITY IN PERYLENE DIIMIDE NANOFIBER MATERIALS[1]

4.1 Abstract

Thermoactivated electrical conductivity has been studied on nanofibers fabricated from the derivatives of perylene tetracarboxylic diimide (PTCDI) both in the dark and under visible light illumination. The activation energy obtained for the nanofibers fabricated from donor−acceptor (D−A) PTCDIs are higher than that for symmetric n-dodecyl substituted PTCDI. Such difference originates from the strong dependence of thermoactivated charge hopping on material disorder, which herein is dominated by the D−A charge-transfer and dipole−dipole interactions between stacked molecules. When the nanofibers were heated above the first phase transition temperature (around 85 °C), the activation energy was significantly increased because of the thermally enhanced polaronic effect. Moreover, charge carrier density can be increased in the D−A nanofibers under visible light illumination. Consistent with the theoretical models in the literature,

---

[1] Reprinted with permission from Wu, N.; Zhang, Y.; Wang, C.; Slattum, P. M.; Yang, X.; Zang, L., Thermo-activated Electrical Conductivity in Perylene Diimide Nanofiber Materials. *J. Phys. Chem. Lett.* **2017**, *8*, 292-298.

the increased charge carrier density did cause decrease in the activation energy due to the up-shifting of Fermi level closer to the conduction band edge.

4.2 Introduction

Organic semiconductor materials have drawn increasing attention in both fundamental and application research, mainly because of the unique features of these materials in comparison to those of conventional inorganic counterparts.[1-4] The typical features include structure and property flexibility through molecular design and engineering, low temperature solution processability, and mechanical conformity to different shapes of substrate. Organic semiconductors have been employed in a wide variety of electronic and optoelectronic devices, such as transistors, diodes, sensors, solar cells, and light-emitting devices. The operation performance of these device systems is usually highly concerned with the electrical conductivity (or the charge transport) within the materials. Although the electrical conductivity of the organic semiconductor is primarily determined by the intrinsic structure (e.g., molecular structure, intermolecular arrangement), some extrinsic physical parameters like temperature can also cause significant modulation in the conductivity through changing the carrier mobility via the so-called thermoactivated process. With this sensitive temperature dependence, some organic materials have been developed into temperature sensors,[5-7] which are suited for integration into wearable systems for in situ monitoring of human activity and personal healthcare.[8-10]

In general, the charge transport in organic materials relies on hopping between the localized energy states (trapped charges),[11-13] which can typically be described as a

thermoactivated process. Higher temperatures facilitate transport by providing the thermo-energy required to overcome the energetic barriers created by disorders. Arrhenius fitting of the conductivity as a function of temperature gives estimation of the activation energy. For many organic semiconductors (including conducting polymers), the activation energy was determined in the range of tens to hundreds of millielectronvolts.[13-15] The origin of the activation energy can be attributed to two major contributions, energetic disorder and polaronic effect.[13,16] The former is usually referred to the diagonal disorder, which is referred to the fluctuations in molecular electronic energies as arranged within the material. Such energetic disorder is commonly described as Gaussian distribution of the molecular electronic energies [mostly the highest occupied molecular orbital (HOMO) and lowest unoccupied molecular orbital (LUMO) level energies], which is usually referred as Gaussian disorder model (GDM).[16] While the diagonal disorder is mainly contributed by the conformational freedom of component molecules, it can also be induced by electrostatic or polarization effects from surrounding molecules, particularly when the molecules contain significant dipole moments (e.g., the electron donor-acceptor structure).[17,18] The polaron effect in organic materials is mainly due to molecular distortion caused by charging and decharging a molecule with an electron.[16,19,20] Hopping of an electron in this case is associated with both intramolecular and intermolecular reorganization in solid stacks. It is evidenced that the polaron effect can become more significant at elevated temperature because of the increased molecular vibration.[16]

Description of charge transport considers both the charge hopping rates between the localized sites and the density of charges involved in the hopping. Some well-established

models, such as the Miller-Abrahams model and that based on Marcus theory, have been developed to describe the hopping rate in disordered organic materials. With the varying densities of charges (e.g., modulated by gate voltage in field-effect transistors, or chemical doping through electron donor or acceptor modification), these theoretical models have been successfully applied in interpreting the observed temperature dependence of electrical conductivity of different organic materials. However, most of these studies were performed on the conducting polymers like those based on poly-phenylenevinylene (PPV) and poly(3-hexylthiophene) (P3HT), or the intrinsic (n- or p-type) molecular semiconductor materials such as the crystals of pentacene, rubrene or triphenylene.[13] We report therein on the temperature activated charge transport within self-doped organic semiconductors, which were assembled from the covalently linked electron donor-acceptor (D–A) molecules based on the derivatives of perylene tetracarboxylic diimide (PTCDI, Figure 4.1). As a unique air-stable n-type organic semiconductor, PTCDIs have been explored for various electrical or optical applications such as photovoltaics, light-emitting diodes, and photoelectric sensors.[1,21-23] More importantly, PTCDI materials offer robust thermal stability with decomposition temperature around 400 °C or above,[24] thus enabling investigation of thermoactivation in a wide high-temperature range.

D–A molecular materials provide increased electrical conductivity through the charge-transfer interaction between the donor and acceptor moieties, which in turn results in increase in charge carrier density.[1,25-27] Because of the effective self-doping, D–A materials have been widely employed in electronic and optoelectronic systems or devices, particularly photovoltaics. Despite the gain of increased conductivity, the D-A charge

transfer creates structural disorder and/or polaronic effect, which combined lead to increased energetic barrier for the charge hopping, meaning higher temperature will be needed to activate the charge transport. It therefore becomes imperative to study the temperature dependent charge transport of these materials. Moreover, most of the D-A materials are also photoconductive, i.e., light illumination of these materials initiates the electron transfer from D to A moiety, and further charge separation leads to increase in charge carrier density.[27] Increasing carrier density will shift up the Fermi level to the conduction band, resulting in decease in thermoactivation energy for the charge hopping, for which the activation barrier is generally considered as the energy difference between the trapped state and conduction band.[28,29] In this regard, the photoconductive feature of D-A materials provides an alternative way to study the thermoactivated charge transport by changing the carrier density, in a manner similar to that of the studies employing field-effect transistors (FET), wherein the charge carrier density can be modulated by the gate voltage.

4.3 Experimental Section

4.3.1 Synthesis of PTCDI Molecules and Fabrication of Nanofibers

The DD-PTCDI molecule was synthesized as the previously reported method.[30] BN-PTCDI and BNO-PTCDI molecules were synthesized following a similar procedure for asymmetric PTCDI molecules.[25,31] First, N-dodecyl-perylene-3,4,9,10-tetracarboxy monoimide monoanhydride compound was synthesized using the previously reported method.[25,31] Second, monoimide monoanhydride compound (490 mg), (4-piperidinophenyl)methylamine (500 mg, Sigma-Aldrich), $Zn(CO_2CH_3)_2$ (8 mg, Sigma-

Aldrich, ACS reagent, 98%) and imidazole (4.5 g, Sigma-Aldrich, ACS reagent, > 99%) were added into a 20 mL vial. The reaction mixture was stirred with a magnetic stir bar at 150 °C for 4 h. After cooling to room temperature, the above mixture was poured into 2N HCl to dissolve the imidazole. The remained product was collected by filtration and washed with distilled water and methanol. The resulting product was dispersed in chloroform (200 mL) and washed with saturated sodium bicarbonate, water, brine and dried over Na_2SO_4, followed by purified on a silica column eluting with 1.5 % ethanol in chloroform to yield 268 mg product. ^{1}H NMR (400 MHz, $CDCl_3$, ppm): δ = 8.84 (d, J = 8.0 Hz, 4H; perylene H), 8.81 (d, J = 8.0 Hz, 4H, perylene H), 7.73 (d, J = 8.4 Hz, 2H; benzene H), 7.47 (d, J = 8.4 Hz, 2H; benzene H), 5.52 (s, 2H; $(CO)_2NCH^*_2(C_6H_4)$), 4.27–4.24 (m, 2H, $(CO)_2NCH^*_2(CH_2)_{10}$), 3.78–3.61 (m, 4H; $C_6H_4N(CH^*_2)_2$), 2.07–1.26 (m, 26H; CH_2), 0.86 (t, J = 6.8 Hz, 3H; CH_3). MALDI-TOF-MS: $[M+H^+]/z$ = 732.43.

BNO-PTCDI molecule was synthesized as the same method as BN-PTCDI, except the corresponding amine of functional moiety was used and the amount of reactants were changed. For the synthesis of BNO-PTCDI, [4-(morpholin-4-yl)phenyl]methanamine (359 mg, Sigma-Aldrich) was used as the substitution reactant. The amount of the other reactants was 300 mg (monoimide monoanhydride), 5 mg ($Zn(CO_2CH_3)_2$) and 4.5 g (imidazole). The final product of BNO-PTCDI was 268 mg. ^{1}H NMR (400 MHz, $CDCl_3$, ppm): δ = 8.83 (d, J = 8.0 Hz, 4H; perylene H), 8.79 (d, J = 8.4 Hz, 4H, perylene H), 7.75 (d, J = 8.4 Hz, 2H; benzene H), 7.53 (d, J = 8.4 Hz, 2H; benzene H), 5.52 (s, 2H; $(CO)_2NCH^*_2(C_6H_4)$), 4.26–4.23 (m, 6H, $(CO)_2NCH^*_2(CH_2)_{10}$, $C_6H_4N(CH^*_2)_2$), 3.77 (m, 4H; $C_6H_4N(CH_2)_2(CH^*_2)_2O$), 1.76–1.26 (m, 20H; CH_2), 0.87 (t, J = 6.8, 3H; CH_3). MALDI-TOF-MS: $[M+H^+]/z$ = 734.33.

In this work, PTCDI molecules were self-assembled into nanofibers through a solvent exchange processing.[30] Typically, 1 mL of PTCDI solution in chloroform (0.1 mmol L^{-1}) was injected into 5 mL ethanol. The mixture was aged in the dark over night to facilitate the precipitation of the fibrous materials.

4.3.2 Materials Characterization

X-ray diffraction patterns of PTCDI nanofiber thin films were obtained using a Bruker D2 Phase X-ray diffractometer with Cu Kα (λ = 1.5418 Å). The thin films for XRD measurement were prepared by drop-casting PTCDI nanofibers into a clean glass slide substrate (D = 1.5 cm). Differential scanning calorimetry (DSC) measurements were conducted by a NETZSCH DSC 3500 calorimeter with a heating/cooling rate of 10 °C min^{-1}. Two heating-cooling cycles were performed for each sample. UV−vis absorption spectra were recorded with an Agilent Cary 100 UV-vis spectrophotometer. Fluorescence spectra were collected on an Agilent Eclipse spectrophotometer. The bright field and fluorescence optical images were obtained with a Leica DMI4000B inverted microscope equipped with an Acton SP-2356 Imaging Spectrograph system and Princeton Instrument Acton PIXIS: 400B Digital CCD Camera System for high resolution imaging. Atomic force microscopy (AFM) measurements were performed on a Veeco MultiMode V scanning probe microscope in tapping mode. Samples for AFM measurements were made by depositing PTCDI nanofibers on a silicon substrate coated with a polished 300 nm thick SiO_2 layer (Silicon Quest International), and drying in vacuum oven at room temperature in dark.

4.3.3 Temperature-Dependent Electrical Current Measurement

Interdigitated electrodes (IDEs) were used for all electrical current measurements. The IDEs were fabricated by a standard photolithography procedure on a silicon wafer with a 300 nm thermal oxide layer (Silicon Quest International). The electrodes were made by sputtering with 20 nm titanium adhesion layer and 50 nm gold layer. The IDE channel width and gap length was 1150 μm and 20 μm, respectively. The electrical conductivity was measured using a two-probe method on a Signatone S-1160 Probe Station combined with an Agilent 4156C Precision Semiconductor Analyzer. All the current measurements were under a bias voltage of 10 V. In the photocurrent measurement, the white light was supplied by a tungsten lamp (Quartzline, 21 V, 150 W) through a glass optical fiber. An objective lens was used to focus the light on the sample to insure the whole nanofiber thin film was covered by light. The optical power reaching the sample surface was measured by a power meter (Mells Griot broadband power/energy meter, 13PEM001). For the temperature-dependent current test, the IDE was placed on a hot stage connected with a temperature controller (INSTEC, STC 200). The temperature was increased from 25 to 120 °C with a rate of 2 °C min^{-1}. A layer of thermal paste (Arctic Sliver 5) was applied between the IDEs and the heating stage to improve the thermal transfer. The temperature change due to the white light irradiation is negligible.

4.4 Results and Discussion

The PTCDI D-A materials used in this study are in the nanofiber morphology (Figure 4.2), which are fabricated by solution self-assembly of the D–A molecules, BN-PTCDI and BNO-PTCDI. The one-dimensional (1D) morphology is dominated by the π–π

stacking of the planar PTCDI molecules, and the 1D molecular stacking facilitates the charge separation between the photogenerated electron and hole through the intermolecular π-electron delocalization.[27] The further increased charge density is conducive to studying the thermoactivated charge transport, for which the activation energy is related to the charge density as evidenced in the FET studies. Although PTCDI nanofiber materials have been extensively studied and used in varying applications (e.g., photovoltaics, sensors), there is little study reported yet on the temperature-dependent charge transport or electrical conductivity. The presented work would fill in this research gap, by providing improved understanding of the thermoactivated charge transport, and the observation may furthermore lead to development of wearable temperature sensors, taking advantages of the flexibility and small size of the nanofibers.

Along with the two D–A molecules, BN-PTCDI and BNO-PTCDI (Figure 4.1), a normal PTCDI molecule (without substitution of D moiety), DD-PTCDI, was also employed as a control in this study to investigate the effect of D–A structure and the photoinduced charge separation on the thermoactivated charge transport. While DD-PTCDI was synthesized following the same method previously reported,[30] BN-PTCDI and BNO-PTCDI were synthesized using a modified procedure as detailed in the Experimental Section. As expected, these PTCDI molecules form well-defined nanofibers when self-assembled in solutions (Figure 4.2a-c), mainly dictated by the strong π–π stacking interaction in between. All the nanofibers are in high aspect ratio with length in the range of a few tens of micrometers. The average width of the nanofibers, as estimated by atomic force microscopy (AFM) imaging, is ca. 263, 213 and 200 nm for BN-PTCDI, BNO-PTCDI and DD-PTCDI, respectively. These nanofibers

were then deposited onto interdigitated electrodes (IDEs) for electrical measurement and characterization (Figure 4.2d).

For all the three PTCDI nanofibers, the electrical current measured under the same conditions (as illustrated in Figure 4.2d) showed significant increase with temperature when heated from 25 to 120 °C (Figure 4.3). One typical heating–cooling cycle, as monitored over the BN-PTCDI nanofibers, is shown in Figure 4.4. The temperature responses observed were completely reversible, indicating the structure robustness of PTCDI materials under heating. Such robust repeatability assures the feasibility of applying these materials in temperature sensors in future. Among the three nanofibers, BN-PTCDI demonstrated the most sensitive response to temperature both in the dark and under white light illumination which creates photoconductivity as indicated by the much increased current. With the temperature increased from 25 to 120 °C, the current increased by a factor of 1350, 342 and 19 in the dark (Figure 4.3a) and 273, 67 and 17 under illumination (Figure 4.3b) for BN-PTCDI, BNO-PTCDI and DD-PTCDI, respectively. Under both dark and illuminated conditions, the relative increase of current with temperature of BNO-PTCDI is significantly smaller than that of BN-PTCDI, but is still much larger than that of DD-PTCDI. The more sensitive temperature dependence of current means higher energy barrier for the thermoactivated charge transport, and this can be seen more clearly from the activation energy, which can in turn be estimated from the linear fitting of the data in Figure 4.3 using the Arrhenius equation (Equation 4.1),[13,16]

$$I = I_0 e^{-\frac{E_A}{kT}} \qquad 4.1$$

where I is the electrical current measured under temperature T; k the Boltzmann constant; E_A the activation energy; and I_0 is the current when E_A is ignored, i.e., in the case of free charge transport. As shown in Figure 4.5, good linear fitting can be obtained for the data either in the low- (25–80 °C) or high-temperature range (80–120 °C) with a turning point around 80 °C, but not in the whole temperature range of experiment. The slope of the linear fitting gives the activation energiers, E_A, which are summarized in Table 4.1 for comparison between the three nanofibers. The two linear ranges may indicate two different phases of the material, which would be characteristic with different activation energy. Remarkably, the turning temperature indicated in Figure 4.5 (80 °C) is highly consistent with the result of DSC, wherein one phase transition temperature of 85 °C was observed for DD-PTCDI. For both the dark current and photocurrent measurements, larger activation energy was observed in the higher-temperature range for all the three nanofibers, implying that some additional contribution to the thermoactivation barrier was generated by increasing temperature. We attribute this additional contribution to the heating-enhanced intermolecular disorder, which in turn may also enhance the polaronic effect. As indeed indicated by the theoretical modeling,[16] at sufficiently high temperature (depending on materials) the polaronic effect can become more dominant than the energetic disorder in controlling the charge transport.

The activation energies shown in Table 4.1, particularly those obtained in low temperature range, are in good consistency with the values measured for the other organic semiconductors under the similar temperatures using the FET devices under varying temperatures.[13,14,32] Also in the lower-temperature range, the activation energies of the two D–A PTCDIs, BN-PTCDI and BNO-PTCDI, are much higher than that of DD-

PTCDI which contains no donor moiety. This can be explained by the much increased disorder within the D–A materials, wherein intermolecular D–A interaction (concerted with the strong dipole-dipole interaction) would distort the molecular arrangement, creating traps for the charge carriers. In contrast, the DD-PTCDI material is mostly controlled by the π–π stacking, for which there is little disorder contribution from the dipole–dipole interaction, considering the close to zero dipole moment of the symmetric molecule. When comparisons are made between BN-PTCDI and BNO-PTCDI in the low temperature range, the activation energy of the former is significantly higher than the latter, ca. 1.35 and 1.77 times for the dark current and photocurrent measurement, respectively. The higher activation energy of BN-PTCDI is apparently due to the stronger D–A interaction between the phenylpiperidine group and PTCDI in comparison to that between phenylmorpholine and PTCDI in BNO-PTCDI material. Indeed, as indicated by our density-functional theory calculation (Figure 4.6), the electron donating power (determined by the HOMO level) of phenylpiperidine is 0.13 eV stronger than that of phenylmorpholine. It is interesting to note that with temperature increasing to sufficiently high levels (here around 80 °C), the relative difference in activation energy between the three nanofibers becomes much smaller than that observed in the low temperature range. This implies that the thermally induced molecular disorder (e.g., conformational defects) at elevated temperature may override the effects of D–A or dipole–dipole interaction, which are usually dominant at low temperatures.

The enhanced low-temperature disorder of the two D–A PTCDI materials (compared to DD-PTCDI) as discussed above was also supported by the X-ray diffraction (XRD) and differential scanning calorimetry (DSC) measurements (Figure 4.7 and Figure 4.8).

Figure 4.7 shows the XRD patterns measured for BN-PTCDI, BNO-PTCDI and DD-PTCDI nanofibers. For DD-PTCDI nanofibers, well-defined XRD peaks are observed and can be indexed from (001) to (007), which are consistent with the previous reports on the same fiber materials (though fabricated with slightly different self-assembly procedures).[30,33,34] The d-spacing of 25.38 Å (deduced from the primary peak at 3.49°) corresponds to the intercolumnar distance, which is about half of the length of two DD-PTCDI molecules tail-to-tail interdigitated.[31,35] The 23.37° peak is indexed as the co-facial stacking between two PTCDI planes, and the calculated stack spacing (3.80 Å) is consistent with the typical π-π stacking distance as observed for other planar π-conjugated molecules.[31,34] To minimize the free energy caused by π-π electronic repulsion, a transverse and/or longitudinal offset is usually observed between the stacked PTCDI planes, resulting in a different edge-to-edge distance from the π-π stacking distance.[36] The *d*-spacing of 4.39 Å (calculated from the peak 20.21°) corresponds to the edge-to-edge distance between the two stacked DD-PTCDI planes, which take a tilted packing conformation. In contrast to the high-quality crystalline structure observed for DD-PTCDI, the structures of BN-PTCDI and BNO-PTCDI look less organized as indicated by the XRD patterns in Figure 4.7. The XRD peak intensity measured for the nanofibers of BN-PTCDI and BNO-PTCDI decreased by about 1 order of magnitude in comparison to that of DD-PTCDI nanofibers. Nonetheless, the intercolumnar spacings, 23.49 and 22.89 Å, as calculated for BN-PTCDI and BNO-PTCDI from the primary diffraction peaks, are quite close to the spacing value (25.38 Å) obtained for DD-PTCDI, indicating a similar cofacial π-π stacking arrangement drives the 1D growth of nanofibers in all the three PTCDIs.

Consistent with the XRD measurement, the DSC result also suggests less ordered structure for the two D-A PTCDI materials compared to DD-PTCDI. DSC is a common method used for studying the phase transition of molecular materials, including the PTCDIs.[30,37,38]. As shown in Figure 4.8, upon heating, DD-PTCDI nanofibers demonstrated three crystalline-crystalline transitions occurred at 85, 160 and 175 °C prior to the melting transition (T_m > 200 °C). When the sample was cooled, a dominant transition from mesophase to crystallization was observed at about 153 °C. Unlike DD-PTCDI, BN-PTCDI and BNO-PTCDI did not exhibit a clear phase transition upon heating, though during the cooling cycle a broad, asymmetric peak can be observed around 172 and 153 °C for BN-PTCDI and BNO-PTCDI, respectively, implying the transition from mesophase to crystallization phase. This observation suggests more disorder structure of the D-A PTCDIs compared to the highly organized molecular packing within DD-PTCDI. The high-quality crystalline structure of DD-PTCDI is mostly due to the symmetric molecular geometry substituted by two linear alkyl chains. This type of PTCDIs is conducive to forming organized columnar stacks in a manner similar to that of liquid crystal.[38] As discussed above, structure disorder leads to increased activation energy for charge transport, which is evidenced in our electrical current measurements shown in Figure 4.3 and Figure 4.5. Such disorder-dependent thermoactivation was also observed previously by others in pentacene thin-film transistors,[15] for which the films morphologies could be tuned and optimized by deposition of the film on a substrate at varying temperatures. Depending on the deposition temperature, different quality of films can be obtained, and low-temperature deposition usually led to low-quality film with more deep level traps, which in turn

resulted in large activation energy.

It is also interesting to be seen from Table 4.1 (Figure 4.5 as well) that the activation energy obtained particularly in the D-A PTCDI nanofibers was significantly decreased when measured under white light illumination in comparison to that in the dark. This decrease in activation energy is likely due to the increase in charge carrier density resulting from the photoinduced charge separation within the nanofibers. An increase in charge carrier density (here electrons for PTCDI) shifts up the Fermi level through the trap distribution, closer to the conduction band edge, and as a result, the thermal energy required to activate the trapped charge into hopping would be decreased. Such charge carrier density dependence of thermoactivation was evidenced or implied in other studies, both experimentally and theoretically, using the gate voltage to modulate the charge carrier density.[28,29]

The increase in charge carrier density upon illumination can be clearly seen from the dramatic increase in photocurrent compared to the dark current (Figure 4.3a, b). Indeed, the electrical current of the two D-A nanofibers, BN-PTCDI and BNO-PTCDI, was increased by more than 2 orders of magnitude when illuminated by white light. Such dramatic photoconductive enhancement is largely due to the photoinduced charge separation between the D moiety and PTCDI π-conjugated backbone (the A part), which produces increased density of charges.[27,31,39] The photocurrent response observed for DD-PTCDI under the same illumination condition was about 1 order of magnitude lower than that of the D-A PTCDIs, likely due to the lack of electron-donating groups. The photoinduced electron transfer from the D moieties to PTCDI is very thermodynamically favorable with a driving force of 0.74 and 0.61 eV for BN-PTCDI and BNO-PTCDI,

respectively (Figure 4.6). The transferred electron will be delocalized along the π–π stacks of PTCDIs, further enhancing the charge separation.[27] The photoinduced intramolecular electron transfer within the two D-A molecules was also evidenced by the efficient fluorescence quenching in both solutions and solid state (Figure 4.9 and Figure 4.10). As shown in Figure 4.9, the BN-PTCDI and BNO-PTCDI molecules dissolved in chloroform exhibit very weak fluorescence emission, whereas DD-PTCDI demonstrated strong fluorescence under the same conditions. The dramatic fluorescence quenching is due to the efficient photoinduced intramolecular electron transfer from the D moiety to PTCDI (as illustrated in Figure 4.6). Similar fluorescence quenching has been observed within many other D-A molecules, including the PTCDIs substituted with different amines.[31,40] To further confirm the intramolecular electron transfer, hydrochloric acid was added into the solution of BN-PTCDI or BNO-PTCDI to protonate the amines, in order to lower the energy level of the lone electron pair, thus blocking the photoinduced intramolecular electron transfer as evidenced before in numerous D-A molecular systems.[31,40] Indeed, the addition of hydrochloric acid resulted in strong fluorescence turning on as shown in Figure 4.9. Similarly, the significant fluorescence quenching was also observed in the solid state of BN-PTCDI and BNO-PTCDI nanofibers, whereas DD-PTCDI nanofibers remained strong fluorescent (Figure 4.10).

4.5 Conclusions

In conclusion, we have investigated the temperature dependent charge transport (measured as electrical current) for three PTCDI nanofibers with two in D-A structure (BN-PTCDI and BNO-PTCDI), and the third one without strong donor substitution (DD-

PTCDI). The results support the thermoactivated hopping mechanism for the charge transport, for which the activation energy was found to be primarily dependent on D-A structure. Indeed, both the D-A nanofibers showed activation energy that was significantly higher than that of the DD-PTCDI nanofibers for both the dark current and photocurrent measurements. D-A structure helps create disorder regarding both the charge-transfer and dipole-dipole interactions between stacked molecules, and the increased disorder enlarges the activation barrier. Significant increase in activation energy was found when heating the materials above the first crystallization to crystallization transition temperature, and this is likely due to the heating-enhanced intermolecular disorder, with which the polaronic effect may become more dominant in controlling the charge hopping process. Under visible light illumination, the electrical current of the nanofibers can be increased by orders of magnitude, thus providing the opportunity to examine the effect of charge carrier density on the activation energy of thermoactivated charge transport. As expected from the theoretical modeling in literature, the increased charge carrier density caused decrease in the activation energy because of the up-shifting of Fermi level through the energetic trap distribution in the bandgap. The photocurrent measurement offers an alternative way, in addition to the gate control in FET device, to modulate the charge density in material and investigate the effect on the thermoactivation of charge hopping. This work also reveals a trade-off regarding the design rules of D-A molecular materials. On one hand, D-A structure enables charge transfer and separation, particularly under light illumination, producing high conductivity, but on the other hand, the D-A materials are often more disordered compared to the neutral (low dipole) materials, thus resulting in higher activation energy

for charge transport. This may be conducive to developing more sensitive temperature sensors, but for many other electronic systems or applications more organized materials are usually required, which in turn demands more control of the intermolecular arrangement through molecular structural design and engineering.

4.6 References

(1) Hains, A. W.; Liang, Z.; Woodhouse, M. A.; Gregg, B. A. Molecular Semiconductors in Organic Photovoltaic Cells. *Chem. Rev.* **2010**, *110*, 6689-6735.

(2) Coakley, K. M.; McGehee, M. D. Conjugated Polymer Photovoltaic Cells. *Chem. Mater.* **2004**, *16*, 4533-4542.

(3) Samuel, I. D. W.; Turnbull, G. A. Organic Semiconductor Lasers. *Chem. Rev.* **2007**, *107*, 1272-1295.

(4) Sirringhaus, H. Organic Semiconductors: An Equal-Opportunity Conductor. *Nat. Mater.* **2003**, *2*, 641-642.

(5) Jung, S.; Ji, T.; Varadan, V. K. Temperature Sensor Using Thermal Transport Properties in the Subthreshold Regime of an Organic Thin Film Transistor. *Appl. Phys. Lett.* **2007**, *90*, 062105.

(6) Ren, X.; Chan, P. K. L.; Lu, J.; Huang, B.; Leung, D. C. W. High Dynamic Range Organic Temperature Sensor. *Adv. Mater.* **2013**, *25*, 1291-1295.

(7) Trung, T. Q.; Ramasundaram, S.; Hong, S. W.; Lee, N.-E. Flexible and Transparent Nanocomposite of Reduced Graphene Oxide and P(VDF-TrFE) Copolymer for High Thermal Responsivity in a Field-Effect Transistor. *Adv. Funct. Mater.* **2014**, *24*, 3438-3445.

(8) Trung, T. Q.; Lee, N.-E. Flexible and Stretchable Physical Sensor Integrated Platforms for Wearable Human-Activity Monitoringand Personal Healthcare. *Adv. Mater.* **2016**, *28*, 4338-4372.

(9) Chortos, A.; Liu, J.; Bao, Z. Pursuing Prosthetic Electronic Skin. *Nat. Mater.* **2016**, *15*, 937-950.

(10) Someya, T.; Kato, Y.; Sekitani, T.; Iba, S.; Noguchi, Y.; Murase, Y.; Kawaguchi, H.; Sakurai, T. Conformable, Flexible, Large-Area Networks of Pressure and Thermal Sensors With Organic Transistor Active Matrixes. *Proc. Natl. Acad. Sci. U. S. A.* **2005**, *102*, 12321-12325.

(11) Lu, N.; Li, L.; Banerjee, W.; Sun, P.; Gao, N.; Liu, M. Charge Carrier Hopping Transport Based on Marcus Theory and Variable-Range Hopping Theory in Organic Semiconductors. *J. Appl. Phys.* **2015**, *118*, 045701.

(12) Tessler, N.; Preezant, Y.; Rappaport, N.; Roichman, Y. Charge Transport in Disordered Organic Materials and Its Relevance to Thin-Film Devices: A Tutorial Review. *Adv. Mater.* **2009**, *21*, 2741-2761.

(13) Coropceanu, V.; Cornil, J.; da Silva Filho, D. A.; Olivier, Y.; Silbey, R.; Brédas, J.-L. Charge Transport in Organic Semiconductors. *Chem. Rev.* **2007**, *107*, 926-952.

(14) Horowitz, G.; Hajlaoui, M. E.; Hajlaoui, R. Temperature and Gate Voltage Dependence of Hole Mobility in Polycrystalline Oligothiophene Thin Film Transistors. *J. Appl. Phys.* **2000**, *87*, 4456-4463.

(15) Knipp, D.; Street, R. A.; Völkel, A. R. Morphology and Electronic Transport of Polycrystalline Pentacene Thin-Film Transistors. *Appl. Phys. Lett.* **2003**, *82*, 3907-3909.

(16) Fishchuk, I. I.; Kadashchuk, A.; Hoffmann, S. T.; Athanasopoulos, S.; Genoe, J.; Bässler, H.; Köhler, A. Unified Description for Hopping Transport in Organic Semiconductors Including Both Energetic Disorder and Polaronic Contributions. *Phys. Rev. B: Condens. Matter Mater. Phys.* **2013**, *88*, 125202.

(17) Dieckmann, A.; Bässler, H.; Borsenberger, P. M. An Assessment of the Role of Dipoles on the Density‐of‐States Function of Disordered Molecular Solids. *J. Chem. Phys.* **1993**, *99*, 8136-8141.

(18) Dunlap, D. H.; Parris, P. E.; Kenkre, V. M. Charge-Dipole Model for the Universal Field Dependence of Mobilities in Molecularly Doped Polymers. *Phys. Rev. Lett.* **1996**, *77*, 542-545.

(19) Chang, J.-F.; Sirringhaus, H.; Giles, M.; Heeney, M.; McCulloch, I. Relative Importance of Polaron Activation and Disorder on Charge Transport in High-Mobility Conjugated Polymer Field-Effect Transistors. *Phys. Rev. B: Condens. Matter Mater. Phys.* **2007**, *76*, 205204.

(20) Parris, P. E.; Kenkre, V. M.; Dunlap, D. H. Nature of Charge Carriers in Disordered Molecular Solids: Are Polarons Compatible With Observations? *Phys. Rev. Lett.* **2001**, *87*, 126601.

(21) Würthner, F.; Saha-Möller, C. R.; Fimmel, B.; Ogi, S.; Leowanawat, P.; Schmidt, D. Perylene Bisimide Dye Assemblies as Archetype Functional Supramolecular Materials. *Chem. Rev.* **2016**, *116*, 962-1052.

(22) Zang, L.; Che, Y.; Moore, J. S. One-Dimensional Self-Assembly of Planar π-Conjugated Molecules: Adaptable Building Blocks for Organic Nanodevices. *Acc. Chem. Res.* **2008**, *41*, 1596-1608.

(23) Chen, S.; Slattum, P.; Wang, C.; Zang, L. Self-Assembly of Perylene Imide Molecules into 1D Nanostructures: Methods, Morphologies, and Applications. *Chem. Rev.* **2015**, *115*, 11967-11998.

(24) Pasaogullari, N.; Icil, H.; Demuth, M. Symmetrical and Unsymmetrical Perylene Diimides: Their Synthesis, Photophysical and Electrochemical Properties. *Dyes Pigm.* **2006**, *69*, 118-127.

(25) Wu, N.; Wang, C.; Bunes, B. R.; Zhang, Y.; Slattum, P. M.; Yang, X.; Zang, L. Chemical Self-Doping of Organic Nanoribbons for High Conductivity and Potential Application as Chemiresistive Sensor. *ACS Appl. Mater. Interfaces* **2016**, *8*, 12360-12368.

(26) Huang, H.; Gross, D. E.; Yang, X.; Moore, J. S.; Zang, L. One-Step Surface Doping of Organic Nanofibers to Achieve High Dark Conductivity and Chemiresistor Sensing of Amines. *ACS Appl. Mater. Interfaces* **2013**, *5*, 7704-7708.

(27) Zang, L. Interfacial Donor–Acceptor Engineering of Nanofiber Materials to Achieve Photoconductivity and Applications. *Acc. Chem. Res.* **2015**, *48*, 2705-2714.

(28) Chesterfield, R. J.; McKeen, J. C.; Newman, C. R.; Ewbank, P. C.; da Silva Filho, D. A.; Brédas, J.-L.; Miller, L. L.; Mann, K. R.; Frisbie, C. D. Organic Thin Film Transistors Based on n-Alkyl Perylene Diimides: Charge Transport Kinetics as a Function of Gate Voltage and Temperature. *J. Phys. Chem. B* **2004**, *108*, 19281-19292.

(29) Fishchuk, I. I.; Kadashchuk, A. K.; Genoe, J.; Ullah, M.; Sitter, H.; Singh, T. B.; Sariciftci, N. S.; Bässler, H. Temperature Dependence of the Charge Carrier Mobility in Disordered Organic Semiconductors at Large Carrier Concentrations. *Phys. Rev. B: Condens. Matter Mater. Phys.* **2010**, *81*, 045202.

(30) Balakrishnan, K.; Datar, A.; Naddo, T.; Huang, J.; Oitker, R.; Yen, M.; Zhao, J.; Zang, L. Effect of Side-Chain Substituents on Self-Assembly of Perylene Diimide Molecules: Morphology Control. *J. Am. Chem. Soc.* **2006**, *128*, 7390-7398.

(31) Che, Y.; Yang, X.; Liu, G.; Yu, C.; Ji, H.; Zuo, J.; Zhao, J.; Zang, L. Ultrathin n-Type Organic Nanoribbons With High Photoconductivity and Application in Optoelectronic Vapor Sensing of Explosives. *J. Am. Chem. Soc.* **2010**, *132*, 5743-5750.

(32) Knipp, D.; Street, R. A.; Völkel, A.; Ho, J. Pentacene Thin Film Transistors on Inorganic Dielectrics: Morphology, Structural Properties, and Electronic Transport. *J. Appl. Phys.* **2003**, *93*, 347-355.

(33) Huang, Y.; Fu, L.; Zou, W.; Zhang, F.; Wei, Z. Ammonia Sensory Properties Based on Single-Crystalline Micro/Nanostructures of Perylenediimide Derivatives: Core-Substituted Effect. *J. Phys. Chem. C* **2011**, *115*, 10399-10404.

(34) Jones, B. A.; Facchetti, A.; Wasielewski, M. R.; Marks, T. J. Tuning Orbital Energetics in Arylene Diimide Semiconductors. Materials Design for Ambient Stability

of n-Type Charge Transport. *J. Am. Chem. Soc.* **2007**, *129*, 15259-15278.

(35) Bushey, M. L.; Hwang, A.; Stephens, P. W.; Nuckolls, C. Enforced Stacking in Crowded Arenes. *J. Am. Chem. Soc.* **2001**, *123*, 8157-8158.

(36) Würthner, F. Perylene Bisimide Dyes as Versatile Building Blocks for Functional Supramolecular Architectures. *Chem. Commun.* **2004**, 1564-1579.

(37) Cormier, R. A.; Gregg, B. A. Synthesis and Characterization of Liquid Crystalline Perylene Diimides. *Chem. Mater.* **1998**, *10*, 1309-1319.

(38) Struijk, C. W.; Sieval, A. B.; Dakhorst, J. E. J.; van Dijk, M.; Kimkes, P.; Koehorst, R. B. M.; Donker, H.; Schaafsma, T. J.; Picken, S. J.; van de Craats, A. M.; et al. Liquid Crystalline Perylene Diimides: Architecture and Charge Carrier Mobilities. *J. Am. Chem. Soc.* **2000**, *122*, 11057-11066.

(39) Rühle, V.; Lukyanov, A.; May, F.; Schrader, M.; Vehoff, T.; Kirkpatrick, J.; Baumeier, B.; Andrienko, D. Microscopic Simulations of Charge Transport in Disordered Organic Semiconductors. *J. Chem. Theory Comput.* **2011**, *7*, 3335-3345.

(40) Zang, L.; Liu, R.; Holman, M. W.; Nguyen, K. T.; Adams, D. M. A Single-Molecule Probe Based on Intramolecular Electron Transfer. *J. Am. Chem. Soc.* **2002**, *124*, 10640-10641.

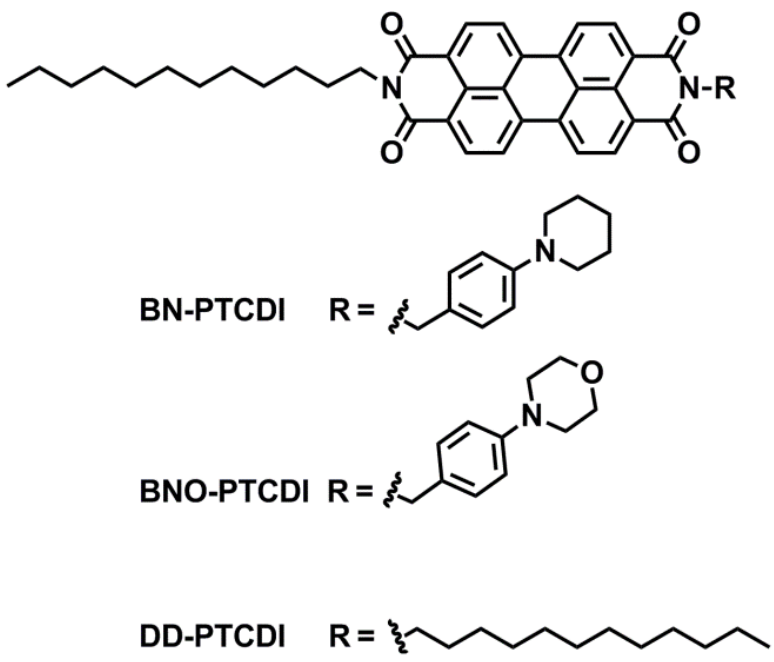

Figure 4.1 Molecular structures of PTCDI derivatives studied in this work.

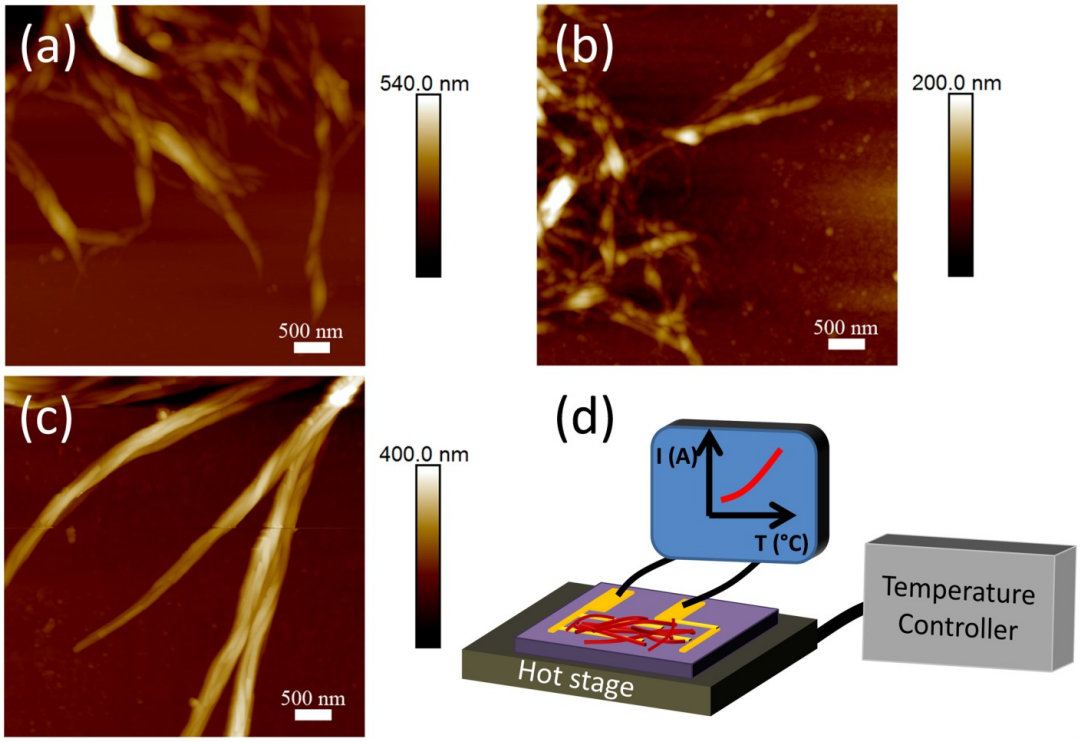

Figure 4.2 Tapping mode AFM topography images of (a) BN-PTCDI, (b) BNO-PTCDI and (c) DD-PTCDI nanofibers; (d) schematic of the IDEs device and temperature control system used for studying the thermo-activated charge transport of PTCDI nanofibers.

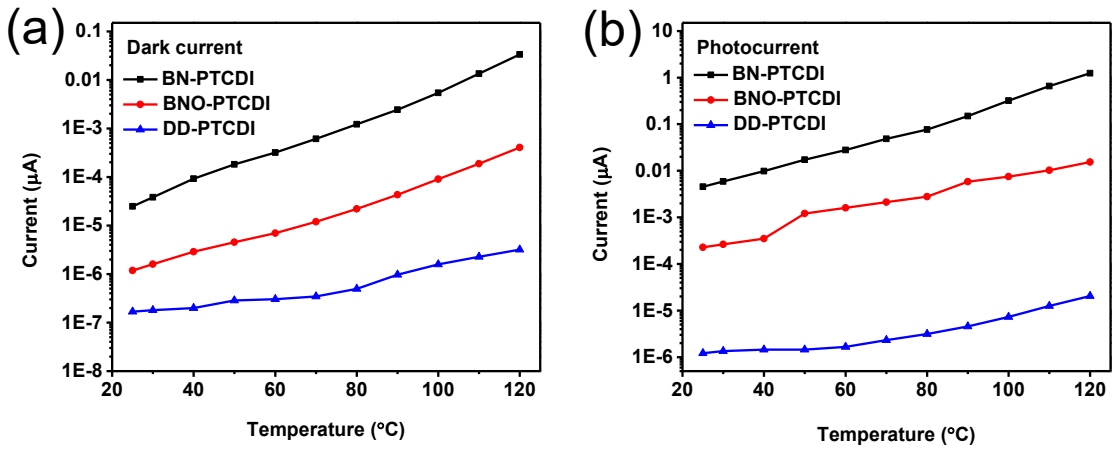

Figure 4.3 The electrical current of PTCDI nanofibers measured at varying temperatures in dark (a) and under white light illumination (7.5 mW cm^{-2}) (b). A constant bias of 10 V was applied during all the measurements. The dark current of BN-PTCDI is two orders of magnitude higher than that of DD-PTCDI, and this is likely due to the self-doping by the piperidine group, which is a strong electron donor and was used before for self-doping of other PTCDIs to increase the electrical conductivity.[25]

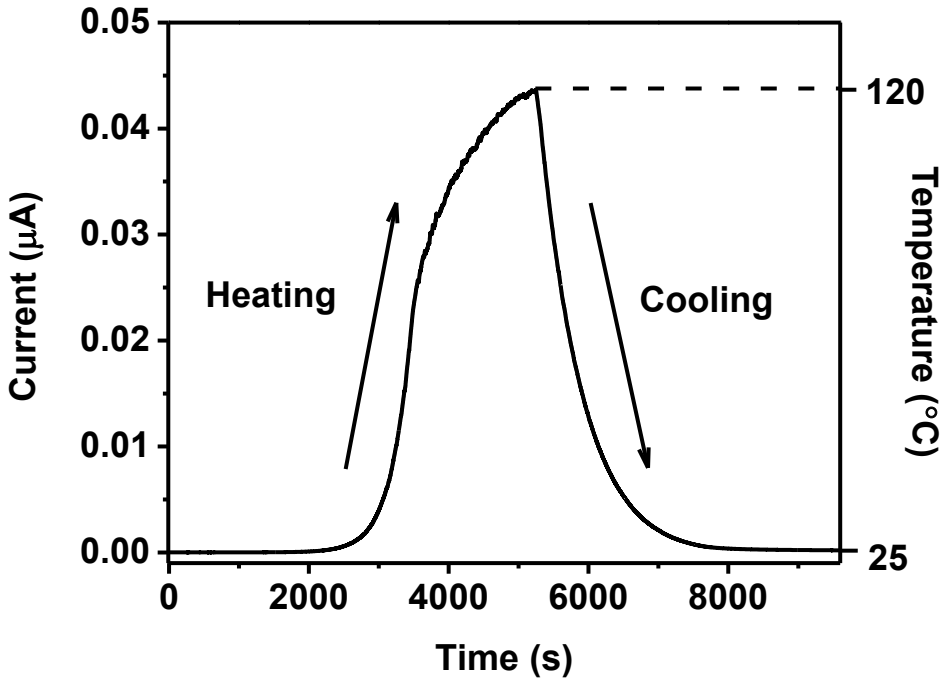

Figure 4.4 Current profile of BN-PTCDI nanofibers in dark with temperature increasing from 25 to 120 °C and then cooling to 25 °C. The bias voltage was 10 V.

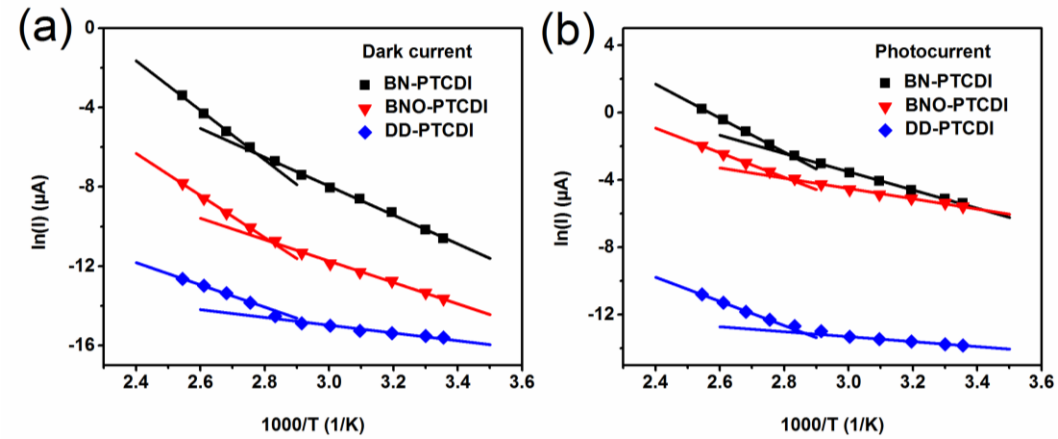

Figure 4.5 Arrhenius plot of current versus inverse temperature for PTCDI nanofibers in dark (a) and under white light illumination (7.5 mW cm^{-2}) (b).

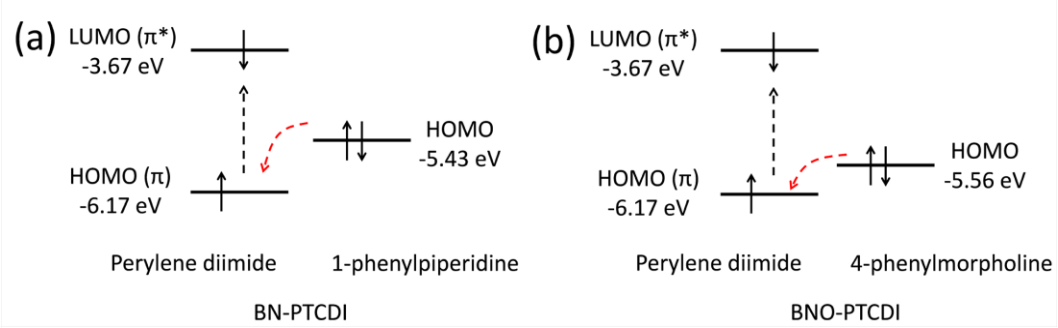

Figure 4.6 Energy level of HOMO (π) and LUMO (π*) orbitals of PTCDI and HOMO orbital of the donor moiety, 1-phenylpiperidine for BN-PTCDI (a) and 4-phenylmorpholine for BNO-PTCDI (b). Geometry optimization and energy calculation were performed with density functional theory (B3LYP/6-311g**// B3LYP/6-31g*) using Gaussian 03 package.

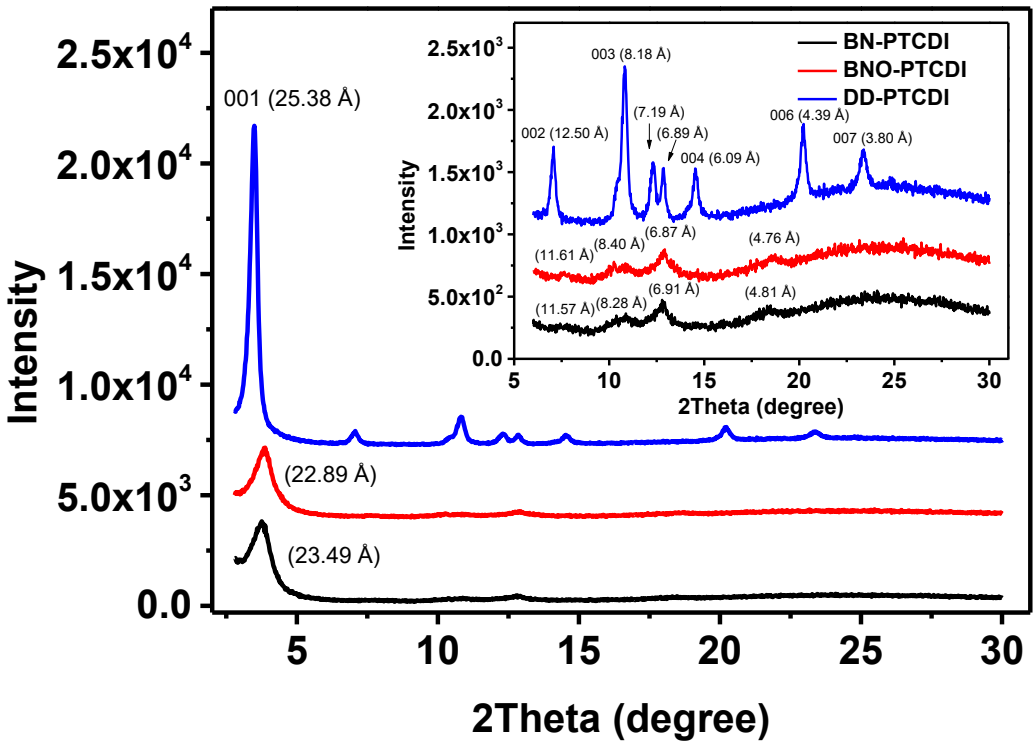

Figure 4.7 X-ray diffraction patterns of BN-PTCDI, BNO-PTCDI and DD-PTCDI nanofibers. The inset is the enlarged spectrum in the degree range from 6° to 30°.

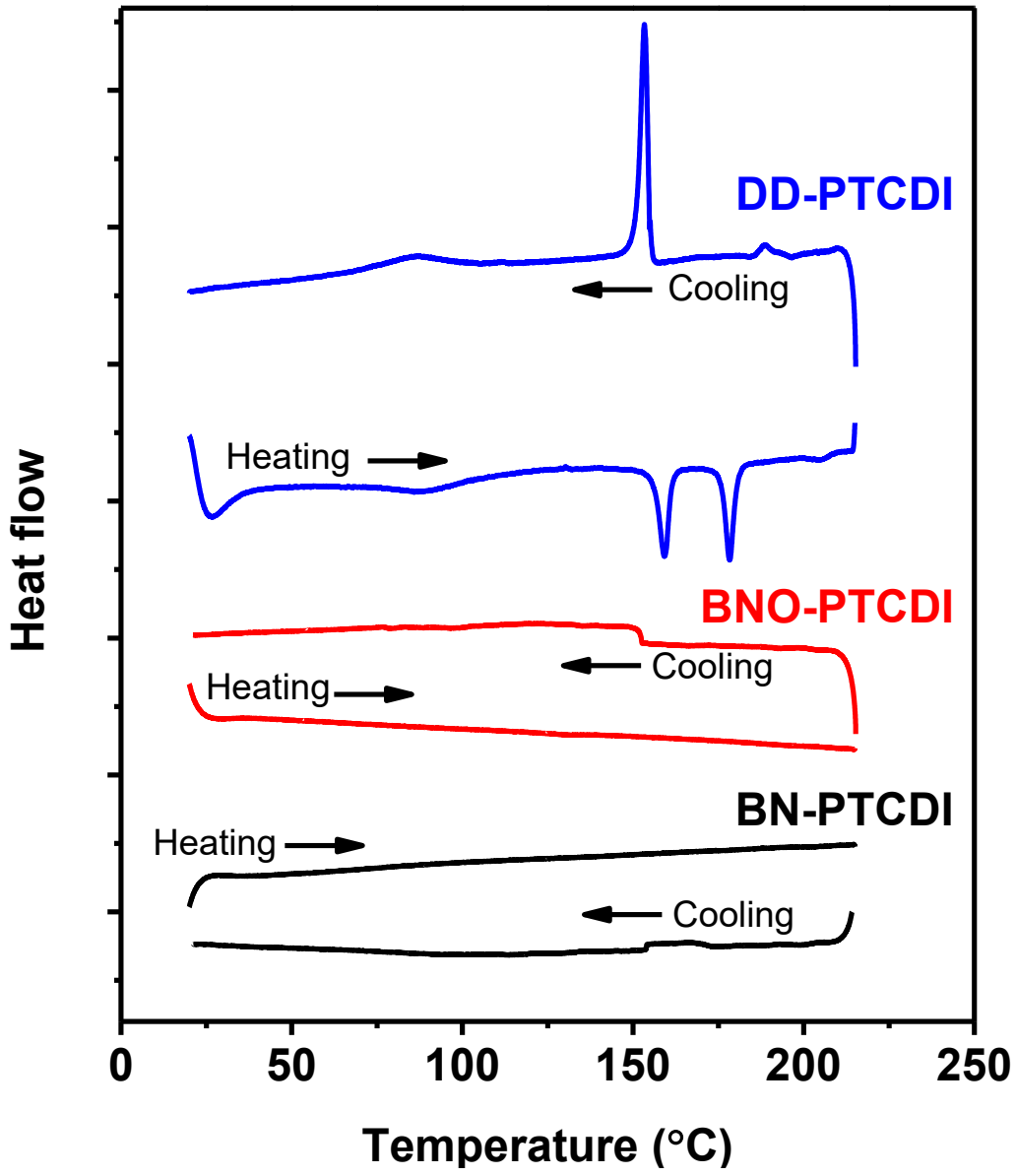

Figure 4.8 Differential scanning calorimetry (DSC) traces of the BN-PTCDI, BNO-PTCDI and DD-PTCDI nanofibers. The data shown are from the second heating-cooling cycle.

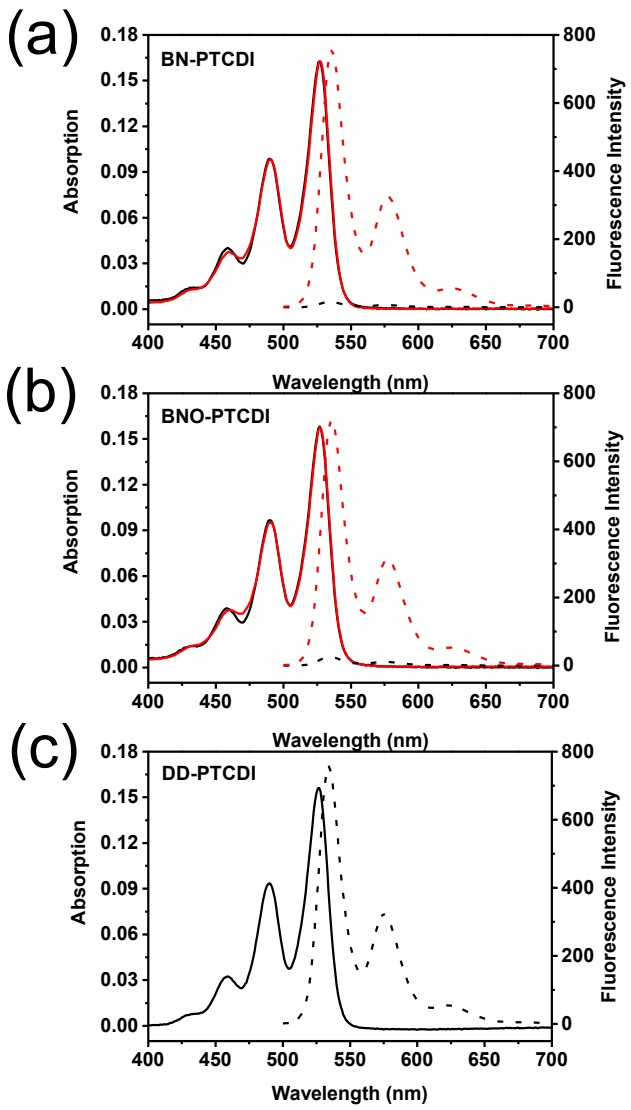

Figure 4.9 UV-vis absorption (black solid) and fluorescence (black dash) spectra of (a) BN-PTCDI, (b) BNO-PTCDI, and (c) DD-PTCDI dissolved in chloroform (2 μmol L^{-1}). Under the same measurement conditions, the fluorescence intensities of BN-PTCDI and BNO-PTCDI solution were much lower than that of DD-PTCDI, but the quenched fluorescence could be recovered by addition of hydrochloric acid (0.1 mol L^{-1}), for which both the UV-vis absorption (red solid) and fluorescence (red dash) spectra were then measured again under the same conditions.

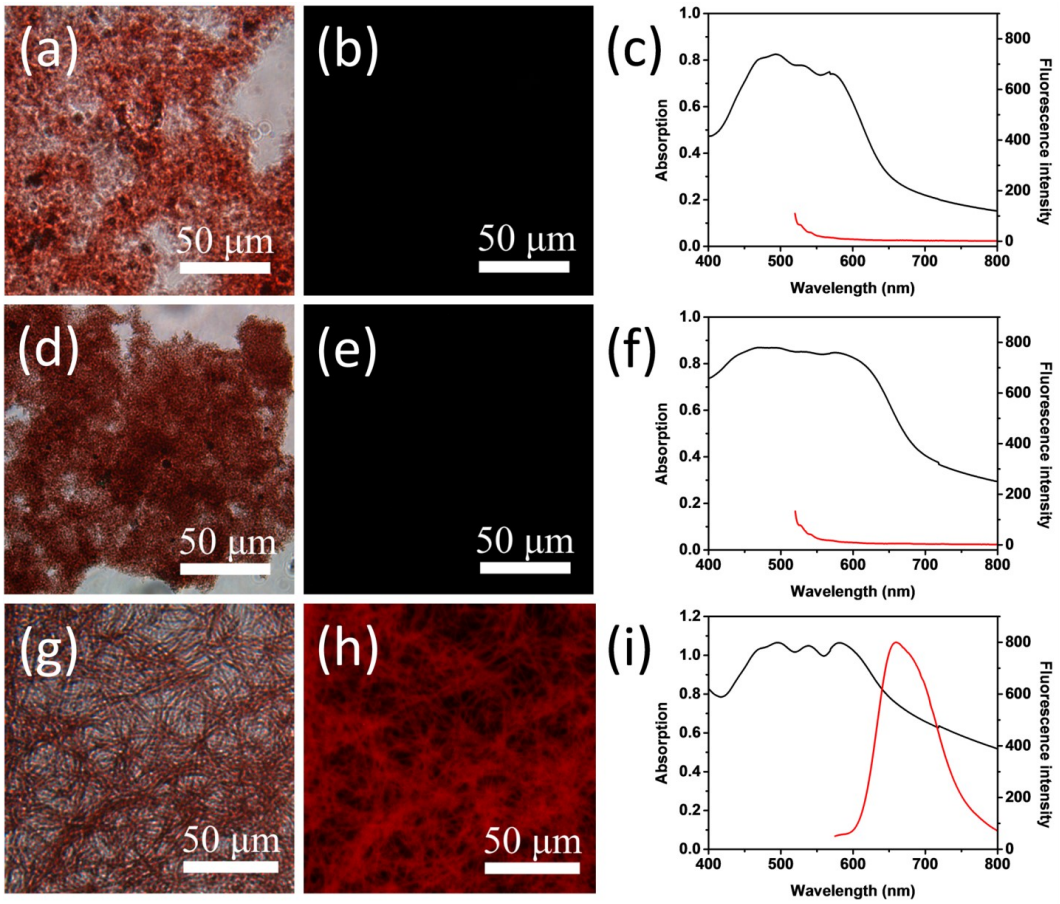

Figure 4.10 Morphologies, UV-vis absorption, fluorescence emission of PTCDI nanofiber thin films: (a, d, g) bright-filed and (b, e, h) fluorescence optical microscopy images of BN-PTCDI, BNO-PTCDI and DD-PTCDI nanofibers, respectively; (c, f, i) UV-vis absorption (black) and fluorescence (red) spectra of BN-PTCDI, BNO-PTCDI and DD-PTCDI nanofibers, respectively. The excitation wavelength for the fluorescence spectrum was 510 nm.

Table 4.1 Activation energy (E_A) estimated for the three PTCDI nanofibers in the low and high temperature range from both the dark current and photocurrent measurements.

Sample	E_A in dark (meV)		E_A under illumination (meV)	
	25 – 80 °C	80 – 120 °C	25 – 80 °C	80 – 120 °C
BN-PTCDI	628	1077	467	868
BNO-PTCDI	465	915	263	628
DD-PTCDI	169	549	127	566

CHAPTER 5

DISSERTATION CONCLUSIONS AND PROPOSED FUTURE WORK

5.1 Dissertation Conclusions

This dissertation is primarily focused on the investigation of electrical properties and potential applications of PTCDI nanofibers with D-A structure. We have designed new PTCDI molecules by substituting one of the imide sides with amine groups (as strong donor) and fabricated them into nanofibers via solution self-assembling. The materials structures, and their optical and electrical properties, were systematically characterized and studied. Moreover, the potential applications of these PTCDI nanofibers have also been explored.

First, we demonstrated a unique chemical self-doping method that could increase the electrical conductivity of a PTCDI-based molecule via a 1D stacking arrangement of D-A PTCDI molecules. The D-A structure is based on 1-methylpiperidine-substituted PTCDI (MP-PTCDI), of which the MP moiety is a strong electron donor, and can form a charge transfer complex with the PTCDI moiety on the other molecule (acting as the acceptor) of an adjacent stacked molecule, generating anionic radical of PTCDI (electron). Upon self-assembling into nanoribbons, the electron generated is delocalized along the long axis of PTCDIs through columnar π–π stacking, leading to enhancement in conductivity. The

resultant PTCDI radicals function as n-type dopants located in the lattice of PTCDI crystals, in contrast to the interstitial doping reported for many other organic semiconductors. With the high conductivity and n-type character, the MP-PTCDI nanoribbons fabricated had highly sensitive responses to H_2O_2 vapor which is a critical signature for improvised peroxide explosives. The lowest detected concentration was down to 0.6 ppm and high selectivity toward H_2O_2 vapor against water and other common organic liquids' vapor. This work provides a simple and efficient approach to fabricating self-doped organic semiconductors with high conductivity by molecular engineering. In addition, the highly conductive PTCDI-based nanofibril materials can potentially be fabricated into a small, light and low-power sensor device for public safety screening and monitoring.

Second, we further studied the persistent photoconductivity (PPC) in PTCDI nanofiber materials by using MP-PTCDI as a case study. It was found that the PTCDI molecules containing strong electron donor groups demonstrated significant PPC when fabricated into nanofiber materials. The donor-acceptor interaction, particularly under photoexcitation, creates charge separation and electrostatic traps, thus producing potential barriers that hinder the recombination of electron-hole pairs. The extended electron delocalization along the π–π stacking (the long axis of nanofiber) further enhances the charge separation, creating more charge relevant defects, resulting in a more pronounced PPC. The temperature dependence of PPC decay time revealed the activation barrier (energy) of 137 meV, which is close to that obtained in the inorganic semiconductors such as n-type GaN. This systematic investigation of the PPC effect in PTCDI nanofibers will provide deep insight into the charge carrier storage and relaxation process within

organic semiconductor materials, thus providing structural design rules for optimizing the photovoltaic and photocatalytic performance of these materials.

Finally, we designed and synthesized more PTCDI molecules with D-A structure (1-phenylpiperidine substituted PTCDI, BN-PTCDI, and 4-phenylmorpholine substituted PTCDI, BNO-PTCDI). Thermoactivated electrical conductivity has been studied on these two D-A PTCDIs and a control sample DD-PTCDI, which is a symmetric molecule with both sides substituted with n-dodecyl chains. The results supported the thermoactivated hopping mechanism for the charge transport, for which the activation energy was found to be primarily dependent on the D-A structure. The D-A nanofibers showed significantly higher activation energy than the DD-PTCDI nanofibers for both the dark current and photocurrent measurements. D-A structure helps create disorder regarding both the charge-transfer and diploe-dipole interactions between stacked molecules, and the increased disorder enlarges the activation barrier. At higher temperatures, polaronic self-trapping may become more dominant in controlling the charge hopping process. In addition, the photocurrent measurement offers an alternative way to the gate control in FET devices to modulate the charge density in material, which allows for investigating the effect of charge density on the thermoactivation of charge hopping.

5.2 Suggestions for Future Work

This dissertation work has provided us deeper insight into the structure and electrical properties of PTCDI nanofibers with D-A structure, as well as the structure-property relationship of these materials. The following suggestions are recommended for continuing research on the 1D nanostructures of D-A PTCDIs.

5.2.1 More Detailed Mechanism Study of PTCDI Molecules With D-A Structure

The current study on PTCDI molecules with D-A structure has demonstrated some interesting structure-property relationships. In the chemical self-doping PTCDI nanofibers project, we have proven the formation of PTCDI anionic radicals, which acted as the n-type dopants. However, a more detailed mechanism will be needed to assist designing more suitable PTCDI molecules with high conductivity. One important factor is the link distance between donor groups and the perylene diimide core because it affects both the intramolecular and intermolecular D/A interactions, as well as the cofacial D/A packing.[1] For future work, we can systematically study the influence of linker distance by changing the alkyl groups between the PTCDI core and donor groups. At the same time, molecular self-assembly patterns can also be modified to study the influence of molecule stacking patterns to the self-doping. The aim of the future study is to achieve structure-controllable self-doping in PTCDI-based materials.

More nanofiber structure characterization, such as single crystal X-ray crystallography or Grzaing incidence X-ray diffractometry (GIXD),[2] will be valuable for providing more detailed information on the nanofibers' structure. Moreover, the transient absorption spectroscopy can also be used to confirm and characterize the charge-separated state directly.[3]

5.2.2 Applications of PTCDI Molecules With D-A Structure

The PPC effect has been observed in PTCDI nanofibers with D-A structures. These types of materials can be used in photovoltaics and photocatalysis systems. In future

work, n-type D-A PTCDI nanofibers with PPC effect, such as MP-PTCDI, can be integrated with p-type OSCs, such as P3HT to fabricated BHJ solar cells, to study their performance,[4] which is expected to provide significantly increased photoconversion efficiency if the device is fabricated with well established processes and techniques. In addition, such PTCDI-based materials can also be applied into photocatalysis systems for photocatalytic splitting of water for H_2,[5,6] or for photocatalytic removal of pollutants.[7]

The PTCDI molecules with D-A structure demonstrated improved sensitivity toward temperature. We can adapt such materials into wearable sensor systems for human-activity monitoring and personal healthcare,[8] where temperature fluctuation plays critical roles. Additionally, the temperature sensor devices with D-A PTCDI molecules can be fabricated into FETs to further enhance the sensitivity because increasing gate voltage can increase the charge density.

5.3 References

(1) Wang, T.; Weerasinghe, K. C.; Sun, H.; Hu, X.; Lu, T.; Liu, D.; Hu, W.; Li, W.; Zhou, X.; Wang, L. Effect of Triplet State on the Lifetime of Charge Separation in Ambipolar D-A1-A2 Organic Semiconductors. *J. Phys. Chem. C* **2016**, *120*, 11338-11349.

(2) Krauss, T. N.; Barrena, E.; Zhang, X. N.; de Oteyza, D. G.; Major, J.; Dehm, V.; Würthner, F.; Cavalcanti, L. P.; Dosch, H. Three-Dimensional Molecular Packing of Thin Organic Films of PTCDI-C8 Determined by Surface X-Ray Diffraction. *Langmuir* **2008**, *24*, 12742-12744.

(3) Walsh, J. J.; Lee, J. R.; Draper, E. R.; King, S. M.; Jäckel, F.; Zwijnenburg, M. A.; Adams, D. J.; Cowan, A. J. Controlling Visible Light Driven Photoconductivity in Self-Assembled Perylene Bisimide Structures. *J. Phys. Chem. C* **2016**, *120*, 18479-18486.

(4) Li, L.; Jacobs, D. L.; Bunes, B. R.; Huang, H.; Yang, X.; Zang, L. Anomalous High Photovoltages Observed in Shish Kebab-Like Organic p-n Junction Nanostructures. *Polym. Chem.* **2014**, *5*, 309-313.

(5) Chen, S.; Jacobs, D. L.; Xu, J.; Li, Y.; Wang, C.; Zang, L. 1D Nanofiber Composites

of Perylene Diimides for Visible-Light-Driven Hydrogen Evolution From Water. *RSC Adv.* **2014**, *4*, 48486-48491.

(6) Chen, S.; Li, Y.; Wang, C. Visible-Light-Driven Photocatalytic H_2 Evolution From Aqueous Suspensions of Perylene Diimide Dye-Sensitized Pt/TiO_2 Catalysts. *RSC Adv.* **2015**, *5*, 15880-15885.

(7) Dong, G.; Yang, L.; Wang, F.; Zang, L.; Wang, C. Removal of Nitric Oxide through Visible Light Photocatalysis by *g*-C_3N_4 Modified With Perylene Imides. *ACS Catal.* **2016**, *6*, 6511-6519.

(8) Someya, T.; Kato, Y.; Sekitani, T.; Iba, S.; Noguchi, Y.; Murase, Y.; Kawaguchi, H.; Sakurai, T. Conformable, Flexible, Large-Area Networks of Pressure and Thermal Sensors With Organic Transistor Active Matrixes. *Proc. Natl. Acad. Sci. U. S. A.* **2005**, *102*, 12321-12325.